INFORMATION TO USERS

This manuscript has been reproduced from the microfilm master. UMI films the text directly from the original or copy submitted. Thus, some thesis and dissertation copies are in typewriter face, while others may be from any type of computer printer.

The quality of this reproduction is dependent upon the quality of the copy submitted. Broken or indistinct print, colored or poor quality illustrations and photographs, print bleedthrough, substandard margins, and improper alignment can adversely affect reproduction.

In the unlikely event that the author did not send UMI a complete manuscript and there are missing pages, these will be noted. Also, if unauthorized copyright material had to be removed, a note will indicate the deletion.

Oversize materials (e.g., maps, drawings, charts) are reproduced by sectioning the original, beginning at the upper left-hand corner and continuing from left to right in equal sections with small overlaps.

Photographs included in the original manuscript have been reproduced xerographically in this copy. Higher quality 6" x 9" black and white photographic prints are available for any photographs or illustrations appearing in this copy for an additional charge. Contact UMI directly to order.

Bell & Howell Information and Learning
300 North Zeeb Road, Ann Arbor, MI 48106-1346 USA

UMI®
800-521-0600

Fusion Enhancement With Neutron-Rich Radioactive Beams

by

Kristiana Elizabeth Zyromski

A Dissertation

submitted to

Oregon State University

in partial fulfillment of
the requirements for the
degree of

Doctor of Philosophy

Completed September 7, 1999
Commencement June 2000

Doctor of Philosophy dissertation of Kristiana Elizabeth Zyromski presented on September 7, 1999

APPROVED:

Walter Loveland

Major Professor, representing Chemistry

John Nichols Hall

Chair of the Department of Chemistry

Sally Francis

Dean of the Graduate School

I understand that my dissertation will become part of the permanent collection of Oregon State University libraries. My signature below authorizes release of my dissertation to any reader upon request.

Kristiana E Zyromski

Kristiana Elizabeth Zyromski, Author

ACKNOWLEDGMENT

There have been many people during the course of this work who have provided me with their time, money, expertise, patience, and intellectual and moral support. It would be impossible to list you all here, but you know who you are; I couldn't have done it without you.

This work was funded in part by the U.S. Department of Energy, the OSU Chemistry Department, the Association for Women In Science Educational Foundation, the David P. Shoemaker Memorial Fellowship, and the Oregon Sports Lottery.

First and foremost, thanks goes to my advisor, Walter Loveland. You've given me an education that rivals anything at the "big" labs, and you've been unfailingly patient and supportive every step of the way. Coming to work for you stands as one of the best decisions of my life.

A huge thank-you also goes to:

My collaborators on these experiments: Kjell Aleklett, Dave Morrissey, Oleg Batenkov, George Souliotis, Ricardo Yanez, Ida Forsberg, Chris Powell, Maria Sanchez-Vega, John Dunn. Your time and effort has made this possible. Special thanks also to Kjell for a wonderful summer in Uppsala, Sweden.

Bruce Glagola and Raman Anantaraman, for excellent user support at ATLAS and NSCL. Also Mathias Steiner, Jeff Stetson, and Reg Ronnigen, for the radioactive beams; and the accelerator operators of ATLAS and NSCL.

Ron Fox, for long-distance computer support above and beyond the call of duty; Lucas Hart, who will someday write a book entitled "Scientific Computing on the DEC Alpha, For Dummies", and dedicate it to me; Mike Conrady and Bob Boyer, for network and hardware support.

The faculty and staff of the Radiation Center, the Chemistry Department, and the Physics Department here at OSU. I have been a part of all three communities, and I consider myself triply lucky. A special thanks to Phil Siemens, who has been a constant source of intellectual, practical and moral support.

My family, for putting up with my absence and my ups and downs; Father T, without whom none of this would have happened; Joey, who can always make it better; Dr. F.D. Flower, Becca, the boys of 2925, the RSC, Craig-n-Scott, MDMS, my Swedish rent-a-friends, CJ, Rob, the McFlies, Wendy, my MSU cohorts, and all those who have loved me enough to forgive my disappearance from reality for a couple years.

And Travis, for giving me a reason just when I needed one.

DEDICATION

For Father Ted Thepe, S.J.

Teacher, mentor, friend.

TABLE OF CONTENTS

TABLE OF CONTENTS (Continued)

LIST OF FIGURES

LIST OF FIGURES (Continued)

LIST OF FIGURES (Continued)

LIST OF TABLES

FUSION ENHANCEMENT WITH NEUTRON-RICH RADIOACTIVE BEAMS

1. INTRODUCTION

1.1. Radioactive nuclear beams

For more than a decade, accelerator facilities providing beams of radioactive ions have been improving their production techniques, making possible an ever-increasing range of experiments using short-lived radioactive nuclei. Of the roughly 6000 nuclides with predicted halflives greater than 1 μs, about 2000 have been observed; only about 300 of these are stable or long-lived [Boy92]. Clearly, the availability of radioactive beams opens vast possibilities for nuclear structure and reaction studies.

Radioactive beam facilities use two main production methods: projectile fragmentation (PF) and isotope separation on-line (ISOL). In the ISOL method, fission, spallation, and/or fragmentation are used to produce exotic nuclei. The product nuclei then diffuse out of the target into an ion source where they are separated, and the desired beam is accelerated. Projectile fragmentation depends on reactions in inverse kinematics: a light target is bombarded by a high-energy projectile with mass greater than the target; the resulting fragmentation products are strongly forward-focused and have velocities near that of the primary beam. No secondary acceleration is necessary in the projectile-fragmentation method. The two techniques are complementary in many respects: ISOL facilities generally have higher beam intensities, but PF facilities have a greater range of possible elements

and halflives. Detailed descriptions of the methods of radioactive nuclear beam (RNB) production can be found in reviews by Mueller and Sherrill [Mue93] and by Giessel, Münzenberg, and Riisager [Gie95].

1.2. Fusion with neutron-rich projectiles

In fusion reactions, the magnitude of the cross section is basically determined by the height of the fusion barrier. Macroscopically, increasing neutron enrichment for a given projectile or target element leads to a net lowering of the Coulomb barrier. Since the barrier is proportional to $Z_1 Z_2/(A_1^{1/3} + A_2^{1/3})$, an increase in mass with no increase in charge results in a net lowering of the barrier, and corresponding enhancement of the low-energy cross sections.

Superimposed on this global behavior, however, are a rich variety of nuclear structure effects. For example, it has been shown [Sto78, Sto80, Rei82, Rei85] that deformation leads to significant enhancement of the cross sections, especially at subbarrier energies. Coupling to vibrational modes [Bec88, Ste90] can also enhance subbarrier cross sections. Transfer of nucleons and rapid isospin equilibration of the fusing system has been shown [Bec80, Bec81, Bec82, Ste86] to play a role, sometimes to the extent that the neutron-deficient projectile yields the larger cross sections. (An example of this is seen in the ^{32,36}S + ^{110}Pd reaction [Ste95], where the ^{32}S-induced cross sections are an order of magnitude larger at low energies than those of the ^{36}S-induced reaction, due to a strong two-neutron transfer channel.) The influence of neutron transfer has also been described macroscopically in terms of neutron flow and neck formation [Ste90]. The influence of nuclear structure on fusion cross sections has been a topic of much interest in the literature, and several detailed reviews have been written on the subject. (See, e.g., [Rei94, Das98].)

The use of radioactive neutron-rich projectiles in fusion reactions is interesting both from a macroscopic point of view and in light of the unusual structure of these nuclides. The neutron enrichment should lead to a significant lowering of the Coulomb barrier as compared to stable isotopes; in heavy-element synthesis reactions especially, where it is advantageous to form the product compound nuclei with the lowest possible excitation energy, this barrier shift is of interest. The structure of extremely n-rich neutron-skin and neutron-halo nuclei has led to much theoretical discussion about fusion with radioactive projectiles. The binding energy of the last neutrons in these nuclei is small, and their matter radii are correspondingly large and diffuse. Predictions have been made that a "soft dipole" vibration (vibration of the nuclear core against the neutron skin) or neck formation can cause significant enhancement of the cross section for these projectiles [Agu88, Agu92, Das92, Tak92]. However, the possibility of breakup of the halo (or loss of the valence neutrons before fusion) has also been postulated, and there is significant disagreement among theorists as to the net effect of fusion with exotic neutron-rich nuclei [Tak91, Hus91a, Hus91b, Das92, Agu92, Tak92].

Preliminary experimental measurements of fusion with radioactive n-rich beams have yielded results that are sometimes conflicting or inconclusive. In measurements of fusion of the neutron-skin nucleus ^{6}He with ^{209}Bi, anomalously large fission cross sections were observed [Pen95], while evaporation residue cross sections showed no significant enhancement. However, the results of Kolata *et al.* [Kol98, Dey98] for the same system are in direct disagreement, finding the fission cross sections to be more than an order of magnitude smaller than those seen in the previous work. Fusion measurements for the ^{6}He + ^{209}Bi [Kol98] and ^{11}Be + ^{209}Bi [Yos95] systems show no evidence for suppression of fusion due to projectile breakup, but a strong enhancement of the low-energy cross sections which has been attributed to

neutron flow. Fission measurements for the ^{9,11}Be + ^{238}U systems [Fek95, Fek97], however, show an anomalous decrease in the cross section at near-barrier energies for the ^{11}Be-induced reaction, which could be attributed to projectile breakup. (The authors have also speculated that the unusual behavior of the excitation function could be due to feeding of the low-energy cross sections by transfer reactions.) A preliminary analysis of the ^{32,38}S + ^{181}Ta fusion-fission reactions [Zyr97] showed only an enhancement which was explainable in terms of Coulomb and size effects. The first experimental measurements of fusion with exotic neutron-rich nuclei have left many open questions.

1.3. Possibilities for heavy-element synthesis

In theory, radioactive neutron-rich beams could be a useful tool in the synthesis of the heaviest elements. Two methods are used in heavy-element synthesis reactions. "Hot" fusion is fusion of a light projectile with an actinide target, followed by evaporation of several neutrons. At each step in the evaporation cascade, however, neutron evaporation competes with fission as a decay mode. Moving up the periodic table, the "window" between the energy to overcome the Coulomb barrier and the maximum excitation energy for a reasonable probability of survival of the heavy nucleus becomes smaller and smaller. Elements 107 to 109 were synthesized in the 1980s using heavy projectiles to bombard targets of lead and bismuth. [Mün81, Mün82, Mün84, Mün86, Mün88, Oga84] It had been shown [Oga74] that the use of targets near the closed-shell nucleus ^{208}Pb led to a minimization of the compound nucleus excitation energy; this method is referred to as "cold fusion". The use of a heavy projectile, however, results in smaller fusion cross sections than for hot fusion, due to a dynamical hindrance to fusion when $Z_p Z_t > 1600$ [Bjø82, Swi82]. The

lowering of the Coulomb barrier due to the use of neutron-rich radioactive projectiles would allow synthesis of compound nuclei at lower excitation energies, and the predicted enhancements to the low-energy cross sections due to exotic effects could also have a significant effect on heavy-element synthesis reactions.

The major drawback to the use of radioactive neutron-rich nuclei in heavy-element synthesis is the limitation of low beam intensities with RNBs. It has been shown [Lov93] that for synthesis of elements 110 and above, high-intensity stable beams are still the only method of achieving reasonable overall production rates. However, synthesis of several neutron-rich isotopes of the lighter transactinides could be feasible using radioactive-beam reactions. Since the N/Z ratio along the line of β-stability increases with increasing atomic number, the use of a stable projectile and target in a fusion reaction will result in a compound nucleus that is neutron-deficient. A neutron-rich projectile would bring the product compound nucleus closer to the line of stability, with a correspondingly longer halflife. The use of radioactive beams in heavy-element synthesis reactions could allow synthesis of transactinides with halflives long enough for detailed study of their physical and chemical properties.

This thesis describes the first U.S. measurements of fusion with neutron-rich radioactive beams, using the system $^{32,38}S + {}^{181}Ta \rightarrow Ac$. Chapter 2 provides a description of the experimental design and methods. Chapters 3 and 4 detail the data analysis of the ^{32}S- and ^{38}S-induced reactions, and compare the results to various models of heavy-ion fusion; and Chapter 5 contains a comparison of the two systems, conclusions, and suggestions for future research.

2. EXPERIMENTAL DESIGN AND PROCEDURES

Reaction studies with radioactive beams pose a unique set of challenges as compared to measurement of fusion reactions using stable beams. The problems of low beam intensities, energy spread, and beam impurities must be addressed in order to obtain a reliable measurement. The goal of the experimental design was to choose a system which could act as a prototype for measuring the effects of unstable neutron-rich projectiles on heavy-ion fusion, while remaining within the current practical limitations on radioactive beam studies. The experiment itself had to provide a clear characterization of the radioactive beam and efficient detection of the reaction products, so that the fusion cross section could be measured in a low-event-rate situation, and the reaction products unambiguously attributed to the projectile of interest.

2.1. Choice of reaction

The reactions chosen for study were $^{32,38}S + {}^{181}Ta \rightarrow Ac$. Stable ^{32}S has a neutron-to-proton ratio of 1:1, while radioactive ^{38}S has a ratio of 1.38:1, which is as neutron-rich as anything currently available in reasonable intensities from radioactive-beam facilities. Neither the projectiles nor the target are magic, and so any enhancement of the fusion cross section would not be due to the shell-stabilization effects discussed in Section 1.3. The system is heavy enough to be a reasonable prototype for heavy-element fusion reactions, but the sulfur projectile is light enough that it was hoped that quasifission would be minimized. (The charge product Z_pZ_t is 1168 for this system; the effects of a dynamical hindrance to fusion are typically associated with $Z_pZ_t \geq 1600$ [Bjø82, Swi82].) According to calculations with the statistical code PACE [Gav80], the actinium compound nuclei

decay by fission in greater than 99% of the events. For heavy systems, fission is the dominant decay mode for a compound nucleus, with only the lowest angular momentum partial waves resulting in evaporation residues. If a significant fraction of the reaction strength went to residue formation, it would be necessary to account for this component before fitting the total fusion cross section. In this case, the fusion-fission cross section could be taken to be equivalent to the fusion cross section without correction for a heavy residue component, according to PACE calculations. Predictions using the code HIVAP [Rei81], however, showed a significant fraction of the low-energy cross section in the residue channel. In order to test the question experimentally, detectors to look for the alpha decay of any residues that might be produced were included in the experimental design. One of the most important factors influencing the choice of projectile, however, was that the radioactive ^{38}S beam was immediately available in intensities sufficient to make a fusion study possible. The fusion enhancement factors for the more exotic, and less available, ^{54}Ca have been predicted [Agu92, Das92]; it was hoped that a first generation of prototypical measurements could aid in the development of realistic theories of fusion enhancement using radioactive neutron-rich projectiles.

2.2. The stable-beam ^{32}S experiment

In order to make a meaningful assessment of the effects of using neutron-rich ^{38}S in a fusion reaction, it was necessary to measure the fusion excitation function for its stable analog ^{32}S for comparison. The following section describes the experimental details of the stable-beam measurement, and can be used as a standard to compare the differences in experimental design required to do reaction studies with radioactive beams.

2.2.1. Beam characteristics

The ^{32}S + ^{181}Ta experiment was performed at the ATLAS accelerator at Argonne National Laboratory. Well-focused, well-collimated beams of ^{32}S with intensities of 4 to 8 enA (or 1.5 to 3×10^9 ^{32}S/second) were sent to the 36" scattering chamber where the experimental apparatus was arranged. Measurements were made at sixteen beam energies ranging from 157 to 300 MeV; the measurements were made in two separate passes through the range of energies in order to avoid possible systematic error. All energy changes were made in the accelerator, with no additional energy degradation at the chamber. Typical energy resolution of the beam was ± 0.01 to ± 0.1 MeV, and so direct measurement of time-of-flight of the beam particles was unnecessary. (Beam energy and resolution at ATLAS are determined continuously in the linac by multiple time-of-flight measurements of the arrival of beam bunches at various points along the beamline.) A satellite beam, nominally identified by time-of-flight and energy to be ^{16}O, was observed as scattered beam in the most forward detectors, but it was a very small component (on the order of 10^{-9} of the total beam) and was easily separable in the data analysis.

2.2.2. Chamber setup

In the scattering chamber, sixteen 300 mm^2 silicon surface-barrier detectors of thickness 60 to 100 μm were arranged in a plane at angles from 15° to 160° in the lab frame, at a distance of 170 mm from the target. A schematic diagram of the setup is shown in Figure 2.1. Each detector subtended 10.4 msr, and so the total solid angle covered by the detector array was 1.3% of 4π. The target ladder in the center of the chamber contained an 0.46 mg/cm^2 self-supporting ^{181}Ta target and a 3 mm diameter hole for tuning. (Targets for all of the experiments were made

by L. Einarsson of Uppsala University in Sweden. Thicknesses were measured by weight, and variations in target thickness were estimated to be 10% by scanning across the midline of the target with an ^{241}Am source.) The target ladder could be rotated, and so for most energies, measurements were made with the target both perpendicular and at an angle to the beam (to increase available target thickness). A Faraday cup at the end of the beamline was connected to a current integrator in the operators' area; the output of this integrator was scaled at the experimental area to record beam current.

The current integrator values became suspect during the data analysis, due to two incidents early in the experiment. The first was the operators' ability to change the integrator's full-scale value without notifying the experimenters. The second incident was a recurrent discharging effect observed in the beam current meter. It was discovered that the tantalum plate which should rest at the back of the Faraday cup was lodged at an angle so close to the mouth of the cup that it was arcing across the insulator to the chamber. Instead of current deposited by the beam being continuously read through the integrator, then, the cup was periodically charging and discharging to the chamber, giving inaccurate readings on the integrator. Although these problems were corrected early in the experiment, during the data analysis the beam currents were normalized using measured elastic scattering cross sections. The normalization procedure will be described in detail in Section 3.1.2.

2.2.3. Data acquisition

Figure 2.2 shows a schematic diagram of the electronics for the stable-beam experiment. A fast signal for timing and a slow energy signal were taken from

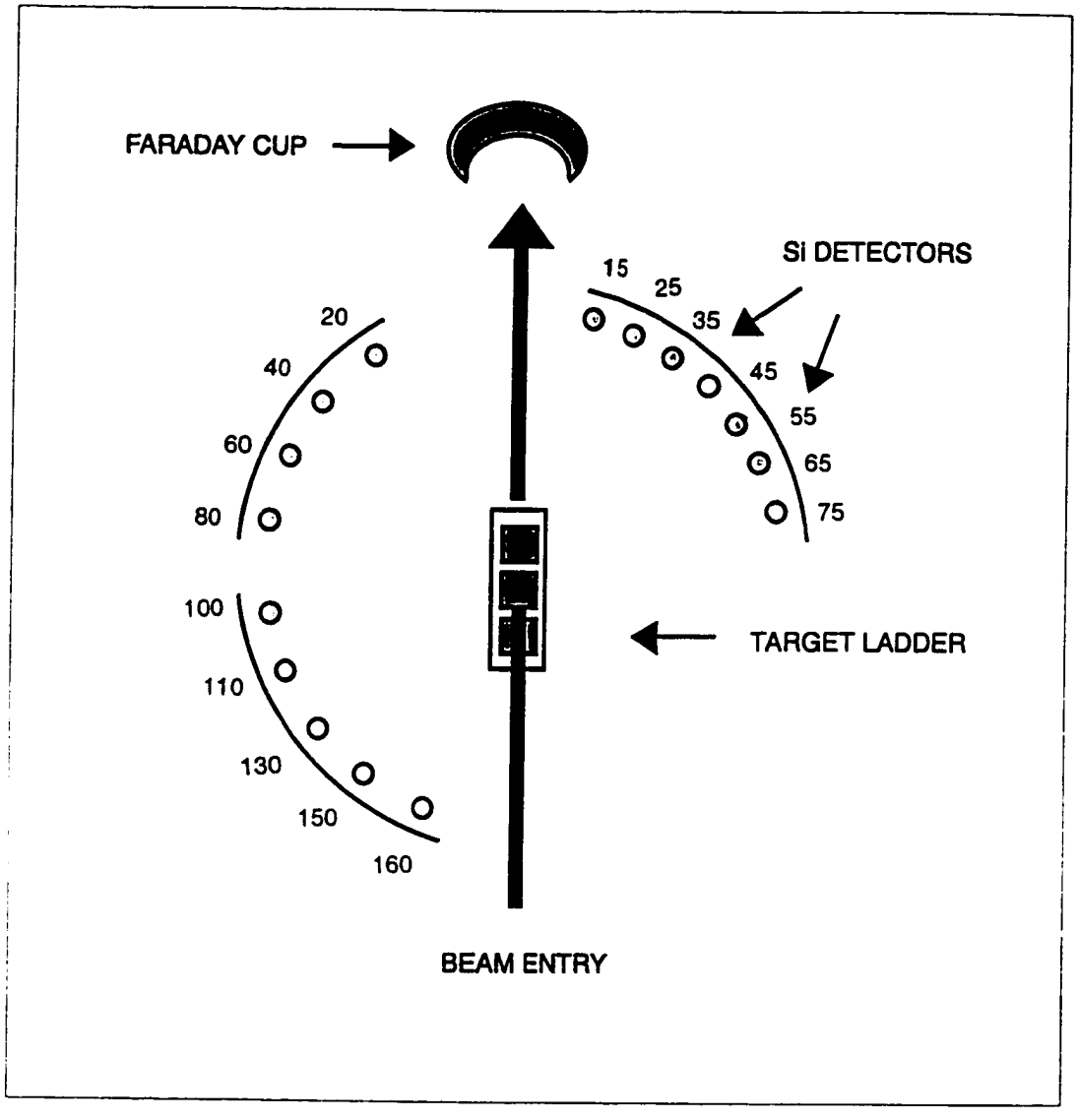

FIGURE 2.1. Schematic diagram of the experimental setup for the ATLAS experiment.

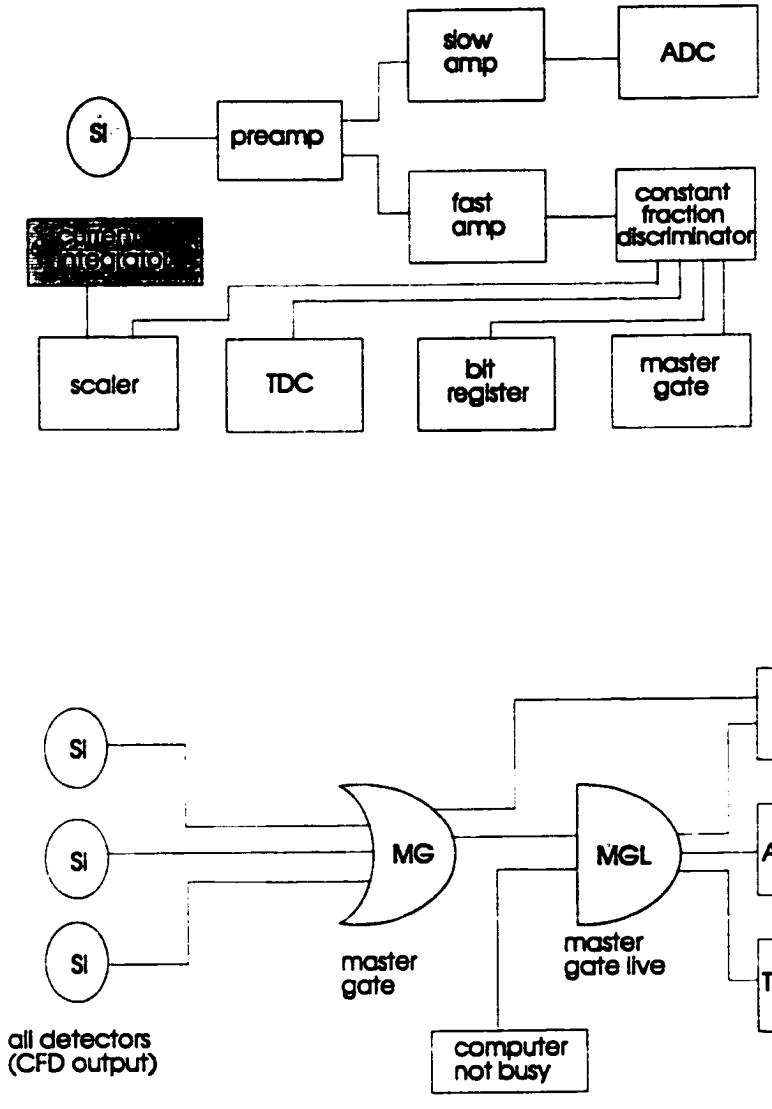

FIGURE 2.2. Schematic diagram of the electronics for the ATLAS experiment.

the preamps for each of the sixteen silicon detectors; the slow signals were sent to analog-to-digital converters (ADCs) to measure the energy of the incident particles. Each fast signal was sent to a constant fraction discriminator to cut out low-level noise and derive the time signal for the event, and the output fast logic pulse was fanned to a scaler, a time-to-digital converter (TDC), a coincidence register, and the "master gate" logic. (The TDCs were later discovered to have been misaligned, and so time-of-flight information for particles incident on the Si detectors was not available for this experiment.) The coincidence register (or "bit register") assigns one bit for each input, and so for a valid event registers which detector(s) triggered the event and records coincident triggers in multiple detectors.

A valid event was defined by the master gate (MG): negative logic pulses from each of the silicon detectors were combined in a logical .OR., and provided a single signal that any detector had fired. This was used in a logical .AND. with a "not busy" signal from the computer to create the "master gate live" (MGL). The master gate live served as a strobe to the ADCs, TDCs, and bit register to read the input signals for the event. In addition, the master gate live : master gate ratio defined the live time of the data acquisition system. Typical live time values ranged from 70-90%. Signals from the MG, MGL, and beam current integrator (as well as the individual detectors) were monitored using scalers, which read continuously and were not restricted by the event logic. Data were read from the modules via a CAMAC crate and controller, which were connected to a computer running the Michigan State data acquisition software and SARA data analysis system [Fox89, She94].

The beam current for a typical run was $1.5 - 3 \times 10^9$ ^{32}S/second, giving event rates from 250-300 fission fragments/minute in the most forward detectors to

50-100/minute in the most backward detectors. Measurements of one half hour to one hour per energy were made in order to obtain adequate statistics.

2.3. The radioactive beam ^{38}S experiments

The fusion excitation function for the radioactive beam ^{38}S + ^{181}Ta reaction was measured in two separate experiments at the National Superconducting Cyclotron Laboratory (NSCL) at Michigan State University. Beams from the K1200 cyclotron were fragmented, and the secondary radioactive beam was separated and energy-degraded in the A1200 fragment separator. After separation, the beam was sent to the 92" scattering chamber where the experimental setup was located. In the chamber, the beam energy was further degraded, beam characteristics were observed, and measurement of the fusion reaction took place.

2.3.1. RNB production in the A1200 spectrometer

Radioactive beams are produced at the NSCL by the projectile fragmentation method, in which a high-energy primary beam impinges on a light target, and the resulting fragments continue forward at velocities near that of the primary beam, as described in Section 1.1. The desired secondary beam is then selected from the fragmentation products by a magnetic separator, and sent to the experimental area. Figure 2.3 shows the A1200 magnetic spectrometer at the NSCL. The device consists of fourteen superconducting quadrupole magnets and four superconducting dipoles, with four sextupoles used for higher-order optical corrections [She91]. Beams from the K1200 cyclotron are fragmented using a production target at the beginning of the spectrometer; for these experiments, the primary beam was ^{40}Ar at 40 MeV/A, and the production target was 141 mg/cm^2 ^{9}Be. As they pass

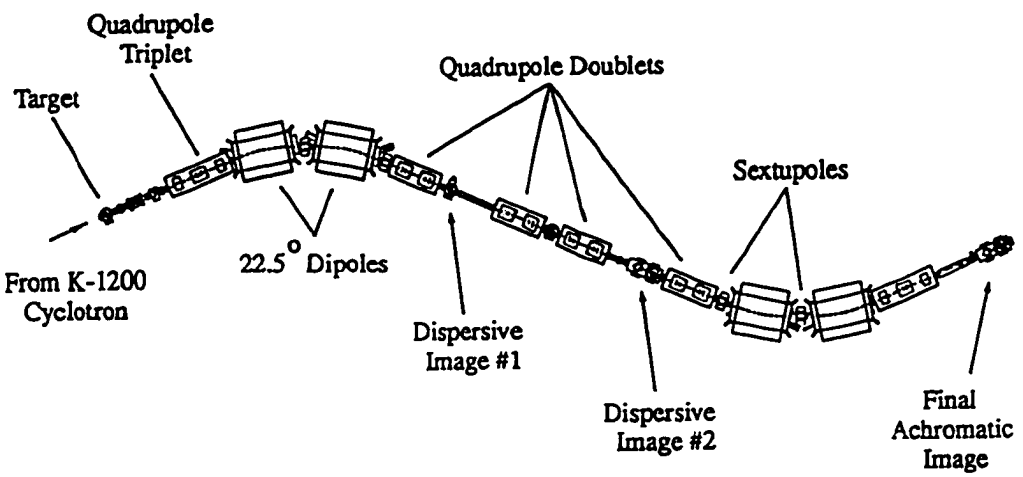

FIGURE 2.3. The A1200 magnetic spectrometer at the NSCL [She91].

through the first set of dipoles, fragments are separated by their magnetic rigidity, based on the relationship

$$B\rho = \frac{mv}{q} \tag{2.1}$$

Magnetic rigidity $B\rho$ is the product of the magnetic dipole field B and the radius of curvature ρ of the particle trajectory; m, v, and q correspond to the mass, velocity, and charge of the particle. At the position labeled "Dispersive Image #1", a set of slits allow momentum selection. The A1200 has a maximum momentum acceptance of $\frac{\Delta p}{p} = 3\%$ at Image 1, although smaller acceptance can be selected by inserting narrower transmission slits. For the majority of the time during the ^{38}S experiments, the A1200 was run with 3% momentum acceptance in order to maximize the beam intensities. (High beam purity was less important than intensity, since the experimental setup was designed for event-by-event beam characterization.) A thin plastic scintillator at Image 1 acts as a start detector for time-of-flight measurements during beam identification runs. At the position labeled "Dispersive Image #2", an achromatic degrader wedge is used to separate fragments of similar mass/charge by differential energy loss. For these experiments, a plastic wedge with thickness 100 mg/cm^2 was used. The second set of dipoles separates the fragments further based on this energy loss through the degrader, and the secondary beam emerges at the focal plane (labeled "Final Achromatic Image" in Figure 2.3). During typical beam diagnostic runs in the A1200, a pair of PPACs (parallel-plate avalanche counters, which are x-y position-sensitive gas-filled transmission detectors) are used at Image 2 to observe fragment momentum, and another pair of PPACs are used at the focal plane to measure final positions and angles of the secondary beams. Velocity measurements are made using the 14 m flight path from Image 1 to the focal plane,

and particle identification is made at the focal plane using a set of silicon and/or plastic ΔE-E detectors.

Figure 2.4 shows the results of a simulation using the code INTENSITY to predict fragmentation products for 40 MeV/A ^{40}Ar incident on a 141 mg/cm^2 ^{9}Be target. INTENSITY [Win92] was written by NSCL scientists as a tool for estimating secondary beam production in the A1200 and other fragment separators; the code typically agrees with experimental observations in the A1200 to about an order of magnitude. Although the absolute cross sections shown in Figure 2.4 should be taken with caution, the simulation results can be used to gain an understanding of the relative intensities of fragments entering the separator. The primary peaks for each element in Figure 2.4 are ^{40}Ar (65 mb), ^{37}Cl (49 mb), ^{34}S (37 mb), and ^{32}P (36 mb). In contrast, the ^{38}S peak is only 2 mb. After passage through the A1200, however, the ^{38}S component can be selected and separated from the other, higher-intensity fragmentation products. Figure 2.5 shows results of an INTENSITY simulation for the same reaction after passage of the A1200. The input parameters for this calculation ($B\rho_1$ = 1.7432,Bρ_2 = 1.00, momentum acceptance = 3%, 100 mg/cm^2 plastic degrader) were taken from the initial experimental settings for the A1200. In Figure 2.5, stable nuclides are shown in gray, and satellite beams expected to be observed with the ^{38}S are shown in yellow. Relative intensities have been normalized setting the ^{38}S rate = 100. It should be mentioned that the A1200 was retuned several times during the experiment due to loss of beam for various reasons, and so the final settings (and relative satellite intensities) were almost certainly not the same as the initial settings. The estimates shown in Figure 2.5 will be compared in Section 2.3.4 with the satellite beams actually observed during the experiment.

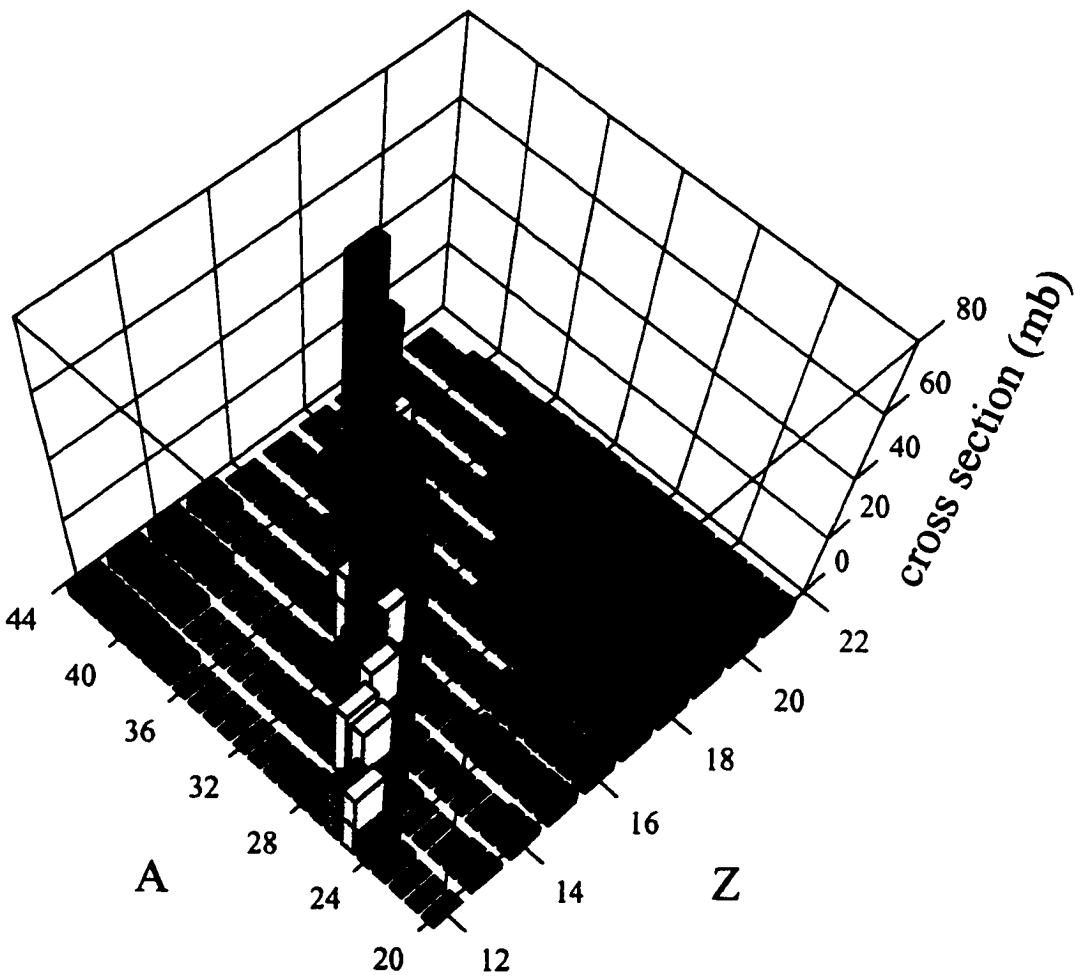

FIGURE 2.4. INTENSITY predictions of fragmentation products for 40 MeV/A ^{40}Ar incident on a 141 mg/cm^2 ^{9}Be target, before separation in the A1200.

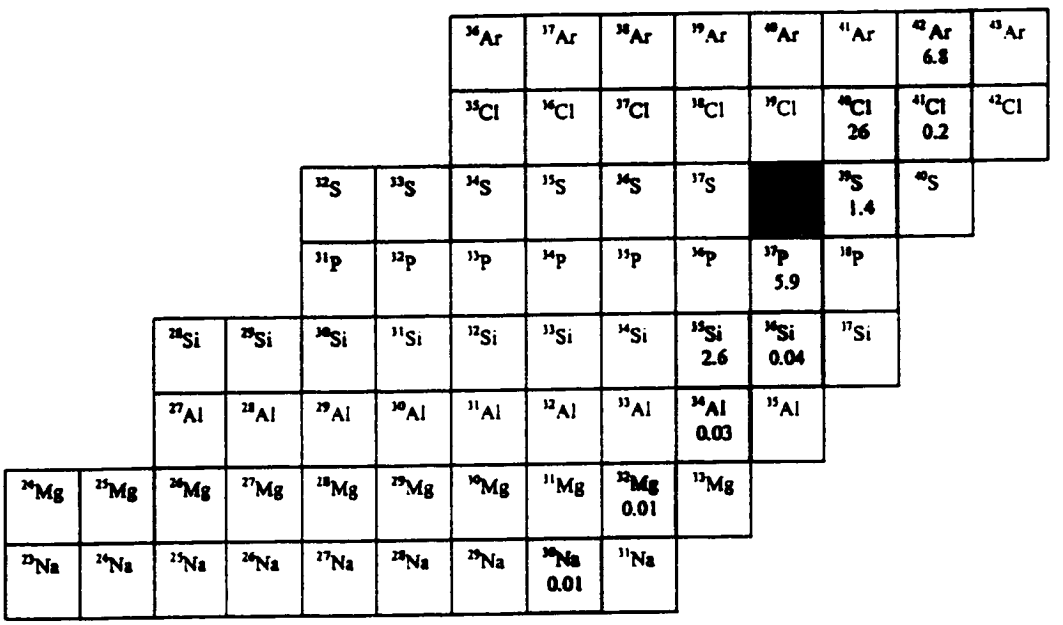

FIGURE 2.5. INTENSITY simulation of relative rates of secondary beams after passage through the A1200. Stable nuclides are shown in gray; predicted secondary beams are shown in yellow, and relative intensities are given normalized to a ^{38}S intensity of 100 units.

2.3.2. Chamber setup

After separation in the A1200, the secondary ^{38}S beam, with a final energy of 8 MeV/A (as measured by time of flight in the A1200), was sent to the 92" scattering chamber. The experimental setup inside the 92" chamber consisted of a degrader wheel, two sets of detectors for beam timing and imaging, a set of fission detectors, and a silicon detector at the end of the beamline to monitor beam intensity and characteristics. A schematic diagram of the apparatus is shown in Figure 2.6. At the entrance to the chamber was mounted a wheel with twelve apertures of 3 cm diameter. Aluminum foils ranging in thickness from 1.6 to 14 mg/cm^2 were mounted over eleven of these holes to degrade the ^{38}S beam from 8 MeV/A to the desired reaction energies. The post-degrader beam energies are given in the description of observed beam characteristics in Section 2.3.4. The wheel was attached to a stepper motor so that rotation of the foils into the beamline could be controlled from outside the chamber. After the beam passed through the degrader, an image of the beam spot was obtained using an x-y position-sensitive parallel-plate avalanche counter (PPAC) detector [Swa94] with 5 cm $\times$5 cm active area, which also served as the first element of the beam timing system. The beam spot for a typical run from the second experiment was 1.5 to 2 cm in diameter before degradation in the chamber.

The beam timing system consisted of two pairs of detectors mounted on a support arm extending roughly one meter from the beam entrance to the table supporting the fission detectors. For the second experiment, the support arm was mounted on a movable rail, so that the entire beam timing system could be rotated out of the path of the beam during high-intensity stable-beam calibration runs. The outer pair of timing detectors were PPACs: the beam-imaging PPAC mentioned previously and a second 10 cm $\times$10 cm PPAC 114 cm downstream, from which

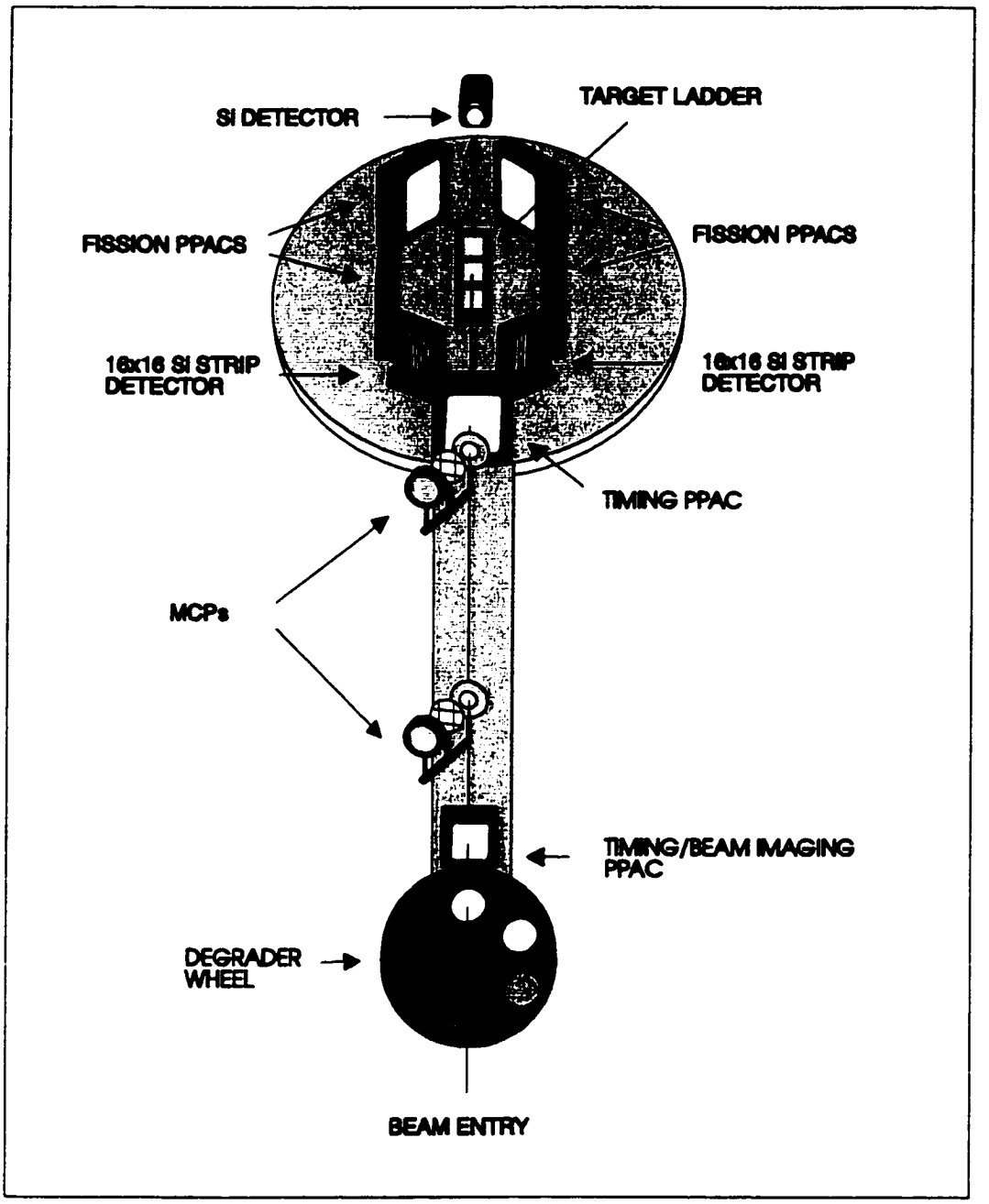

FIGURE 2.6. Schematic diagram of the experimental setup for the RNB experiments.

no imaging signals were taken. Between the PPACs were a pair of microchannel plate detectors (MCPs) [Bat97] separated by a flight path of 93 cm (97 cm in the second experiment). A microchannel plate is a glass disc or annulus with thousands to millions of pores, each typically a few microns in diameter, etched through it. These channels are coated with CsI, which releases multiple secondary electrons when struck by an energetic electron. A potential difference is placed across the MCP to accelerate electrons from one side to the other, and charge is collected at the anode at the back of the detector. Thin aluminum or aluminum oxide foils were placed in the beamline at an angle of 45° as electron emitter foils for the MCPs, and wire grids were used to focus the electrons onto the MCPs. In the first experiment, the emitter foil thicknesses were 3.09 mg/cm^2 Al (upstream) and 60 μg/cm^2 Al_2O_3 on 10 μg/cm^2 Au (downstream); in the second experiment, both emitter foils were 1.62 mg/cm^2 Al. The detectors themselves were set at backward angles out of the beamline. 1.75 cm diameter collimators were placed in front of the MCPs during the second experiment to reduce scattered beam background. The PPACs showed a time resolution of 1.5 ns FWHM for the one-meter flight path, and the MCP time resolution was 530 ps FWHM, as measured using a stable ^{40}Ar beam of 300.9 MeV. (The beam energy spectrum in the Si detector at the end of the beamline had a FWHM of 2.5 MeV, which corresponds to a spread in time-of-flight of 100 ps.) Time calibration spectra with the ^{40}Ar beam are shown in Figure 2.7. The time resolution of the ^{38}S spectra was limited by the energy spread of the beam.

Efficiency of the timing system was calibrated by measuring the percentage of ^{38}S beam particles implanted in the silicon detector at the end of the beamline which had triggered a coincidence signal in the ^{38}S time-of-flight peak for each pair of timing detectors. The efficiency of the MCPs was 95-99%, and PPAC efficiency was measured to be $>99\%$. Both of the timing systems together recorded 99.9%

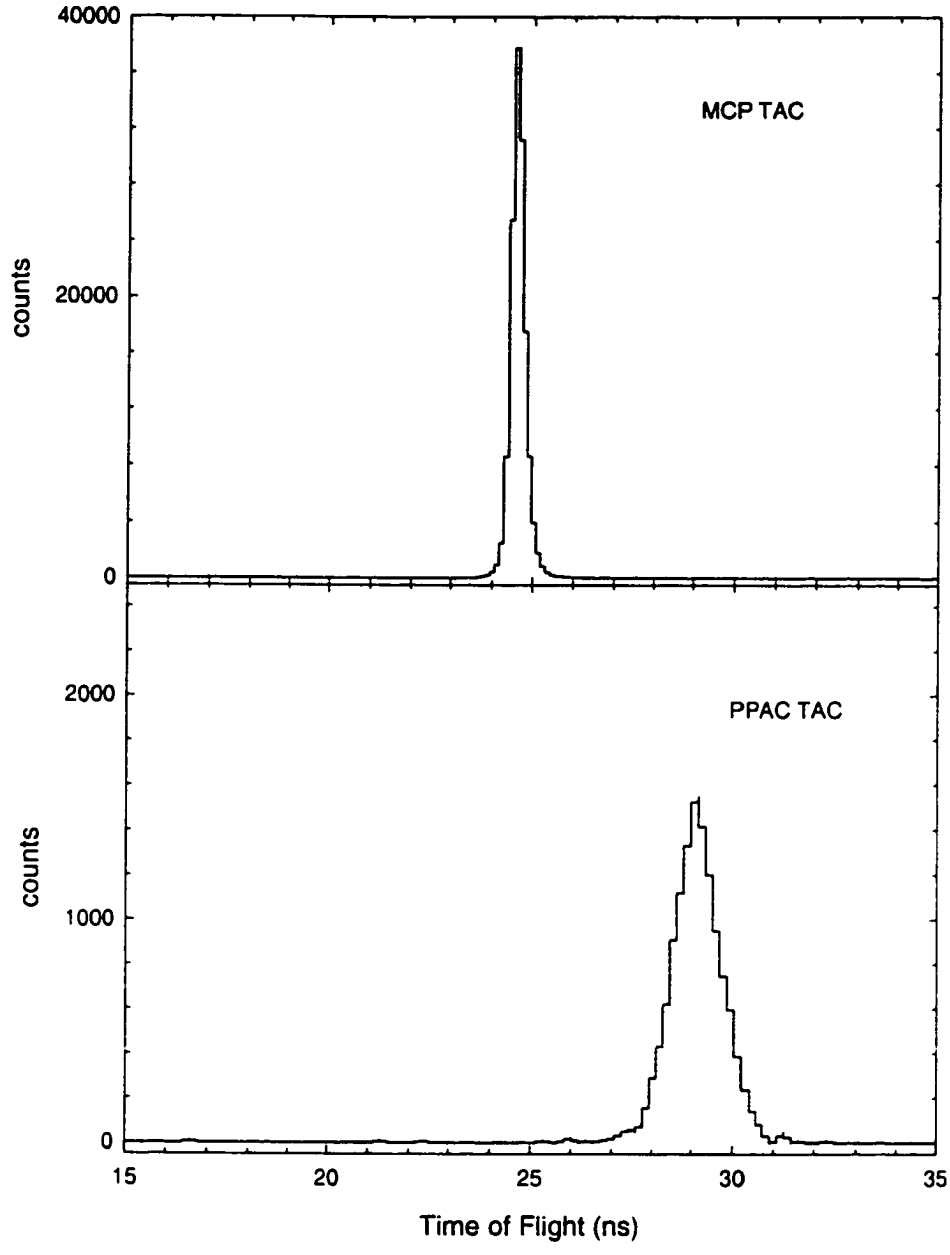

FIGURE 2.7. Time-of-flight calibration spectra for the timing PPACs and MCPs, with a stable ^{40}Ar beam of 300.9 MeV (after passage through all detectors and foils). The difference in time of flight between the two spectra reflects the longer flight path between the PPACs.

of the ^{38}S beam particles. (The ^{38}S rates in the silicon detector were about 500 particles/second for these runs, and the total beam rates were less than 700/second, time-averaged over the runs. This corresponds to more than 1 ms average time between particles, which is ample resolving time for the detectors.) Because of the low beam intensity, the beam timing system could be used to give event-by-event time of flight information for the radioactive beam. The MCPs were used as the primary source of timing data due to their better resolution, with the PPACs as a backup system.

After passing through the timing system, the beam struck a 2 cm $\times$2 cm ^{181}Ta target in the center of the chamber. The targets were self-supporting, with a mean thickness of 0.924 mg/cm^2 for the first experiment, and 0.857 mg/cm^2 for the second. (These targets were also made by the Uppsala targetmaker, as described in the previous section, and had an uncertainty in thickness of about 10%.) A remotely movable target ladder allowed for rotation of the targets to 40° for some runs, in order to increase the thickness presented to the beam.

Two 500 μm 16$\times$16 silicon strip detectors were placed at backward angles from the target with the p$^+$ (vertical strips) side facing the target. The detectors were at $\pm$155° (lab), at a distance of 14.6 cm. Each detector had an active area of 47 mm $\times$47 mm and covered 0.101 sr solid angle; the strips were chained together into a 4 vertical $\times$ 1 horizontal configuration. Positive bias was applied to the vertical strips in order to collect the fast negative signals; the horizontal side was left at ground potential to collect the slower positive signals. For the second experiment, the strip detectors were removed due to operating difficulties, and were replaced by an array of silicon surface barrier detectors. Eight 300 mm^2 Si detectors of 100 μm thickness were used, mounted four on each side of the beam in a square configuration which subtended 75% of the original strip detector's solid angle coverage. The signals

from the strips and Si detectors were used to detect fission fragments at backward angles, but also to look for alpha particles from any heavy residues that may have survived. No residue alphas were observed for any of the data runs, which puts an upper limit on the heavy residue cross section of 3% of all events. Alpha spectra for these backward detectors, along with details of the upper-limit calculation and comparison to theoretical predictions for residue cross sections, will be given in the description of the data analysis in Chapter 4.

Four 10 cm $\times$10 cm x-y position-sensitive PPACs were placed around the target in order to detect fission fragments. Two detectors were centered at $\pm 25°$ (lab frame) at a distance of 20 cm from the target, and two were at $\pm 90°$ and a distance of 6.5 cm. The position resolution of the PPACs was $\leq$ 5 mm as measured using a plastic mask and a ^{252}Cf calibration source. The PPACs were filled with isobutane gas at 5 to 8 torr and held applied voltages from +500 to +750V. (The operating pressure and voltage can be tuned to optimize the signal, depending on incident particle energy loss in the detector gas.) The four "fission PPACs" covered a total solid angle of 20% of 4π in the lab frame; this large area coverage was crucial to compensate for the low beam intensities. The efficiencies of these four detectors for fission fragments ranged from 85% to 88% as measured with a ^{252}Cf source. Although the PPACs subtended large solid angles and gave position information, they are transmission detectors, and so total energy of the incident particles was not recorded. Since the detectors were also sensitive to other reaction products such as scattered beam, transfer products, and target recoils, separation of fusion-fission from other events had to be accomplished by observing angular correlations between pairs of coincident particles.

Another Si surface barrier detector with area 100 mm^2 and thickness 500 μm was placed downstream from the target. This detector was mounted on an

arm attached to a movable rail, and was placed in the beam path to observe the intensity and characteristics of the radioactive beam. The rail on which this detector was mounted, which also acted as the base for the timing apparatus as mentioned previously, enabled the entire set of detectors for timing and beam imaging to be rotated out of the beamline for high-intensity stable-beam calibration runs. The range of rotation was ±30°, which allowed for ample clearance of all detectors during these calibrations. At the end of the beamline, a Faraday cup was attached to the exit line from the chamber. This was connected to a current integrator in the data acquisition area, and was used to measure beam current for the high-intensity beams.

The total efficiency of the detector system was determined by measurement of the known fission cross section for the reaction of ^{16}O + ^{197}Au [Vio63] as will be described in Chapter 4. Time-of-flight and energy calibrations were made using well-defined primary beams of ^{40}Ar at four energies in the first experiment, and of ^{16}O at three energies in the second.

2.3.3. Data acquisition

The electronics setup for the radioactive beam experiments was similar to that of the stable-beam ^{32}S measurements. Figure 2.8 shows a schematic diagram of the electronics. Energy signals for the silicon detectors and position signals for the PPACs were sent through preamplifiers to shaping amplifiers and ADCs. Fast timing signals from the PPACs and MCPs of the beam timing system were sent through fast amplifiers and discriminators to TDCs to allow time-of-flight calculation in software; time of flight was also measured directly for each pair of timing detectors using time-to-analog converters (TACs) which were read into ADCs. A

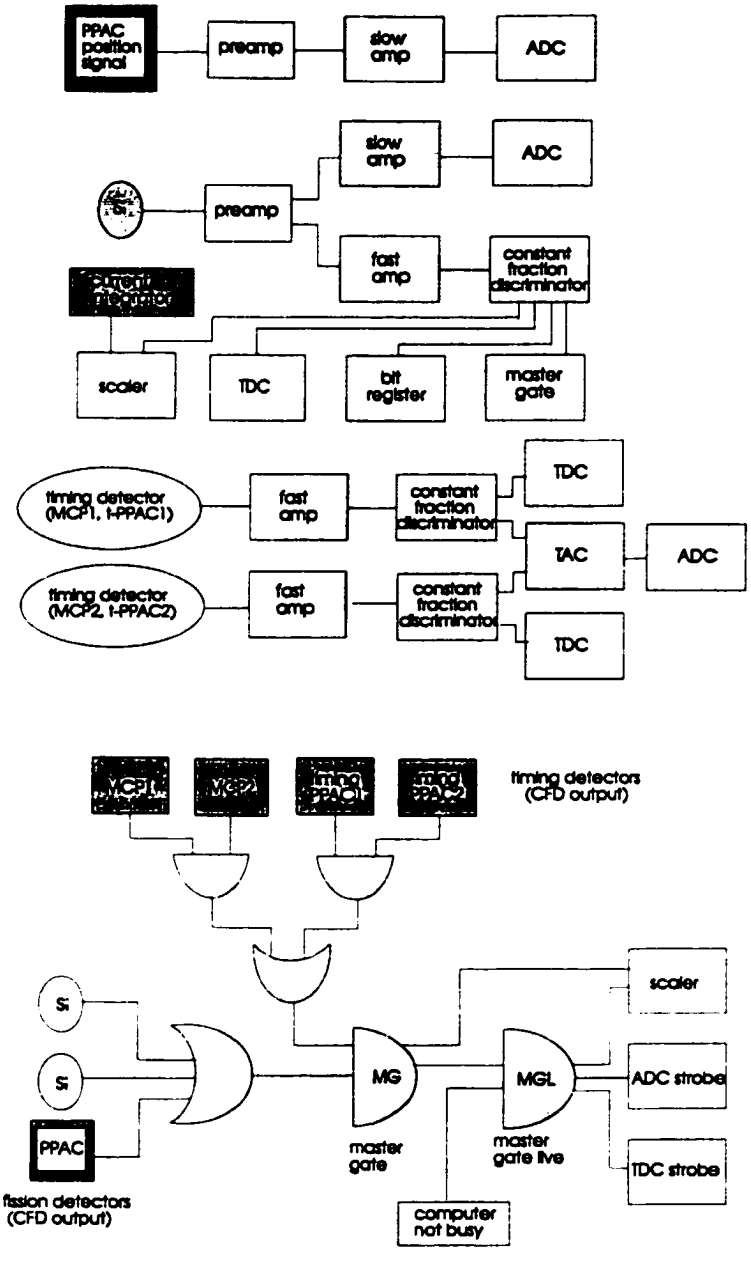

FIGURE 2.8. Schematic diagram of the electronics for the radioactive beam experiments.

fast time signal was taken from each of the fission detectors (fission PPACs and silicons) as well, and sent to a constant fraction discriminator to eliminate low-level noise and generate a fast timing signal. The logic outputs of these CFDs were used in the master gate logic to determine a valid event.

A valid event for the data runs was defined as a coincidence signal in either of the two timing systems, in coincidence with a signal from any fission detector. (These events were further restricted in the data analysis to require a timing + fission + fission triple coincidence.) For runs to measure beam characteristics, an event was defined as a timing coincidence or a signal from the silicon detector at the end of the beamline. The master gate was used in a logical .AND. with a not-busy signal from the computer to form the master gate live; as in the ^{32}S experiment, this was the strobe to trigger readout of an event. Also as in the ^{32}S experiment, all detector signals, as well as the master gate, master gate live, and beam current integrator, were monitored with scalers that were independent of the event logic. The ADCs, TDCs, scalers and bit register (which recorded which detector(s) triggered an event) were read using a CAMAC system controlled by the standard NSCL data acquisition software [Fox89]; data was written to tape and sent to a workstation running the SARA analysis program [She94].

2.3.4. Beam characteristics

Typical energy and time-of-flight spectra for the ^{38}S radioactive beam are shown in Figures 2.9 and 2.10, and a plot of energy vs. time of flight is given in Figure 2.11. It can be seen that, although the ^{38}S is the major component of the beam, there are several satellite impurities as well. These figures show the "undegraded" radioactive beam; that is, with the timing apparatus in the beamline

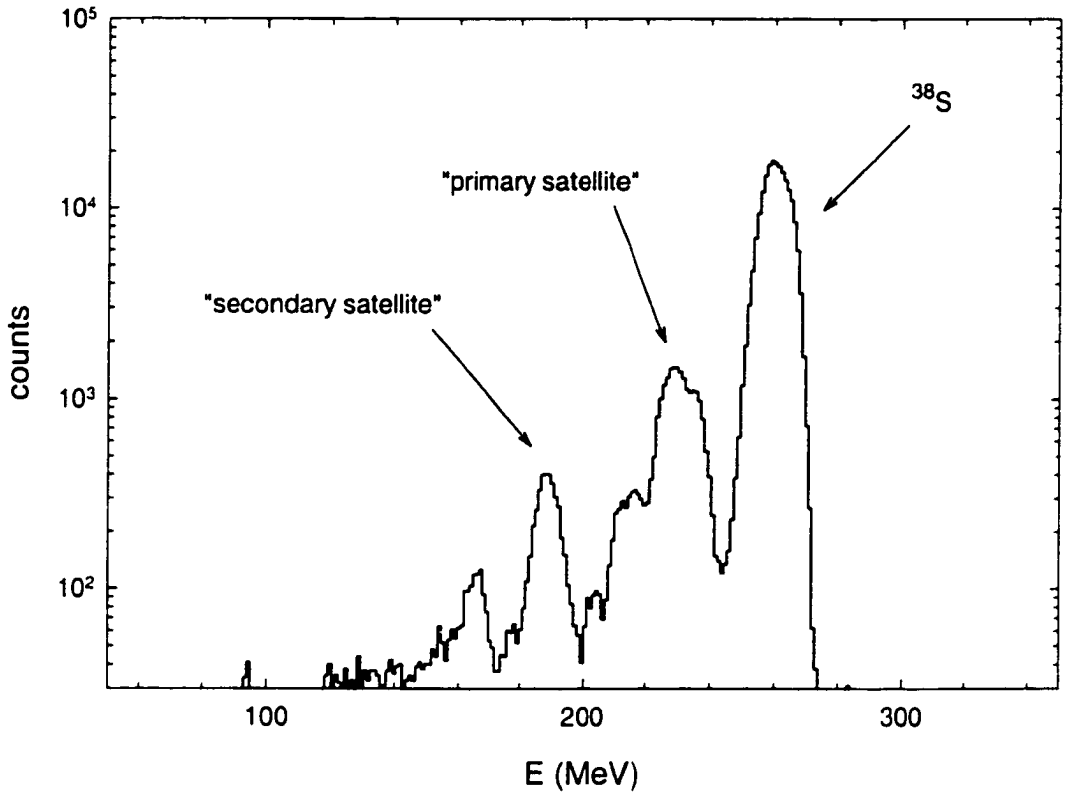

FIGURE 2.9. Energy spectrum of the ^{38}S radioactive beam.

as the only degraders. With increasing energy degradation using the aluminum foils at the entrance to the chamber, the ^{38}S and satellite beams became more separated in energy; and so these figures show the worst-case scenario for separation of the ^{38}S from other components of the beam. Energy and time-of-flight data and relative beam intensities for ^{38}S and the two largest satellites for all the measured energies are given in Table 2.1.

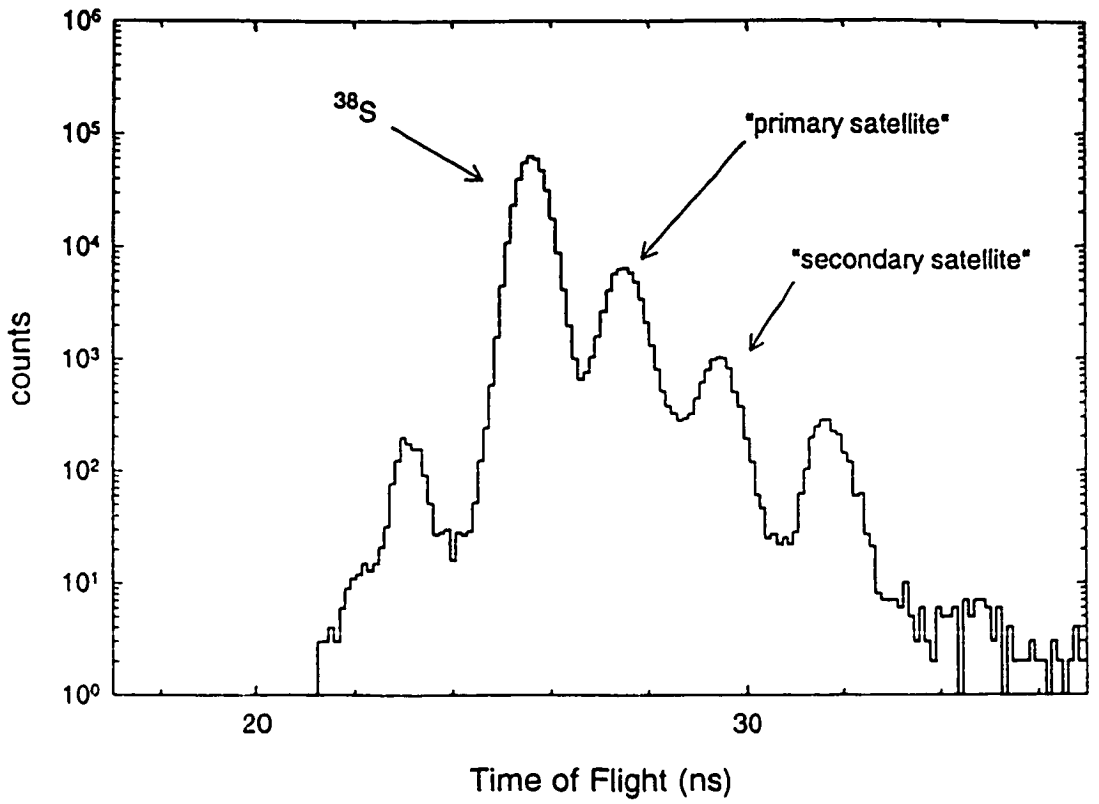

FIGURE 2.10. Time-of-flight spectrum for the ^{38}S radioactive beam.

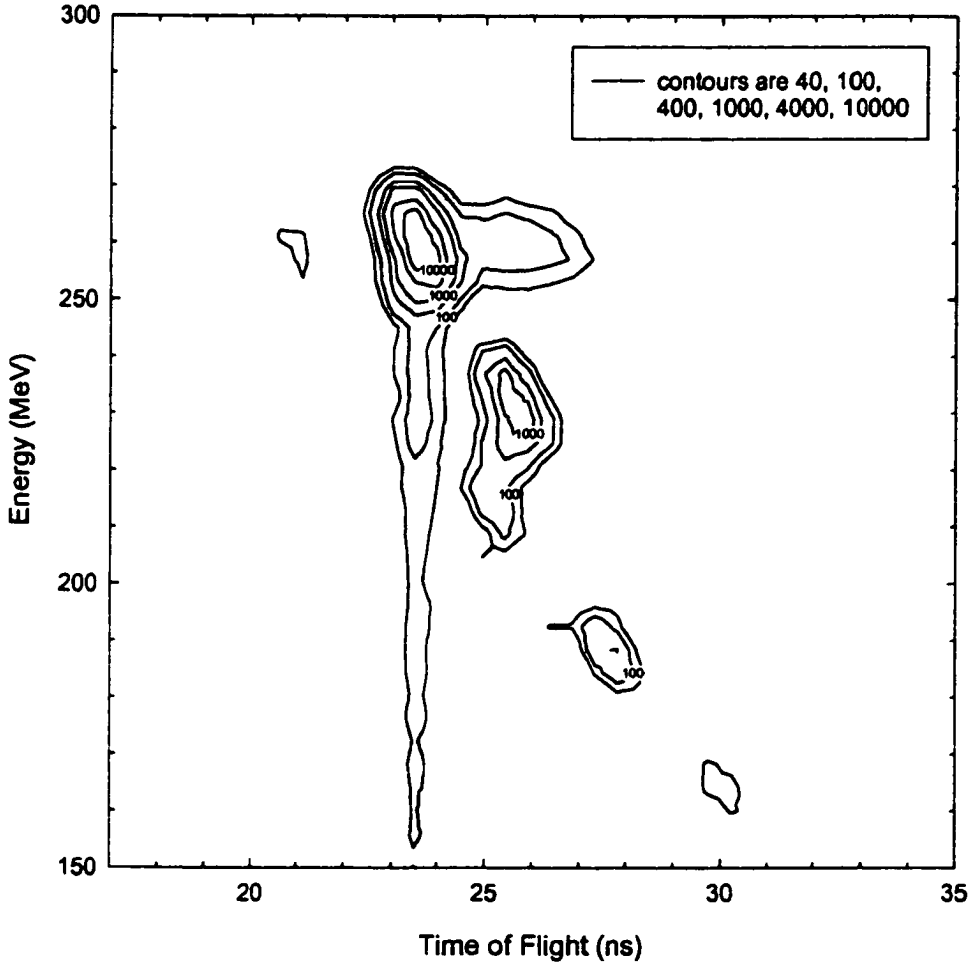

FIGURE 2.11. Energy vs. time-of-flight for the ^{38}S radioactive beam.

TABLE 2.1. Measured energy, time of flight, and relative beam intensities for ^{38}S and the two largest satellites. Energies are those observed in the silicon detector at the end of the beamline, while time-of-flight data is before energy loss in the second PPAC and MCP of the timing system.

	beam component	initial degrader thickness (mg/cm^2 Al)	observed final energy (MeV)	observed time of flight (ns)	intensity relative to ^{38}S
Expt 2	^{38}S	0	256.1 ± 3.6	25.63 ± 0.59	
	satellite 1		226.9 ± 3.2	27.63 ± 0.76	0.12
	satellite 2		185.7 ± 2.6	29.62 ± 0.75	0.02
	^{38}S	1.64	239.9 ± 3.4	26.15 ± 0.71	
	satellite 1		209.6 ± 2.9	28.07 ± 0.82	0.13
	satellite 2		171.3 ± 2.4	29.88 ± 0.89	0.02
	^{38}S	5.12	206.7 ± 2.9	28.02 ± 0.78	
	satellite 1		173.3 ± 2.4	31.18 ± 1.17	0.13
	satellite 2		139.0 ± 2.0	33.67 ± 1.10	0.02
	^{38}S	7.79	185.1 ± 2.6	29.26 ± 1.01	
	satellite 1		137.8 ± 1.9	33.00 ± 1.27	0.14
	satellite 2		105.9 ± 1.5	35.46 ± 1.11	0.02
Expt 1	^{38}S	0	256.8 ± 5.6	25.60 ± 0.87	
	satellite 1		223.4 ± 4.8	27.84 ± 0.96	0.15
	^{38}S	3.09	215.8 ± 4.7	27.17 ± 0.88	
	satellite 1		181.3 ± 3.9	30.13 ± 0.98	0.10
	^{38}S	6.55	187.9 ± 4.1	29.12 ± 0.89	
	satellite 1		146.7 ± 3.2	33.47 ± 1.02	0.09
	^{38}S	9.27	158.6 ± 3.4	31.21 ± 0.89	
	satellite 1		104.9 ± 2.3	37.92 ± 1.09	0.10

Maximum beam intensities on target ranged from 2000 to 10,000 particles/second, with the ^{38}S as 85% to 90% of the total flux. In order to be sure that the observed fission fragments were induced by the ^{38}S beam, event-by-event time-of-flight information was used. A triple coincidence of timing + fission + fission was required to define a valid event. Time-of-flight gates were then used in the data analysis to associate fission-fission coincidences with the ^{38}S or with the satellite beams. True fusion-fission events (as defined by correct folding angle and coincidence with a ^{38}S particle through the timing detectors) occurred at rates ranging from about two per hour at the highest energies to roughly one event every 2.5 hours at the lowest energies. Running times were from 7-16 hours of data per energy (which typically translates into more than 24 hours of real time).

Although the ^{38}S was identified and selected by its flight path and energy loss measurements in the calibrated A1200 spectrometer, it is worthwhile to ask if the beam identity can be confirmed by time-of-flight and dE/dx measurements as the beam was degraded to lower energies in the chamber. Energy loss through a degrader depends quadratically on Z of the projectile, and so dE/dx can be used for elemental identification. (Typically this is measured with a ΔE-E series of silicon detectors, but for the present measurements was calculated using the observed final energy after passage of a series of foils of known thickness.) Time of flight for a known beam energy is proportional to $\sqrt{A}$, and so can be used to estimate the projectile mass.

Figures 2.12 and 2.13 show energy-loss calculations for ^{38}S for the two experiments, compared to the observed final energies. These values are also given in Table 2.2. The calculated values were obtained by using the observed final energy for the measurement with no initial degrader to calculate an initial beam energy into the chamber before passage through the timing apparatus. From this initial energy,

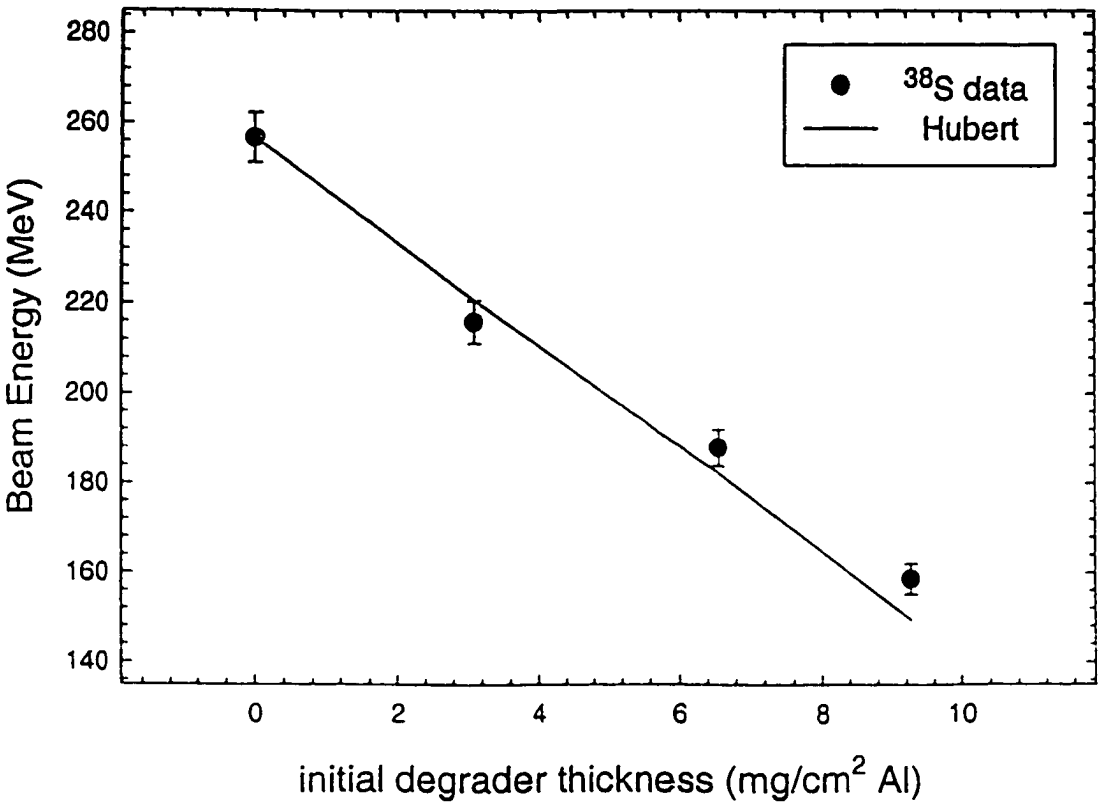

FIGURE 2.12. ^{38}S energy-loss calculations, first experiment

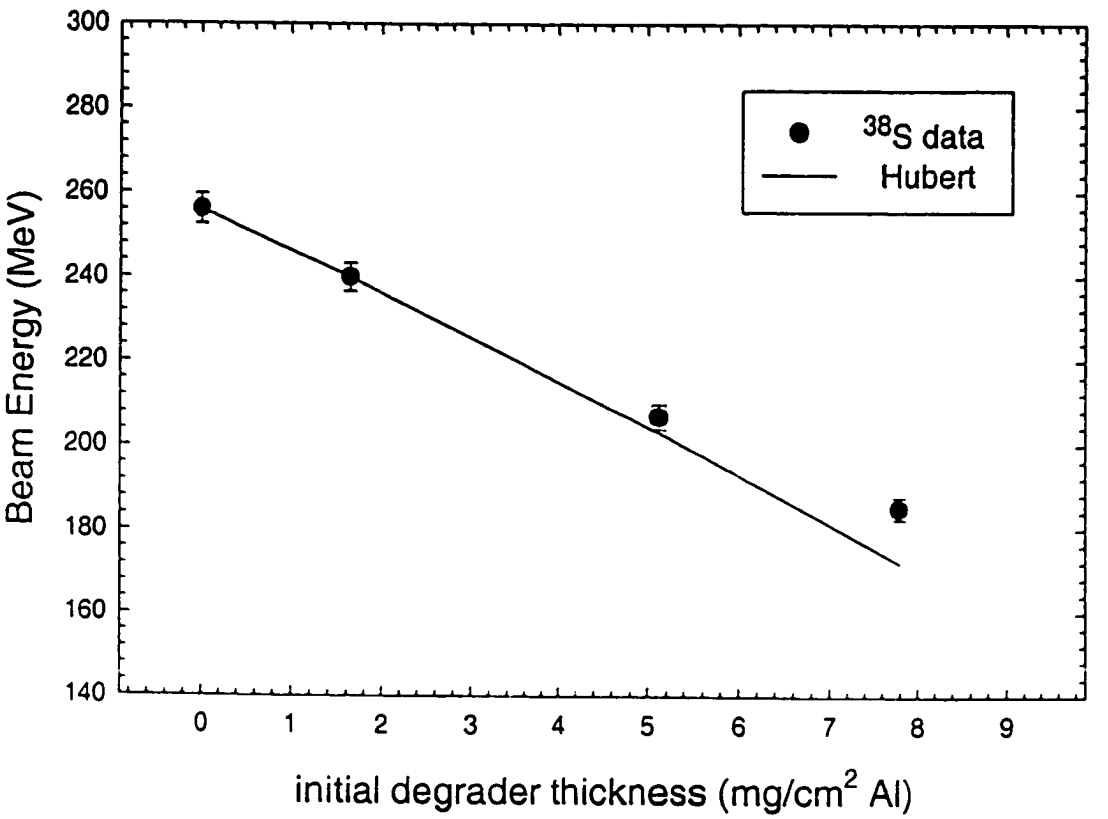

FIGURE 2.13. ^{38}S energy-loss calculations, second experiment

TABLE 2.2. Energy-loss and time-of-flight calculation results for ^{38}S and the two largest satellite beams. Energies are calculated at the final silicon detector after passage through all elements of the timing system; runs marked '*' include passage through the Ta target as well. Time of flight is based on calculated energy before the second elements of the timing system, deduced from observed final energies in the silicon detector.

	beam component	initial degrader (mg/cm^2)	calculated final energy (MeV)	observed final energy (MeV)	calculated time of flight (ns)	observed time of flight (ns)
Expt 2	^{38}S	0	256.1	256.1 ± 3.6	25.56	25.63 ± 0.59
	satellite 1		226.9	226.9 ± 3.2	27.20	27.63 ± 0.76
	satellite 2		185.7	185.7 ± 2.6	29.10	29.62 ± 0.75
	^{38}S	1.64	239.9	239.9 ± 3.4	26.18	26.15 ± 0.71
	satellite 1		209.2	209.6 ± 2.9	27.99	28.07 ± 0.82
	satellite 2		171.6	171.3 ± 2.4	30.04	29.88 ± 0.89
	^{38}S	5.12	203.0	206.7 ± 2.9	27.81	28.02 ± 0.78
	satellite 1		168.6	173.3 ± 2.4	30.13	31.18 ± 1.17
	satellite 2		136.5	139.0 ± 2.0	32.54	33.67 ± 1.10
	^{38}S	7.79	172.1	185.1 ± 2.6	29.04	29.26 ± 1.01
	satellite 1		134.3	137.8 ± 1.9	32.75	33.00 ± 1.27
	satellite 2		106.6	105.9 ± 1.5	35.63	35.46 ± 1.11
Expt 1	^{38}S	0	256.8	256.8 ± 5.6	25.36	25.60 ± 0.87
	satellite 1		223.4	223.4 ± 4.8	27.44	27.84 ± 0.96
	^{38}S	3.09*	220.7	215.8 ± 4.7	27.25	27.17 ± 0.88
	satellite 1		183.8	181.3 ± 3.9	29.85	30.13 ± 0.98
	^{38}S	6.55*	182.4	187.9 ± 4.1	29.01	29.12 ± 0.89
	satellite 1		141.0	146.7 ± 3.2	32.77	33.47 ± 1.02
	^{38}S	9.27*	149.3	158.6 ± 3.4	31.28	31.21 ± 0.89
	satellite 1		103.5	104.9 ± 2.3	37.73	37.92 ± 1.09

calculations were then made to predict final energies after passage of the various ^{27}Al degrader foils and the timing apparatus for the other three runs. All dE/dx calculations were made using the program RANGE [Lil95], which interpolates values using the range-energy correlations of Hubert *et al.* [Hub90]. At low energies, these predictions are accurate to about six percent [Hub90]. It can be seen that the measured beam energies are in agreement with predictions for ^{38}S, within the accuracy of the model. (This method is fairly insensitive to errors in the thickness of the Al foils and PPACs, due to the fact that the initial energy was obtained from back-calculation through these elements. Changing the foil thicknesses resulted in different initial energies, and so the calculated final energies for the degraded-beam runs remained similar. For example, decreasing the PPAC thicknesses by 35% resulted in a 4.7% difference in final energy at the lowest measured data point, where the effect is largest; and changing the MCP foil thicknesses by 0.4 mg/cm^2, which corresponds to a 10 mg weighing error, shifted the final energy down by only 2.6 MeV at the lowest measured data point. The slope of the line, which is the key to elemental identification, was extremely insensitive to changes in degrader thickness.) Time-of-flight predictions and masses calculated from the measured time of flight are shown in Figures 2.14 and 2.15, and are also in agreement with the beam identification as ^{38}S. For the first experiment, in addition to the degrader thicknesses listed in Table 2.2, the first MCP foil was 3.09 mg/cm^2, set at 45°, and the second foil was 60 μg/cm^2 Al_2O_3. Runs marked with an asterisk in Table 2.2 also had a 0.924 mg/cm^2 Ta target in place. For the second experiment, both MCP foils were 1.62 mg/cm^2 Al set at 45°, and no target was in place. The PPACs were taken to have a thickness of 0.68 mg/cm^2 carbon equivalent [Yur99] for all calculations.

The same procedure was used to make nominal identifications of the two most intense satellite beams. The primary satellite, which accounted for roughly 10% of

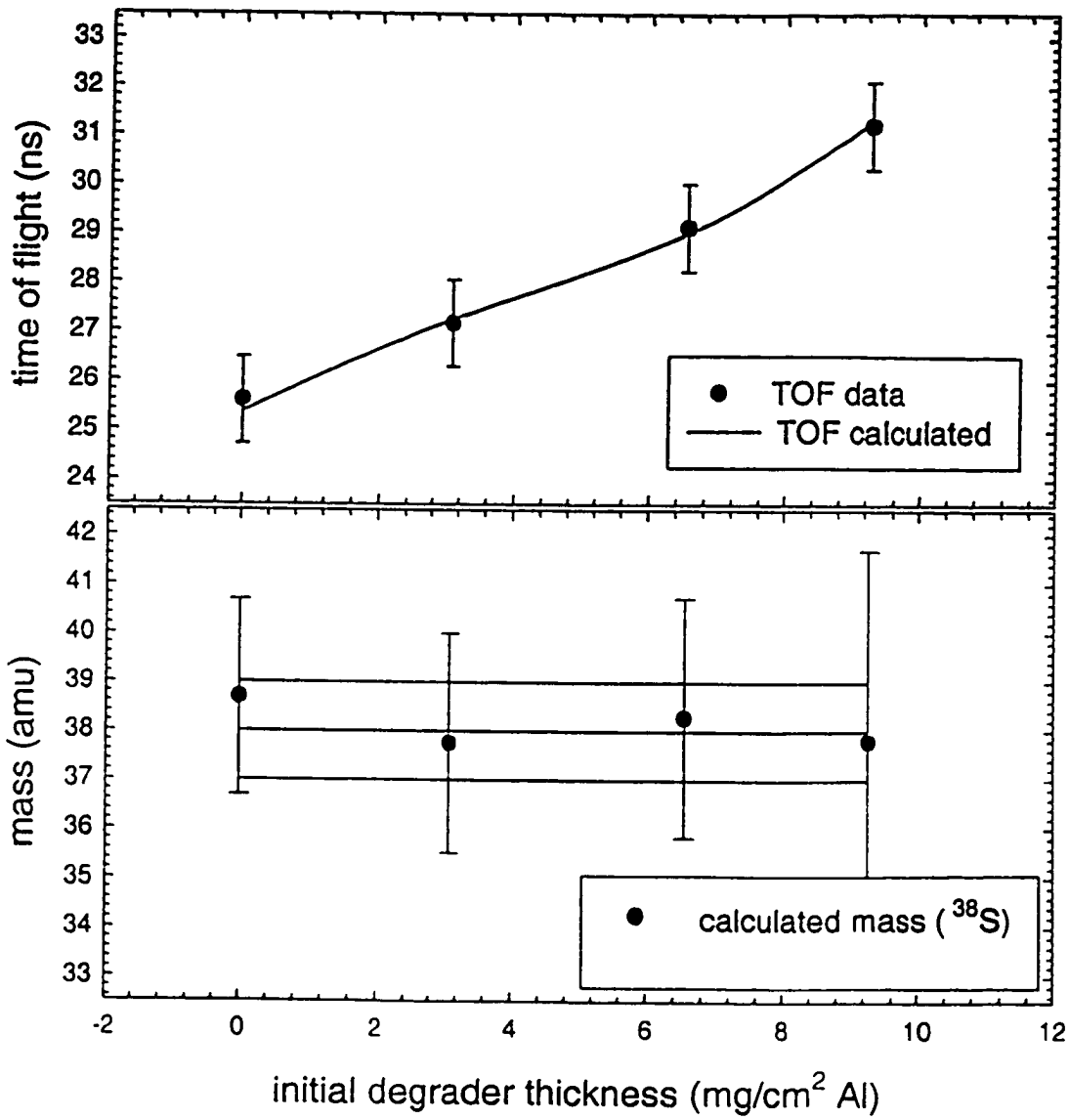

FIGURE 2.14. Time-of-flight predictions and calculated masses for the ^{38}S beam, first experiment.

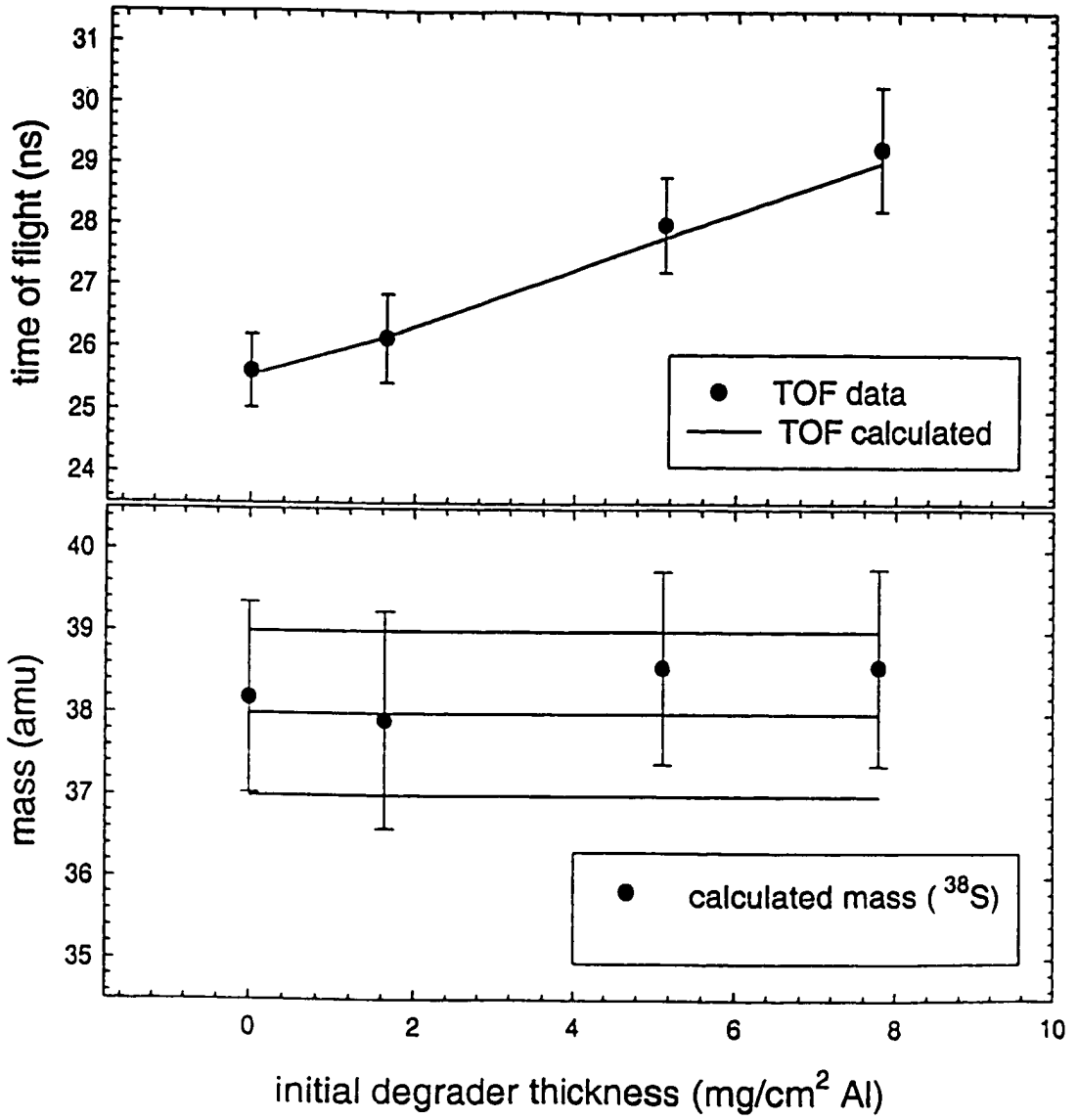

FIGURE 2.15. Time-of-flight predictions and calculated masses for the ^{38}S beam, second experiment.

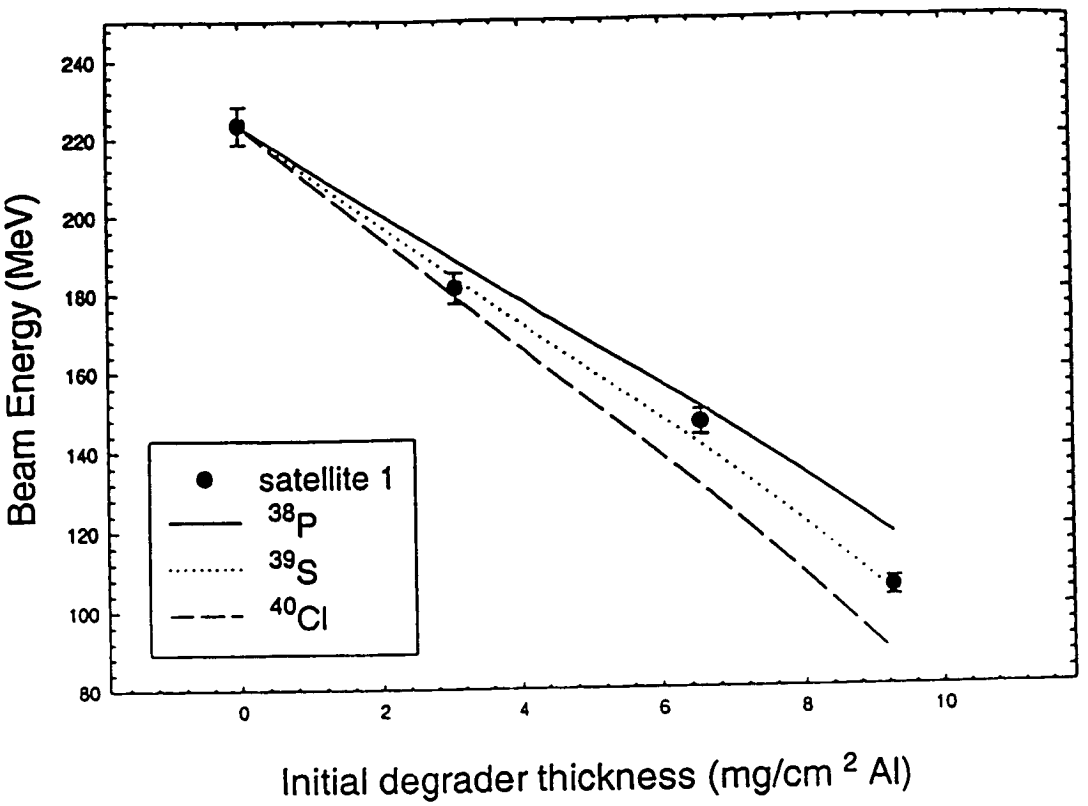

FIGURE 2.16. Energy-loss calculations for the primary satellite, first experiment

the beam, remained separable through the degraded-energy runs; but the secondary satellite spectra were not clean for the lower energy runs, and so identification is tentative (and was not possible for the first of the two experiments). The secondary satellite accounted for only 1-2% of the beam, and did not trigger any fission events, and so did not have any large effect on the experiments. Figures 2.16 and 2.17 show energy-loss calculations for the primary satellite for the two experiments. The measured data agree with the energy-loss calculations for sulfur; time-of-flight and

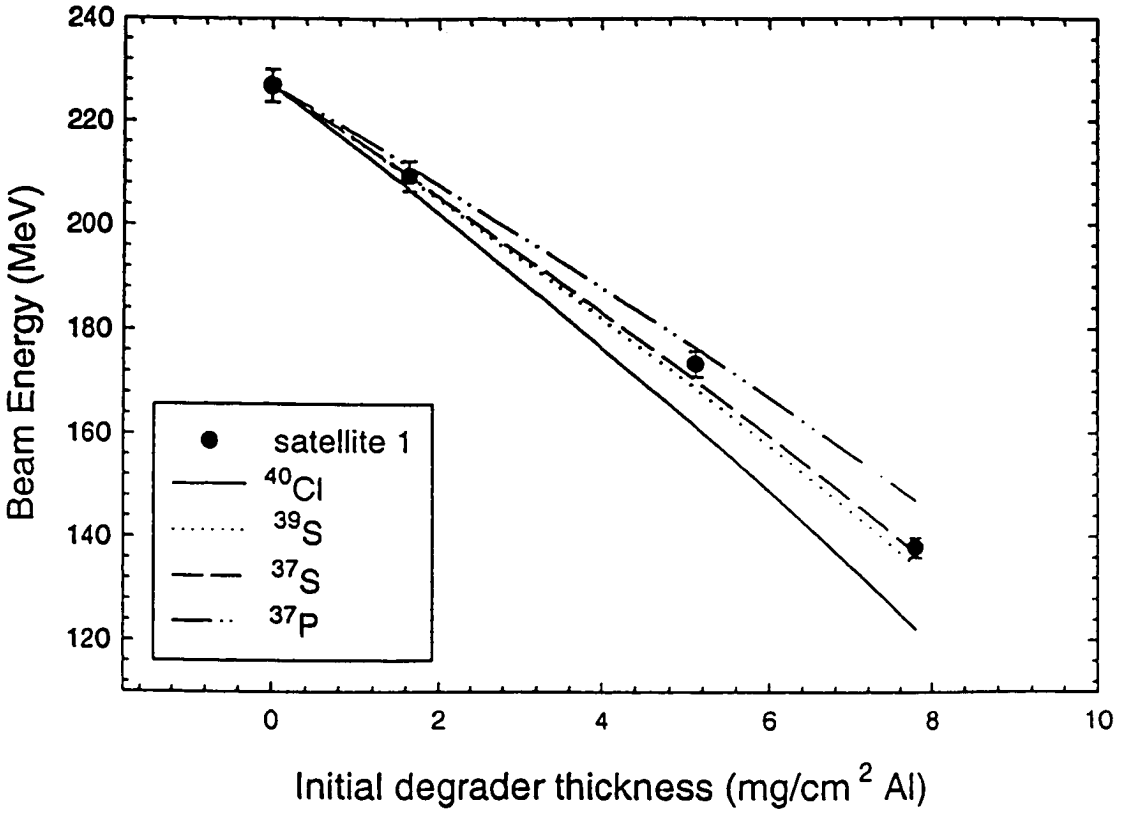

FIGURE 2.17. Energy-loss calculations for the primary satellite, second experiment

mass calculations (shown in Figures 2.18 and 2.19) show a best fit to ^{39}S (reduced χ^2 = 0.40, first experiment; 0.25, second experiment) or ^{40}S (reduced χ^2 = 0.28, first experiment; 0.25, second experiment). Energy-loss and time-of-flight plots for the secondary satellite for the second experiment are shown in Figures 2.20 and 2.21. The data match the energy-loss predictions for silicon; the time-of-flight data, however, were not easily separable from nearby satellites, and so the mass cannot be unambiguously determined. (It is possible that multiple beams are included in this data.) Reduced χ^2 for a fit in time of flight to ^{37}Si was 0.54, however, so this is one tentative identification. Comparing these identifications with the simulation predictions given in Figure 2.5, it can be seen that although ^{39}S is a possible satellite, the predicted silicon isotopes are all lighter than ^{37}Si. The time-of-flight data for the secondary satellite were not always cleanly separable, though, so error in the calculated masses is likely. It is also noted that the observed satellites are both lighter elements than those predicted to have the highest intensities (^{40}Cl and ^{42}Ar); however, minor tuning of the A1200 can change the observed beam ratios. Given that the beam was retuned several times after the initial test runs (from which the settings used in the simulation were taken), a difference in relative satellite intensities between prediction and observation is not unreasonable.

2.4. Summary

The measurement of the stable-beam ^{32}S reaction used a straightforward experimental design. The beams were well-focused and well-defined, so collimation and precise time-of-flight measurements were unnecessary. Multiple silicon detectors were used in order to obtain angular distributions of the fission fragments, but

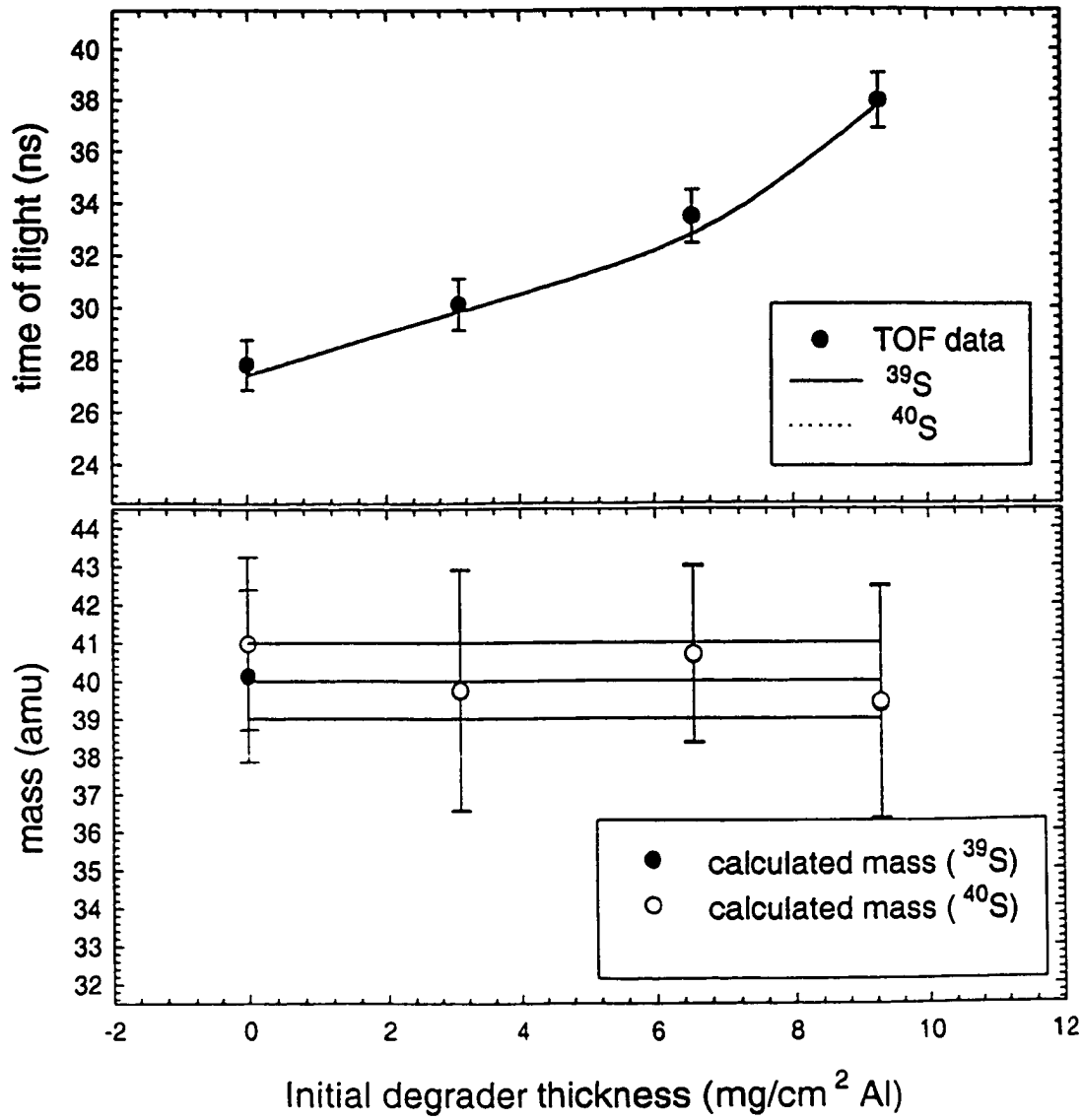

FIGURE 2.18. Time-of-flight and mass calculations for the primary satellite, first experiment

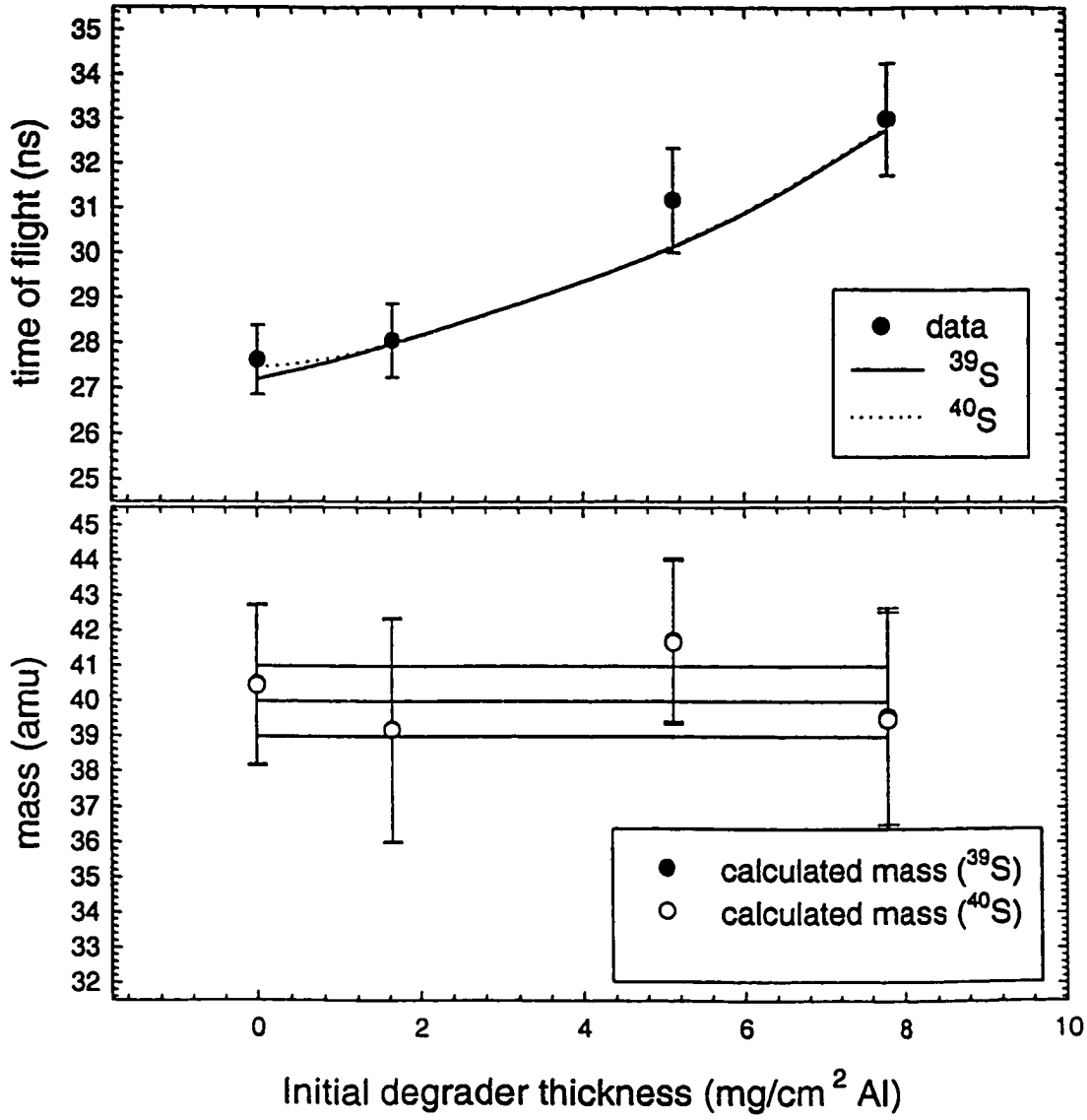

FIGURE 2.19. Time-of-flight and mass calculations for the primary satellite, second experiment.

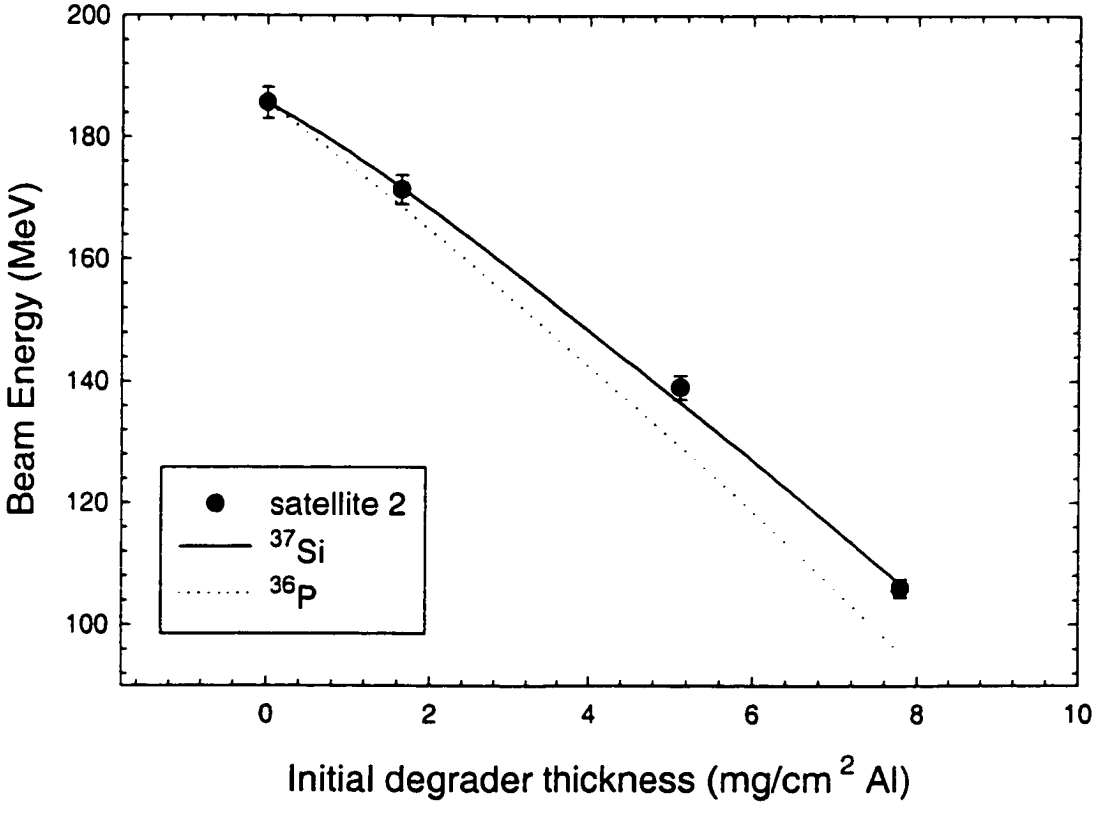

FIGURE 2.20. Energy-loss calculations for the secondary satellite.

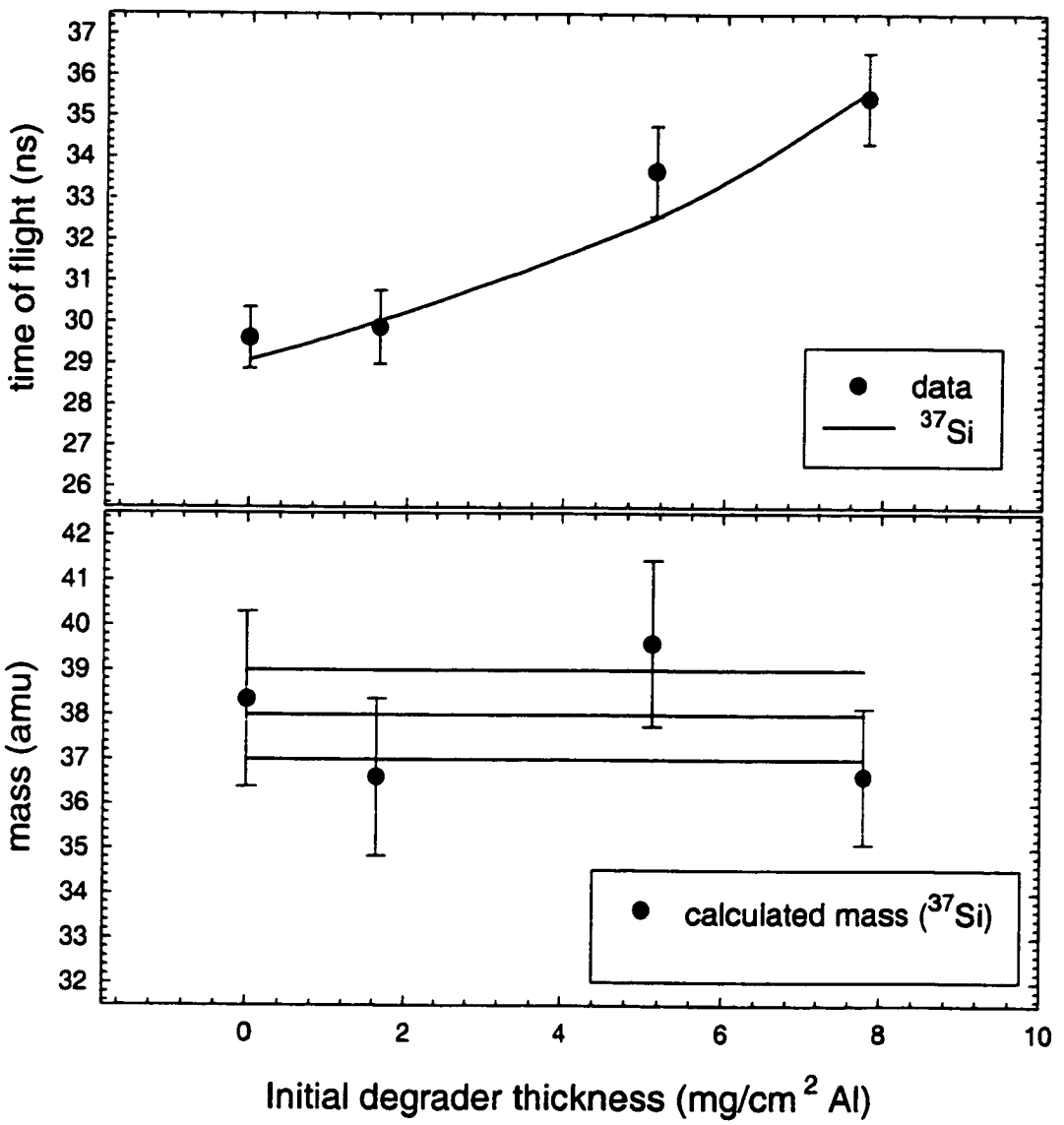

FIGURE 2.21. Time-of-flight and mass calculations for the secondary satellite.

beam currents were high enough that adequate statistics could be obtained in runs of an hour or less, without high solid angle coverage.

The radioactive beam measurements, in contrast, posed several significant challenges. Since elimination of all impurities in the secondary beam would be difficult or impossible, it was necessary to use a high-precision timing system to identify the beam particles on an event-by-event basis. Direct measurement of the energies with a silicon detector was also valuable in characterizing the radioactive beam. Since the beam spot was physically large (a few centimeters in diameter as compared with a few millimeters for a typical stable beam), some care had to be taken in balancing collimation to protect the detectors with losses in intensity due to the collimation and to straggling from the degrader foils. Finally, due to the low beam intensities, high solid angle coverage and measurements of 7 to 16 hours per energy were required in order to carry out a measurement of the fusion cross section.

In summary, reaction studies with radioactive beams, although feasible, pose a unique set of challenges, and require significant differences in experimental design as compared to typical stable-beam experiments.

3. $^{32}S + ^{181}TA$ DATA ANALYSIS

The objectives of the data analysis for the stable-beam $^{32}S + ^{181}Ta$ experiment were to use the measured fission data to determine the excitation function for the reaction and extract the fusion barrier from it. This was accomplished by an analysis of the fission fragment singles angular distributions, and separately by determination of coincident fission fragments with full linear momentum transfer. The fission excitation function was fitted to extract the fusion barrier and radius using both a classical method and a coupled-channels approach; good agreement between the two results was observed. This chapter will describe the methods used in the singles and coincidence analysis, and compare the results to various model predictions. In addition, an estimate will be made of the quasifission contribution to the reaction, in order to relate the fission cross section to the cross section for true complete fusion. Results of this data analysis will be used for comparison to the radioactive beam $^{38}S + ^{181}Ta$ reaction in Chapter 5.

3.1. The singles analysis

3.1.1. Angular distributions

Fission cross sections were extracted from the data by integration of the angular distributions of fission fragments. As shown in Figure 2.1, sixteen detectors were arranged in a plane around the target, at angles ranging from 15° to 160°. Thirteen of these detectors were used in the analysis; the two most forward detectors (at 15° and 20°) were unplugged during the experiment (the rates of scattered beam were causing almost continuous triggers in these detectors, leading to unreasonable dead times in the data acquisition system), and the detector at 45° failed

during the course of the experiment. The yield of fission fragments in each detector was determined by integrating the counts within a gate set on the energy spectrum. Fission fragments were easily separable in energy from scattered beam; a representative energy spectrum is shown in Figure 3.1. The differential cross section $\frac{d\sigma}{d\Omega}$ for each detector was calculated, where

$$d\sigma = \frac{N}{n\,\phi \cdot LT} \tag{3.1}$$

where N is the number of counts in the fission peak, n is the number of target atoms, ϕ is the beam flux, and LT is the live time of the data acquisition system; and $d\Omega$ is the detector solid angle in the center-of-mass (CM) frame.

For each energy, the in-plane angle θ (relative to the beam axis) was also transformed into the center-of-mass frame. Fission fragment velocities used in the CM transformations were calculated using the systematics of Viola, Kwiatkowski, and Walker [Vio85] for total kinetic energy of fission. By fitting to a large set of experimental data, Viola *et al.* describe the most probable total kinetic energy release in fission $\langle E_K \rangle$ as:

$$\langle E_K \rangle = (0.1189 \pm 0.0011)\,\frac{Z^2}{A^{1/3}} + 7.3\,(\pm 1.5)\ \text{MeV} \tag{3.2}$$

Symmetric fission was assumed, with the total kinetic energy divided equally between the fission fragments. (A mass split of 1.4:1 would introduce an uncertainty in the CM angles of up to 1.5° at the lowest energy and up to 3° at the highest energy.) Once the system was transformed to the center-of-mass frame, the differential cross sections $\frac{d\sigma}{d\Omega}$ were plotted as a function of θ to give the angular distributions.

Two methods were used to fit the angular distribution data. In the simplest approach, the data can be modeled by a curve with shape $\frac{1}{\sin\theta}$. In the center-of-mass frame, fission fragments are emitted isotropically (assuming a fully

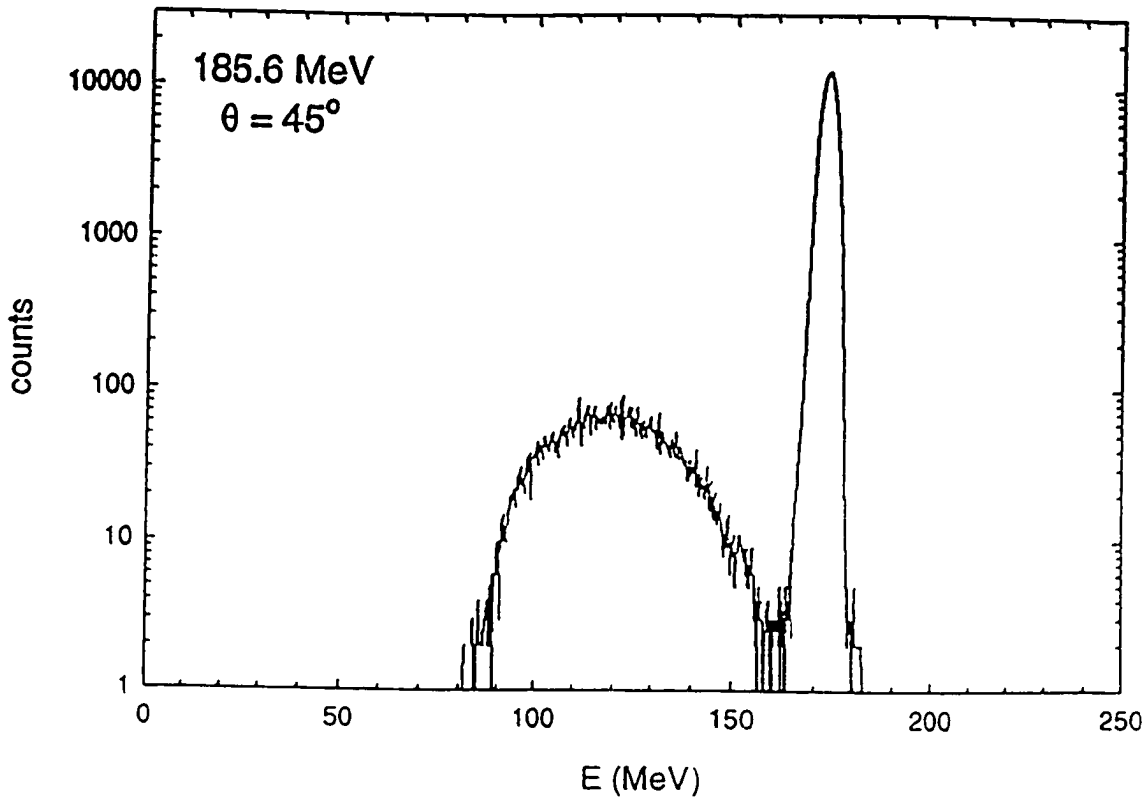

FIGURE 3.1. A representative energy spectrum showing the separation between fission fragments and scattered beam.

equilibrated compound nucleus); that is, $d\sigma$ is constant as a function of θ. Since $d\Omega$ is proportional to $\sin\theta\, d\theta$, then plotting $\frac{d\sigma}{d\Omega}$ as $f(\theta)$ should yield a curve which can be fitted by a function $\frac{x}{\sin\theta}$ where x is a constant. These fits to the data are shown in Figures 3.2 and 3.3. The function was truncated at 12° and 168° for numerical integration.

A more exact method to describe fission fragment angular distributions was taken from Vandenbosch and Huizenga [Van73] and was also used to fit the data. In this approach, the fissioning nucleus is described as an axially symmetric top. The system can be defined by the angular momentum, J; K, the projection of J on the nuclear symmetry axis; and M, the projection of J along the space-fixed axis (which is defined as the beam axis), as shown in Figure 3.4.

The probability of emitting fission fragments in a given state (J,K,M) at a given angle θ can be written as [Boh39]

$$W^J_{M,K}(\theta) = \frac{2J+1}{2}\left|d^J_{M,K}(\theta)\right|^2 \tag{3.3}$$

where the functions $d^J_{M,K}(\theta)$ are given by the symmetric top wavefunctions. If it is assumed that the projection M of the total angular momentum on the beam axis is small compared to J, then for a given J, the angular distribution of fission fragments is determined by K, the projection of J on the nuclear symmetry axis. The distribution of K values can be treated as a Gaussian function and K_0^2, the variance in the K distribution, is taken to be

$$K_0^2 = \frac{T\mathcal{J}_{\text{eff}}}{\hbar^2} \tag{3.4}$$

T is the thermodynamic temperature, and $\mathcal{J}_{\text{eff}}$ is the effective moment of inertia:

$$\frac{1}{\mathcal{J}_{\text{eff}}} = \frac{1}{\mathcal{J}_{\parallel}} - \frac{1}{\mathcal{J}_{\perp}} \tag{3.5}$$

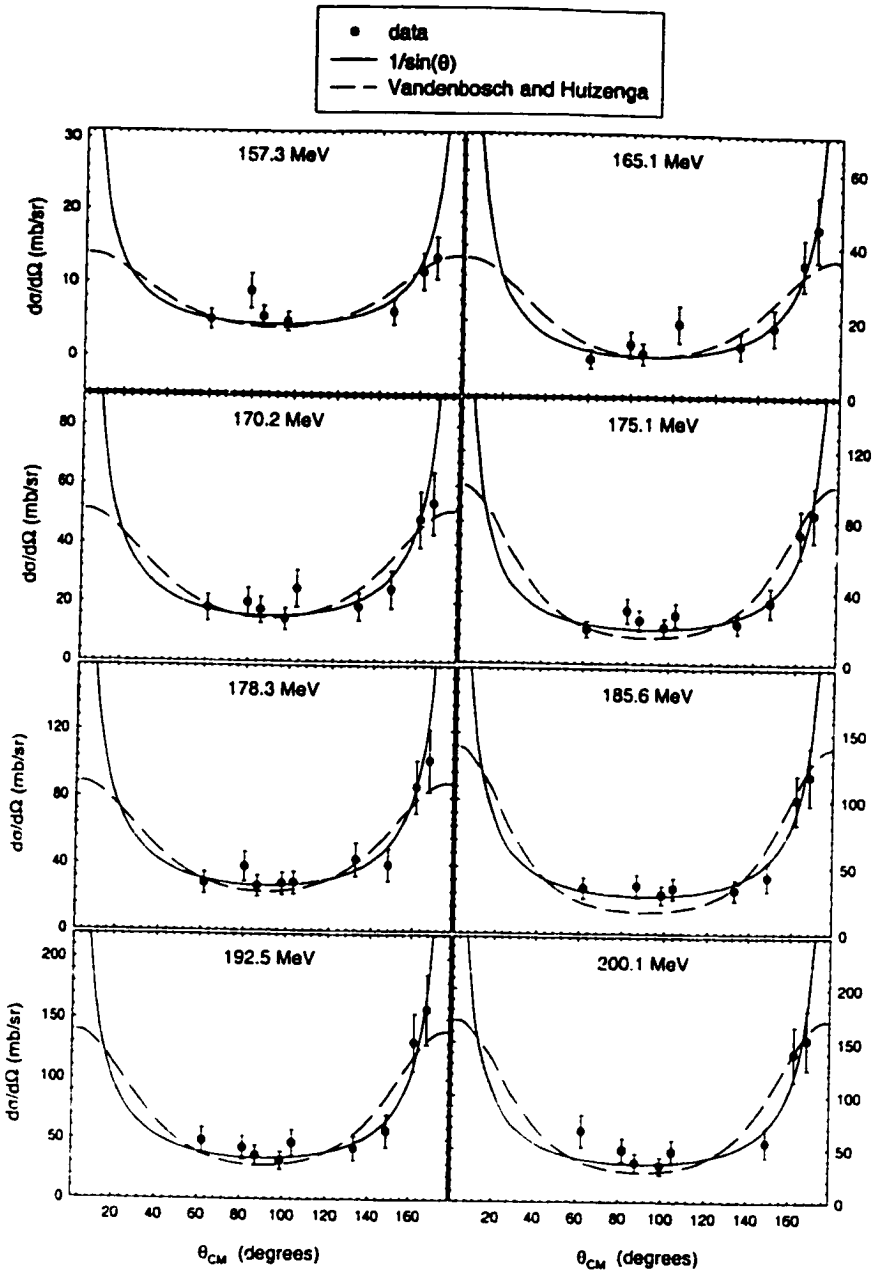

FIGURE 3.2. Fits to the angular distribution data, showing the two fitting methods. (Continued on following page.)

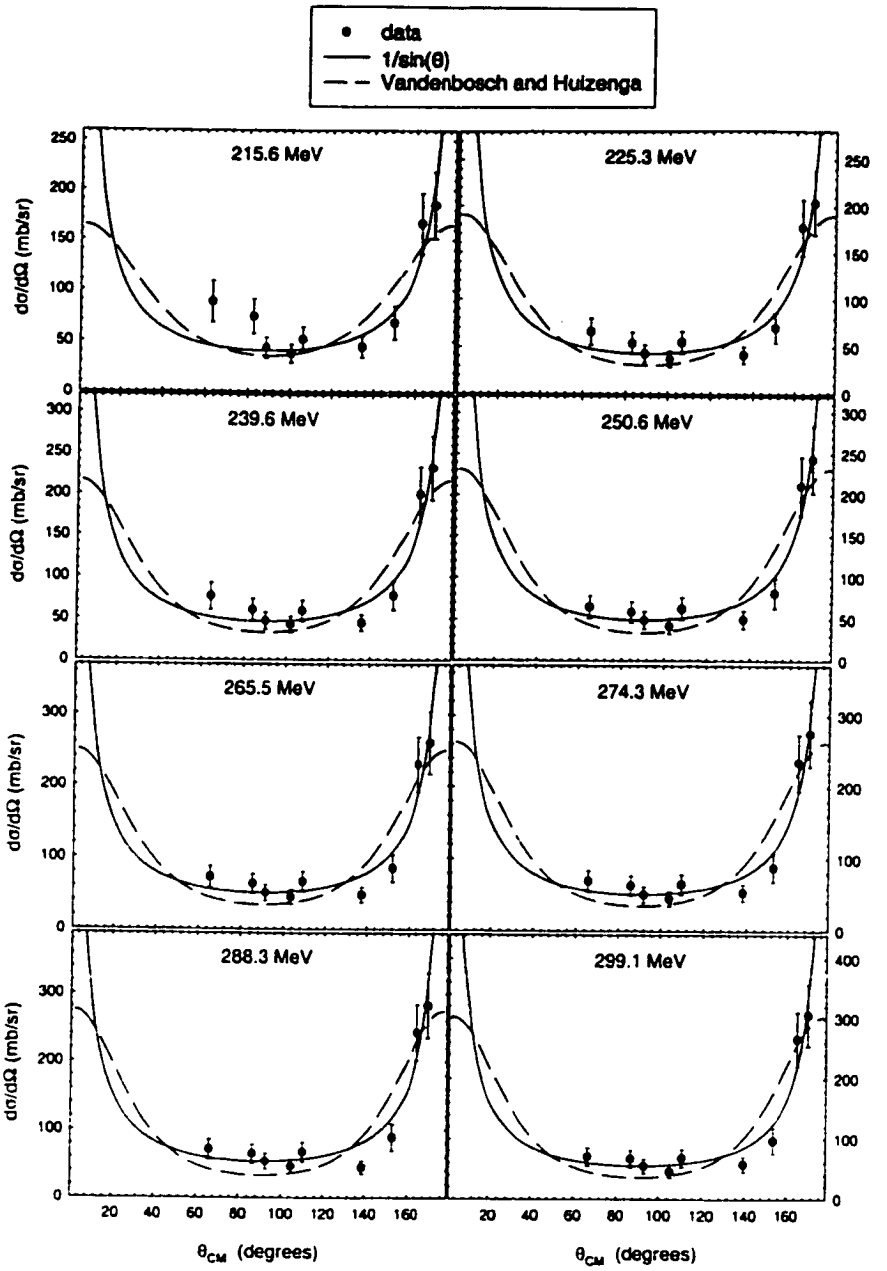

FIGURE 3.3. Fits to the angular distribution data, showing the two fitting methods. (Continued from previous page.)

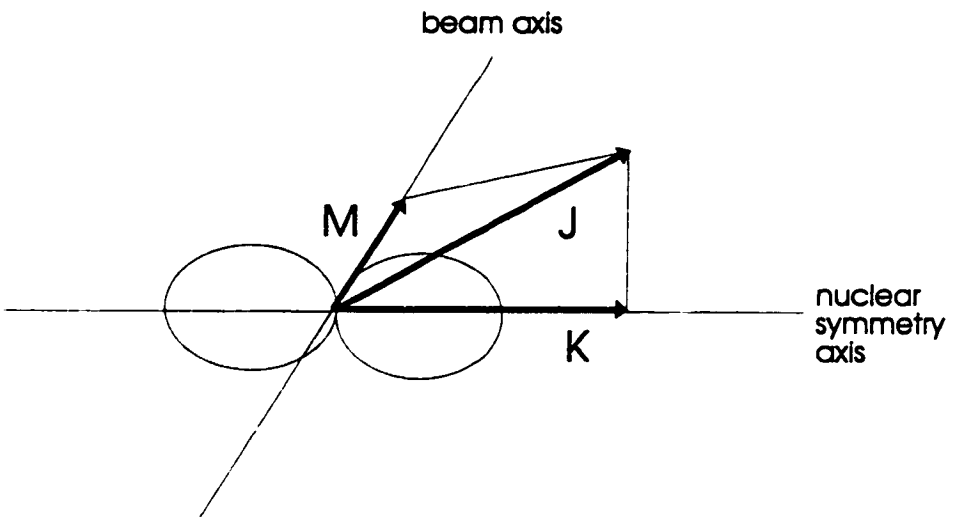

FIGURE 3.4. Schematic diagram of the vectors describing the fissioning system.

Using an approximate expression for the $d^J_{M,K}(\theta)$ functions, Vandenbosch and Huizenga give an analytic expression (developed by Huizenga, Behkami, and Moretto [Hui69]) for the angular distribution of fission fragments:

$$W(\theta) \propto \sum_{J=0}^{\infty} \frac{(2J+1)^2 T_J \exp\left[\frac{-\left(J+\frac{1}{2}\right)^2 \sin^2\theta}{4K_0^2}\right] J_0\left[\frac{i\left(J+\frac{1}{2}\right)^2 \sin^2\theta}{4K_0^2}\right]}{\operatorname{erf}\left[\frac{\left(J+\frac{1}{2}\right)}{(2K_0^2)^{1/2}}\right]} \quad (3.6)$$

J_0 is the zero-order Bessel function with an imaginary argument, and erf(x) is the error function. For the transmission coefficients T_J, the sharp cutoff approximation was used. The angular distribution data were fitted according to this prescription, using J_{max} values determined by the experimental cross sections, and allowing K_0^2 to vary to achieve the best fit to the data. These fits are also shown in Figures 3.2 and 3.3. When the angular distribution fits were integrated to yield total cross sections for the $^{32}S + {}^{181}Ta$ data, the two methods of fitting gave equivalent results; this can be seen in a plot of the unnormalized cross sections obtained from each fitting method, given in Figure 3.5.

3.1.2. Normalization procedure

The angular distributions of fission fragments, when integrated, resulted in absolute cross sections that were more than a factor of two less than any theoretical predictions. Given the experimental difficulties with the Faraday cup (described in Section 2.2.2), the values for absolute beam currents were suspect, and so the cross sections for elastically scattered beam in the most forward detectors were used as a measure of beam current to normalize the fission cross sections.

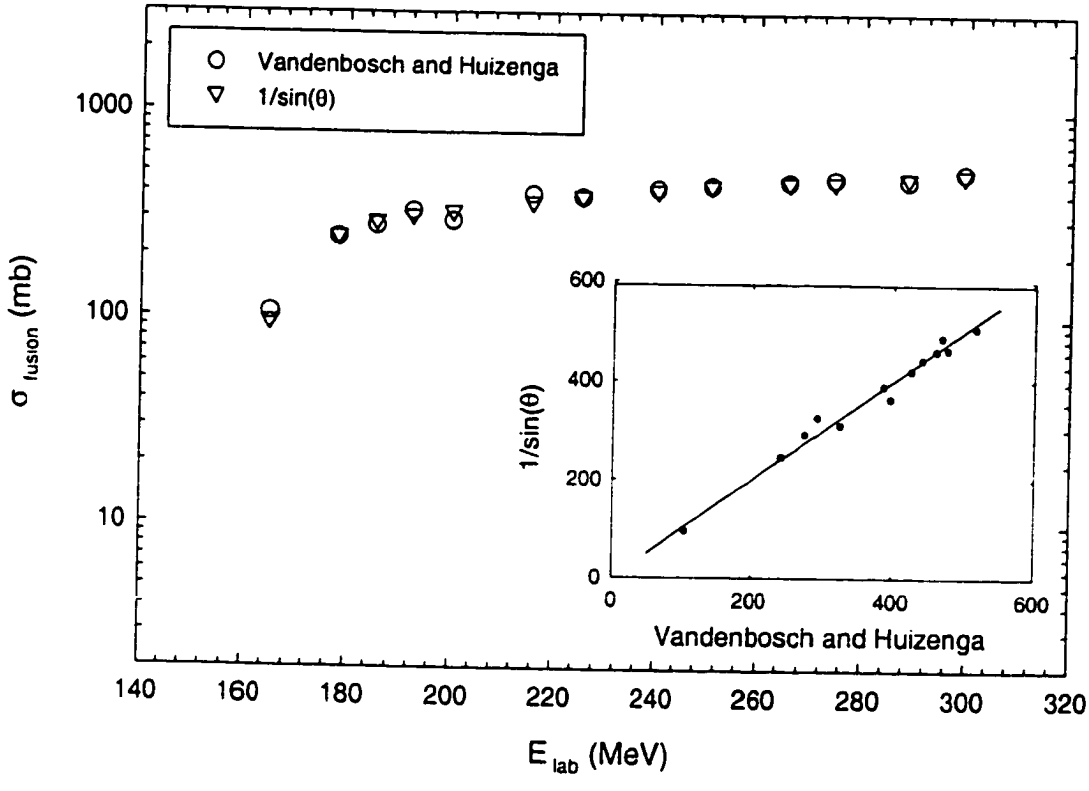

FIGURE 3.5. Comparison of cross sections obtained by the two methods used to fit the fission fragment angular distributions. The inset shows the values plotted against each other, with a guideline at 1:1 correspondence.

The differential cross section for pure Coulomb scattering is given by the Rutherford formula:

$$\frac{d\sigma_{Rutherford}}{d\Omega} = \left(\frac{d_0^2}{4}\right)\frac{1}{\sin^4\frac{\theta}{2}} = \left(\frac{Z_1 Z_2 e^2}{4E}\right)^2 \frac{1}{\sin^4\frac{\theta}{2}} \tag{3.7}$$

where d_0 is the distance of closest approach for a head-on collision, which is dictated by the projectile and target charges Z_1 and Z_2, and by the center-of-mass beam energy E. (The angle θ and solid angle $d\Omega$ are also in the CM frame.) For collisions with small impact parameters, i.e., near-head-on collisions in which the beam particle is scattered to backward angles, nuclear forces between the two nuclei come into play and so the cross sections for scattered beam cannot be described by the Rutherford cross section. However, at forward angles (corresponding to large impact parameters), the forces involved are pure Coulomb, and the elastic scattering cross section shows a 1:1 correspondence to the Rutherford cross section (see, e.g., [Bas80, Sat90]). The ratio of observed scattered beam in detectors inside the grazing angle to predicted Rutherford scattering cross sections, then, can be used as a normalization factor. The grazing angle θ_{gr}, which is the angle at which the collision impact parameter corresponds to the Coulomb radius of the system, is given by [Bas80]:

$$\sin\left(\frac{\theta_{gr}}{2}\right) = \frac{\varepsilon_c}{2\varepsilon - \varepsilon_c} \tag{3.8}$$

where ε is the laboratory energy per nucleon of the projectile, and ε_c is the reduced Coulomb barrier:

$$A_{12}\,\varepsilon_c = \frac{Z_1 Z_2 e^2}{R_c}, \qquad A_{12} = \frac{A_1 A_2}{A_1 + A_2} \tag{3.9}$$

The Coulomb radius R_c was taken to be

$$R_c = R_1 + R_2 + 3.5 \text{ fm}; \tag{3.10}$$

$$R_n = r_{0C}\, A_n^{1/3} \quad \text{with } r_{0C} = 1.44 \text{ fm}.$$

Detectors inside the grazing angle sample the portion of elastic scatter resulting from pure Coulomb interactions, and so elastic scattering cross sections for the most forward detectors were determined and used with the calculated Rutherford cross sections to normalize the beam current data. (The grazing angle for the highest measured energy for this system, 299.1 MeV, is 41°, and so even at the highest energies at least one detector was well inside the grazing angle.) The resulting normalized fission cross sections are given in Table 3.4, and the excitation function is shown in Figure 3.6.

Uncertainties listed for the fission cross sections are relative uncertainties. They were estimated by assuming that the fission yields followed a Gaussian distribution, and so the error in the count rate was taken to be the square root of the number of counts. The live time and current integrator count rate were assumed to be accurate to 1%. The uncertainty in the Rutherford normalization was determined by the differences in correction factors for several detectors in the same run and for different runs at the same beam energies; this was the largest contribution to the total uncertainty, and was of the order of 1.5-4%.

3.2. Comparison of singles data to fusion models

Once the absolute cross sections were extracted from the angular distribution data, the singles excitation function could be compared to various models for fusion. A simple classical approach was used to describe the data and to determine experimental values for the fusion barrier V_b and radius R_b; these were then compared with model predictions. The issue of near- and subbarrier fusion also had to be addressed: fusion for medium to heavy systems show significant deviations in the near- and subbarrier cross sections as compared to those predicted by classical

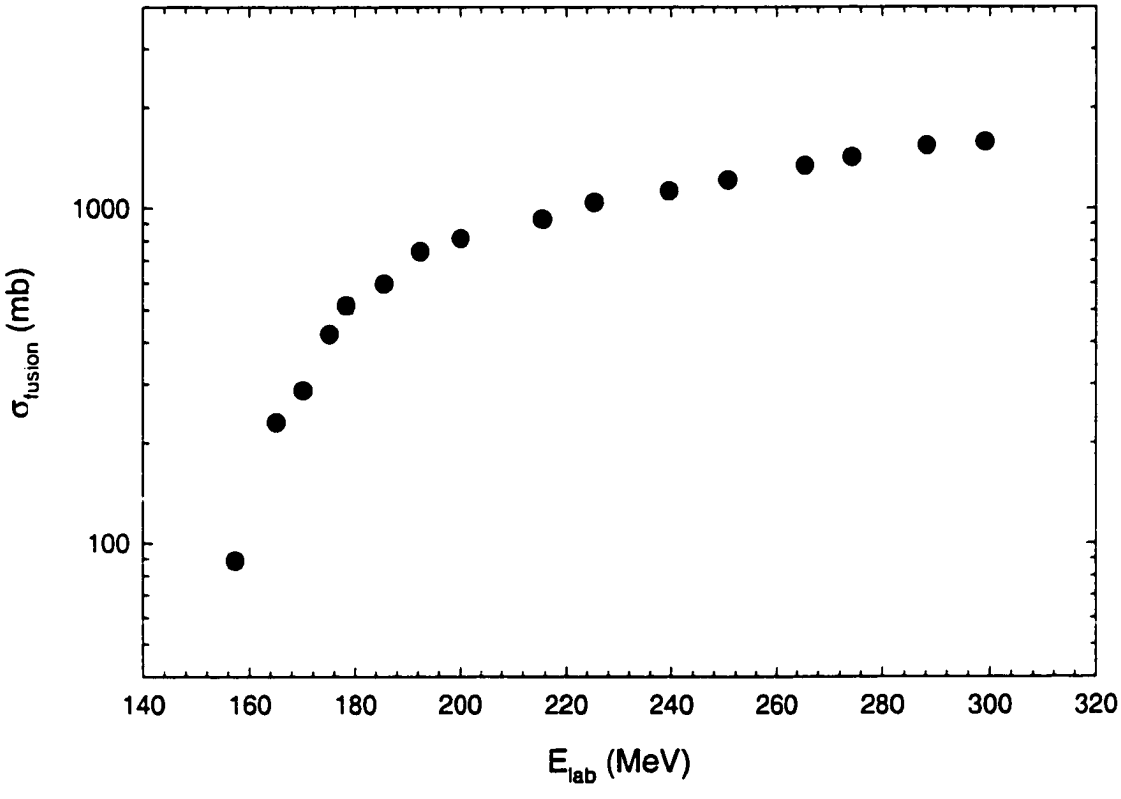

FIGURE 3.6. Excitation function for the ^{32}S + ^{181}Ta reaction derived from the fission singles data. Error is smaller than the size of the data points unless otherwise indicated.

models using a one-dimensional barrier (see, e.g., [Vaz81, Rei85]). To test this, the data were analyzed using a coupled-channels method which takes into account the effects of coupling to modes such as static deformations, dynamic excitations, and transfer reactions on the fusion cross section. In both of these analyses of the singles data, the assumption was made that passage of the barrier was necessary and sufficient condition for fusion; that is, the fate of the mononucleus between capture and fission was assumed to be formation of a fully equilibrated compound nucleus. This is not necessarily the case; however, the models used do not distinguish between mononucleus formation and true complete fusion, and so the issue will be treated separately in Section 3.4.

In this section, a brief description of some common models for fusion will be given, followed by a comparison of the singles data to the predictions of these models. The effects of a distribution of barriers on the cross section and the coupled-channels analysis will then be described; and the results of the classical and coupled-channels approaches will be compared. Finally, the same analysis methods will be applied to existing data for two similar systems, $^{34}S + {}^{168}Er$ and $^{32}S + {}^{182}W$, in order to test the method on high-precision data and to view the results for $^{32}S + {}^{181}Ta$ in the context of other, similar systems.

3.2.1. Models for fusion

3.2.1.1. The classical approach and barrier penetration [Bas80]

The fusion of two nuclei is governed by the effective nucleus–nucleus potential between them, which combines the attractive short-range nuclear force and the repulsive long-range Coulomb interaction. This effective potential typically has an energy minimum, or "pocket", at short range $r < R_b$ (where R_b is the barrier

radius) and a potential barrier of height V_b and curvature $\hbar\omega$ centered at R_b. In addition, the angular momentum of the compound system must be accounted for by a centrifugal term $\frac{\ell(\ell+1)\hbar^2}{2\mu r^2}$, which has the net effect of raising the pocket in the potential until at some critical angular momentum ℓ_{crit}, there is no longer a minimum in the nucleus-nucleus potential.

The most straightforward approach to determining the fusion cross section is to apply the classical formula

$$\sigma(E) = \pi R^2 \left[1 - \frac{V_b}{E}\right] \tag{3.11}$$

That is, the cross section increases from zero at the fusion barrier $E = V_b$ to a saturation value of πR^2 at $E \gg V_b$. At energies below the barrier, there is no possibility of fusion in the classical treatment; however, measurable fusion cross sections at subbarrier energies are a well-documented fact. Inclusion of quantum tunneling in a "one-dimensional barrier penetration" model improves the agreement between theory and experiment at subbarrier energies.

If the cross section is rewritten as a sum over all possible partial waves,

$$\sigma = \sum_J \sigma_J = \pi\lambda^2 \sum_{\ell=0}^{\infty} (2\ell+1)\, T_\ell \tag{3.12}$$

then the transmission coefficients T_ℓ can help define both the high-energy and low-energy limits of fusion. At high energies, a common assumption is the "sharp cutoff approximation", where

$$\begin{aligned} T_\ell &= 1 \quad \ell \leq \ell_{crit} \\ &= 0 \quad \ell > \ell_{crit} \end{aligned} \tag{3.13}$$

although in reality, a slightly less abrupt transition from $T_\ell = 1$ to $T_\ell = 0$ would be expected. For energies at and below the barrier, the Hill-Wheeler barrier penetra-

tion model [Hil53] can be used to define T_ℓ:

$$T_\ell = \left[1 + \exp\left(+2\pi \frac{V_\ell - E}{\hbar\omega_\ell}\right)\right]^{-1} \tag{3.14}$$

where V_ℓ is the effective barrier height for the partial wave with angular momentum ℓ. An elaboration of Equation 3.11 which includes penetrability was proposed by Wong [Won73] expressing the fusion cross section as

$$\sigma(E) = \frac{R^2}{2}\left(\frac{\hbar\omega_0}{E}\right) \times \ln\left\{1 + \exp\left[\frac{2\pi}{\hbar\omega_0}(E - V_b)\right]\right\} \tag{3.15}$$

The barrier penetration model includes quantum tunneling effects, resulting in nonzero transmission probabilities at energies below the barrier, and so is a good first-order approach to subbarrier fusion.

3.2.1.2. Nuclear potentials [Bas80, Ram87b, Fel84, Vaz81]

The fusion barrier can be parametrized by the barrier height V_b, its radius R_b, and the curvature $\hbar\omega$ of the top of the barrier potential. Any theoretical description of these quantities is dependent on the models chosen to describe the nucleus-nucleus potential. The Coulomb contribution is generally treated using the familiar formula $V_c = \frac{Z_1 Z_2 e^2}{R}$; however, there are several widely-used models for the attractive nuclear potential. Nuclei are too complex for exact solutions to the many-body Schrödinger equation to be feasible, yet they are not large enough to treat rigorously with statistical methods. This problem is compounded by the fact that the interaction between nucleons is not completely understood. Descriptions of the nuclear potential used in fusion models commonly treat the attraction between nucleons as an average effective potential and ignore the internal structure of the nucleus. In addition, several of the most popular potential models are semiempirical parametrizations which have evolved from fitting to experimental data. Sev-

eral models for nuclear potentials are commonly cited in the literature, including the Woods-Saxon potential [Woo54], the proximity potential [Ran74, Blo77], the Krappe-Nix-Sierk (KNS) potential [Kra79], the Akyüz-Winther potential [Aky79], and the energy-density formalism [Ngô75]. A broad comparison of many different excitation functions has been made in a review by Vaz, Alexander, and Satchler [Vaz81], in which it is shown that the deduced empirical fusion barriers vary only slightly with the model potential chosen. A more detailed discussion of the many commonly used nuclear potentials is beyond the scope of this work, and may be found in the references above.

3.2.1.3. Empirical models

One of the most well-accepted models for fusion is the semiempirical approach developed by Bass [Bas74, Bas77, Bas80]. In this method, it is assumed that the sizes and shapes of the colliding nuclei are frozen during barrier passage, and so mass transfer and dynamic deformations do not affect the system. Fusion occurs when the energy of relative motion is completely dissipated and the system is trapped in the attractive pocket of the effective potential. In essence, the Bass model assumes that the system's complex evolution in degrees of freedom such as shape and mass transfer happen on a longer timescale than barrier passage, and so do not affect the fusion barrier. (These degrees of freedom strongly affect the fate of the compound system after barrier penetration, but this is beyond the scope of the Bass model and will be discussed in Section 3.4.) The fusion cross section in the Bass model is based on the classical formula of Equation 3.11, and the nuclear potential is taken to be an empirical modification of the proximity potential developed by fitting to experimental data. The Bass model has shown great success in its predictive ability

for near- and above-barrier fusion cross sections, and has gained wide acceptance in the literature.

Although the Bass model is probably the most well-accepted parametrization of fusion excitation functions, several other empirical and semiempirical prescriptions have been proposed. A few of these will be compared to the data in Section 3.2.2, and so are briefly summarized here.

Vaz, Alexander, and Satchler [Vaz78, Vaz81] used the proximity potential with small empirical changes, and developed a systematization of s-wave fusion barriers and barrier radii. They describe the barrier height and radius in terms only of Z and A of the projectile and target. A comparison with experimental data from 87 excitation functions [Vaz81] shows reasonable agreement at energies near and above the barrier. At subbarrier energies, the model often underestimates the fusion cross sections for heavier systems; this is a problem common to one-dimensional barrier models, and will be discussed in Section 3.2.3.

Recently, Royer, Normand, and Druet [Roy98] have published fully analytic expressions for determining fusion and fission parameters. They model the colliding (or separating) nuclei as liquid drops which move through a "compact quasi-molecular shape"; that is, a shape evolution from two separate spheres through a one-body necked configuration with spherical ends, to the final spherical compound nucleus. Analytic polynomial expressions in terms only of A and Z of the projectile, target, and compound system were developed for the fusion barrier height and radius, and for symmetric and asymmetric fission barriers for β-stable nuclei. These equations were solved in this analysis using a FORTRAN code available upon request from the authors. A comparison of the results obtained using the expressions of Royer *et al.* with empirical values shows good agreement over a wide range of masses and asymmetries of the fusing systems.

In order to assist experimentalists in the prediction and characterization of heavy-ion reactions, Wilcke *et al.* [Wil80] have tabulated several reaction parameters for more than 400 systems in the range of 1 to 50 MeV/nucleon. Their fusion cross sections are calculated using the proximity potential and Equation 3.11. Values for the barrier radius are taken from a previously published analysis of 56 experimental data sets [Bir79].

3.2.2. Application of models to the ^{32}S + ^{181}Ta system

The experimental values of the fusion barrier and barrier radius were determined using the classical formula of Equation 3.11. If the cross section is modeled as $\sigma = \pi R^2(1 - \frac{V_b}{E})$, then a plot of the cross section data vs. $\frac{1}{E_{CM}}$ will have a linear form with the x-intercept at $\frac{1}{V_b}$, and the y-intercept at πR^2. In reality, however, nonlinearities can occur at near- and subbarrier energies due to tunneling effects and coupling to other reaction modes, and at high energies due to angular momentum limitations on the fusion process. In this analysis, only data in the range $200 \leq \sigma \leq 800$ mb were used in the linear fit, in order to exclude these nonlinear regions. A plot of the cross section data vs. $\frac{1}{E_{CM}}$ is shown in Figure 3.7; reduced χ^2 for this fit is 0.22. The barrier as determined by this fit is $V_b = 130.9 \pm 0.5$ MeV, and the barrier radius is $R_b = 10.4 \pm 0.3$ fm.

Fusion barriers and radii were also calculated for the ^{32}S + ^{181}Ta system using the methods of Bass, Vaz *et al.*, Royer *et al.*, and Wilcke *et al.*, as described in the previous section. Table 3.1 gives the experimental values and those of the various model predictions. It can be seen that all of the predicted values overestimate the experimental barrier and barrier radius, with the predictions of Bass and Royer coming closest to the deduced experimental values. The measured barrier in this

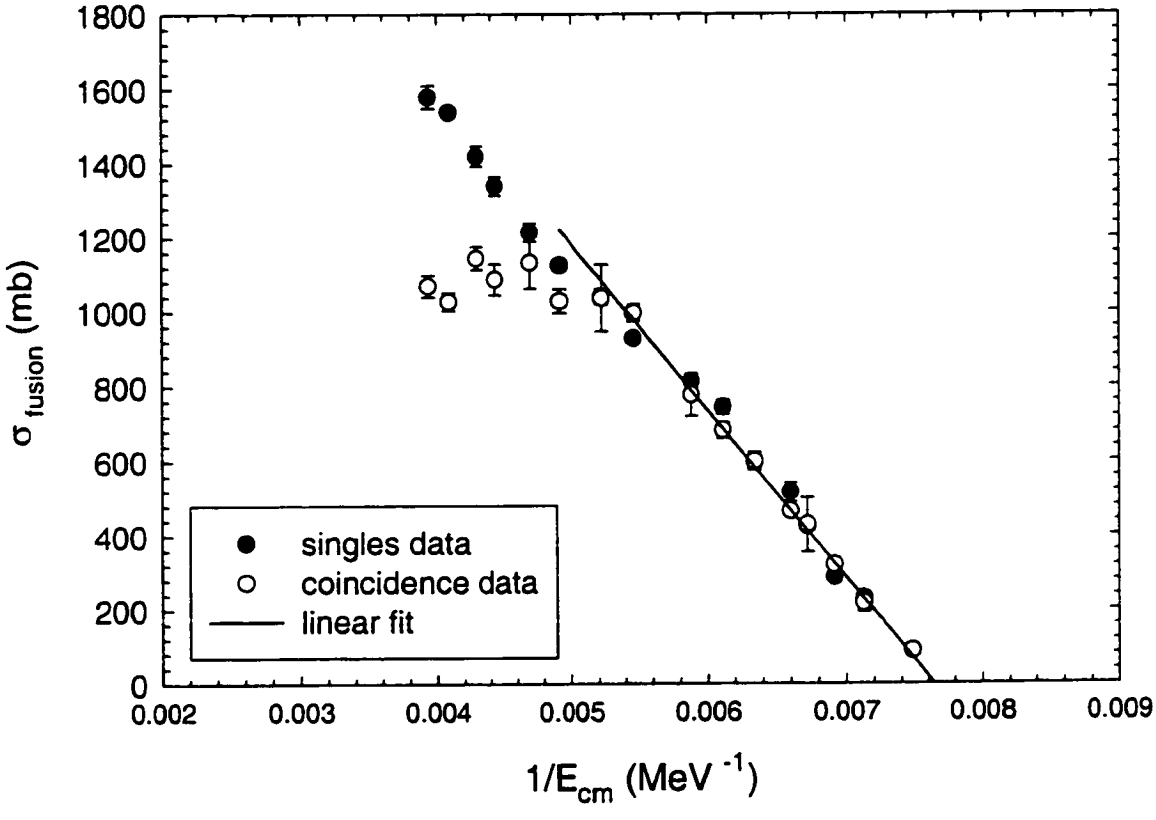

FIGURE 3.7. The linear fit to the cross section data vs. 1/E for the ^{32}S + ^{181}Ta system.

TABLE 3.1. Fusion barriers and barrier radii for the ^{32}S + ^{181}Ta system.

model	V_b (MeV)	R_b (fm)
experimental (1/E)	130.9 ± 0.5	10.4 ± 0.3
experimental (CCDEF)	129.5 ± 1.7	10.2 ± 0.4
mean	$\mathbf{130.7 \pm 0.3}$	$\mathbf{10.3 \pm 0.1}$
Bass [Bas80]	134.1	11.6
Vaz *et al.* [Vaz81]	138.0	11.4
Royer *et al.* [Roy98]	135.0	11.5
Wilcke *et al.* [Wil80]	137.9	11.4

case, however, is the interaction barrier, which in heavy systems is not necessarily identical to the barrier for true complete fusion. As the charge product Z_pZ_t increases, it becomes possible for the system to penetrate the interaction barrier and form a mononucleus, then fission before full equilibration. True complete fusion requires an additional "extra-push" energy beyond that required to penetrate the interaction barrier. This process, "quasifission", will be addressed in detail in Section 3.4. The models used for comparison here are based on complete fusion, and so the low value of the experimentally deduced barrier could be taken as a first-order indication of the presence of quasifission.

A secondary consideration is that all of the models above treat the collision partners as spherical. In reality, the Ta nucleus has a static prolate deformation ($\beta_2 = 0.269$, [Möl95]). In collisions with a deformed target, the barrier and barrier radius do not have a single value, but are dependent on the angle of orientation between the collision axis and the symmetry axis of the deformed nucleus. It has been shown [Sto78, Sto80, Rei82, Rei85] that in reactions with deformed nuclei, averaging over all orientations of the deformed nucleus yields an average value for

the barrier that is lower than that of the equivalent spherical system. In describing the fusion excitation function, then, factors beyond the masses and charges of the reaction partners must be taken into account. In this analysis, the effects of nuclear structure factors on the fusion cross section were addressed using a coupled-channels formalism.

3.2.3. Distributions of barriers

One common characteristic of all the fusion models mentioned above is that they tend to underestimate the cross section at subbarrier energies for heavier systems. Inclusion of tunneling effects as in the one-dimensional barrier penetration model is not sufficient to explain the enhancement. The failure of one-dimensional models at subbarrier energies has long been recognized (see, e.g., a review by Vaz, Alexander, and Satchler [Vaz81]), and much research has been devoted to exploring the mechanisms responsible. Better agreement between theory and experiment can be obtained if the concept of a single fusion barrier is replaced by a distribution of barriers due to effects of the nuclear structure of the colliding nuclei. However, the relative importance of the many possible degrees of freedom is still an open question; among the mechanisms explored have been static deformation, excitation of vibrational and rotational modes, coupling to nucleon transfer channels, and macroscopic ideas such as neutron flow and neck formation.

In experiments using $^{144-154}$Sm targets, Reisdorf *et al.* [Rei82, Rei85] and Stokstad *et al.* [Sto78, Sto80] have shown that the cross sections for reactions between spherical nuclei are equivalent when the bombarding energy is scaled by the Bass barrier for each system, while reactions with deformed targets do not fall into agreement, but show an enhancement of the low-energy cross section going

from spherical to deformed targets. This enhancement can be described [Sto78] by replacing the spherical radius R in calculations of the nuclear potential by an angle-dependent $R(\theta)$, where θ is the angle between the symmetry axis of the target nucleus and the beam axis.

In addition to static deformations, dynamic excitations of low-lying states in the projectile and/or target have been shown to affect the fusion cross section [Bec88]. Stelson *et al.* [Ste90] have measured excitation functions for ^{46,50}Ti + ^{90}Zr,^{93}Nb, and showed that the presence of low-lying collective states can enhance the subbarrier fusion cross section by an order of magnitude. However, vibrational excitations are insufficient to completely explain their data: the cross sections for the ^{46,50}Ti + ^{93}Nb reaction were factors of 3 to 6 larger than those of the ^{46,50}Ti + ^{90}Zr reaction, although ^{90}Zr and ^{93}Nb have similar quadrupole collective states. Stelson *et al.* attribute this to the difference in binding energies of the valence neutrons. The valence neutrons in ^{93}Nb are much more weakly bound than those of ^{90}Zr, and the barrier for neutron transfer disappears at about 1 fm greater distance for ^{93}Nb. They postulate that transfer or flow of neutrons may lead to formation of a neck between the colliding nuclei as a precursor to fusion. (Wu and Bertsch [Wu86] provide an alternate explanation for the differences in the ^{46,50}Ti + ^{90}Zr,^{93}Nb cross sections, in terms of coupling to several higher-order excitations in addition to the first 2^+ state.) Much attention has since been devoted in the literature to the importance of inelastic excitations as a microscopic approach, or neutron flow and neck formation as an alternative, macroscopic approach to describing subbarrier fusion (see, e.g., reviews by Reisdorf [Rei94] and Dasgupta *et al.* [Das98], and references therein).

Transfer of nucleons between the colliding nuclei (in a microscopic approach) has also been studied as a factor influencing subbarrier fusion. Beckerman *et al.* [Bec80, Bec81, Bec82] measured fusion cross sections for the systems ^{58,64}Ni +

^{58,64}Ni, and found that the excitation function for ^{58}Ni + ^{64}Ni did not resemble an interpolation between the ^{58}Ni + ^{58}Ni and ^{64}Ni + ^{64}Ni systems. At subbarrier energies, the mixed system ^{58}Ni + ^{64}Ni has higher cross sections than either of the symmetric systems, suggesting that neutron transfer to establish N/Z equilibrium strongly enhances subbarrier fusion. Consistent results were seen in an extension of this work to include the systems ^{58,64}Ni + ^{74}Ge and ^{74}Ge + ^{74}Ge [Bec83]. Stefanini *et al.* [Ste86] demonstrated that the effect can be generalized to mass-asymmetric systems, in measurements of ^{32,36}S + ^{58,64}Ni. When the neutron-poor target ^{58}Ni was used, the n-rich ^{36}S led to higher fusion cross sections at the lowest energies; however, in the case of the n-rich ^{64}Ni target, the n-poor projectile ^{32}S yielded the larger subbarrier cross sections. The relative N/Z ratios of projectile and target, and transfer of nucleons between them, clearly play a role in subbarrier fusion. (See the reviews and references cited above; also, e.g., [Mac96, Oer96, Ros97].)

Inclusion of coupling to deformations, dynamic excitations, and nucleon transfer requires replacing the single, one-dimensional potential barrier V_b with a distribution of barriers with varying heights and widths depending on the entrance channel of the colliding nuclei. This can be modeled using a coupled-channels approach, and it has been shown [Row91] that, with high-precision data, this distribution of barriers can be directly extracted from experimental data. These techniques have been used extensively in recent literature to determine the presence and strength of coupling to additional reaction channels from high-precision subbarrier fusion data ([Das98], and references therein).

3.2.4. The coupled-channels approach

The coupled-channels formalism is widely used to model the effect of coupling to additional reaction modes on the gross fusion excitation function and distribution of barriers. Reviews by Reisdorf [Rei94], Balantekin and Takigawa [Bal98], and Dasgupta [Das98], among others, contain detailed descriptions of the coupled-channels problem and methods of solution. The description herein will follow the approximations of Dasso *et al.* [Das83, Bro83b, Lan84], which were used to model the data with the codes CCFUS [Das87] and CCDEF [Fer89].

In the fusion of two nuclei, quantum tunneling under a multidimensional barrier can be described by a set of coupled equations in terms of the relative motion wavefunctions. Dasso *et al.* assume that the coupling interaction can be factored into relative and intrinsic motion parts, and make the further simplification of taking the relative motion form factor to be a constant, equal to the coupling strength at the s-wave barrier. (The fusion cross section is dependent on the flux passing through the barrier, and so only the coupling strength in the barrier region is taken to be essential.) This is typically referred to as the "constant coupling" approximation. The coupled equations decouple under these approximations, and the single barrier $V(r)$ has been replaced by a set of eigenbarriers $V(r) + \lambda_n$, which corresponds to the physical concept of a distribution of barriers described in the previous section. The transmission coefficients and fusion cross section can then be calculated using this set of eigenbarriers. The transmission coefficients are taken by Dasso *et al.* to have the Hill-Wheeler form, and the fusion cross section is calculated in CCFUS and CCDEF using a modification of Equation 3.15. In the codes CCFUS and CCDEF, the coupling of each mode is treated as a separate two-channel problem. CCFUS assumes that both reaction partners are spherical, but CCDEF allows for axially

symmetric deformations; the fusion cross sections are determined by averaging over all orientations of the deformed system. This approach treats the deformation within the sudden approximation [Won73]: since the timescale for barrier passage is short compared to that of rotational motion, the two nuclei are treated as frozen during the collision. Averaging over all orientations, therefore, is equivalent to coupling to the ground state rotational band.

Although simplified coupled-channels codes provide a good qualitative model, it has been noted [Bal98] that the constant coupling approximation can result in overestimates of the transmission functions as compared to exact coupled-channels calculations; this must be considered in any quantitative description of the data. In an analysis of fusion data for the ^{64}Ni + ^{92,96}Zr system, however, Stefanini [Ste92] compared results of the code CCFUS to exact coupled-channels calculations and found no significant difference. Another potential shortcoming of the simplified coupled-channels codes is that only single-phonon excitations are considered; it has been shown [Das97, Kru93, Ste95] that in some cases multiphonon states can couple strongly and play a significant role at subbarrier energies. This enhancement, however, is most evident in a low-energy, subbarrier region of the excitation function ($\sigma \simeq 10 - 50$ mb, [Kru93, Ste95]) which is not relevant to this data analysis. Although the limitations of coupled-channels codes must be kept in mind, they have come into common use in analysis of fusion data and in many cases can reproduce the measured excitation functions and distributions of barriers quite well [Ste92, Hin95, Cha95, Agu95, Liu96, Bie96].

3.2.5. *Coupled-channels analysis of the ^{32}S + ^{181}Ta data*

A coupled-channels fit to the ^{32}S + ^{181}Ta excitation function was made using the code CCDEF. The parameters used in the fit were the ^{181}Ta static deformation, with $\beta_2 = 0.269$ and $\beta_4 = -0.090$ [Möl95]; and the first 2^+ and 3^- excited states of the ^{32}S projectile ($\beta_2 = 0.336$, at 2.302 MeV [Ram87]; $\beta_3 = 0.48$, at 5.006 MeV [Spe89]). The barrier height and radius were allowed to vary to achieve the best fit to the experimental data. The resulting fit is shown in Figure 3.8.

The barrier parameters which gave the best fit to the experimental data were $V_b = 129.5 \pm 1.7$ MeV, $R_b = 10.2 \pm 0.4$ fm, and $\hbar\omega = 3.99$ MeV. These are listed in Table 3.1 with the results of the 1/E fit; it can be seen that the coupled-channels and classical fits yield the same results within error. (Error in the barrier height and radius for all coupled-channels fits was determined using a nonlinear least-squares fit to the data. Error bars were not assigned to the quantity $\hbar\omega$; since the lowest measured data point was at 133.7 MeV, i.e., still above the barrier, the curvature could be varied greatly with no significant effect on the excitation function in the region of the data.)

The best fit to the data, given by the solid line in Figure 3.8, is obtained from coupling to the target static deformation only. Reduced χ^2 for this fit is 1.95. Addition of coupling to the ^{32}S vibrational excitations results in a slight overprediction of the cross section at the lowest energies. However, in other published fits with coupled-channels calculations [Ste92, Agu95, Bie96], enhancements in the cross section due to vibrational couplings seem to be significant only in the region $\sigma \simeq 100$ mb and below. Since the only significant deviation between the data and the fit which includes the ^{32}S excited states is at the lowest-energy data point, the results of this fit are inconclusive. Additional data at subbarrier energies would

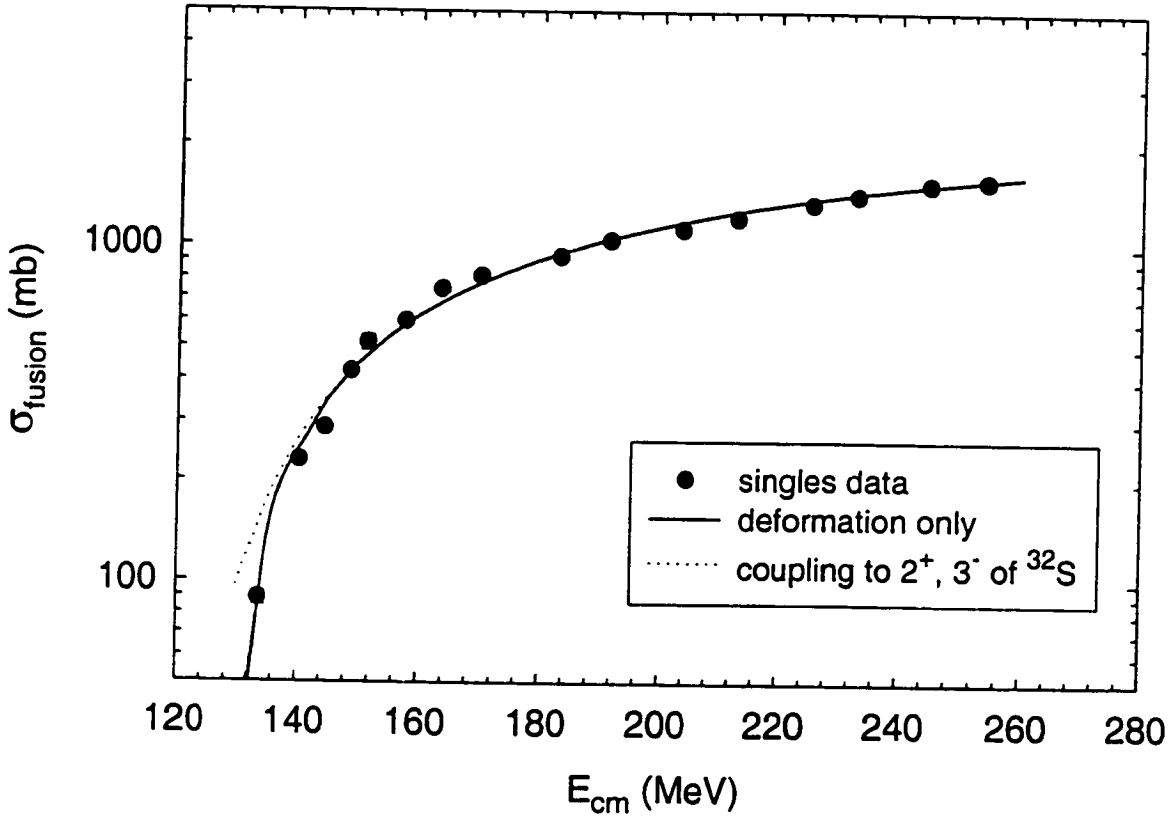

FIGURE 3.8. Coupled-channels fit to the ^{32}S + ^{181}Ta excitation function.

be necessary in order to draw any strong conclusions on the presence or absence of coupling to the vibrational states of the projectile.

3.2.6. Comparison to similar systems

In order to test the analysis methods and to place the ^{32}S + ^{181}Ta results within the context of similar systems, the same analysis was performed on fusion data for the reactions ^{34}S + ^{168}Er and ^{32}S + ^{182}W, which bracket the ^{32}S + ^{181}Ta system.

3.2.6.1. The ^{34}S + ^{168}Er system

High-precision subbarrier data for fusion of ^{34}S + ^{168}Er [Mor98] was used to test the coupled-channels method. The cross section was measured in 1 MeV steps down to the 1 mb range with very small error, and so leaves much less room for ambiguity in fitting than the ^{32}S + ^{181}Ta data. A coupled-channels fit with CCDEF was performed, including the ^{168}Er deformation ($\beta_2 = 0.294$, $\beta_4 = -0.007$, [Möl95]) and exploring couplings to the first 2^+ and 3^- vibrational states of the projectile and/or target. The parameters used for the ^{34}S excited states were $\beta_2 = 0.252$ at $E = 2.127$ MeV, $\beta_3 = 0.008$ at $E = 4.623$ MeV; and for ^{164}Er, $\beta_2 = 0.338$ at $E = 0.0798$ MeV, and $\beta_3 = 0.044$ at $E = 1.431$ MeV [Ram87, Spe89]. The barrier height and radius were allowed to vary as before to obtain the best fit to the data. The results of this fit were $V_b = 124.2 \pm 0.6$ MeV, $R_b = 11.3 \pm 0.9$ MeV, and $\hbar\omega = 3.21$ MeV; the fit is shown in Figure 3.9. For this system, it can be seen that coupling to static deformation of the ^{168}Er target alone is insufficient to describe the data. The best fit (with reduced $\chi^2 = 2.18$) includes coupling to the first 2^+ and 3^- states of ^{168}Er, as well as the static deformation; these states

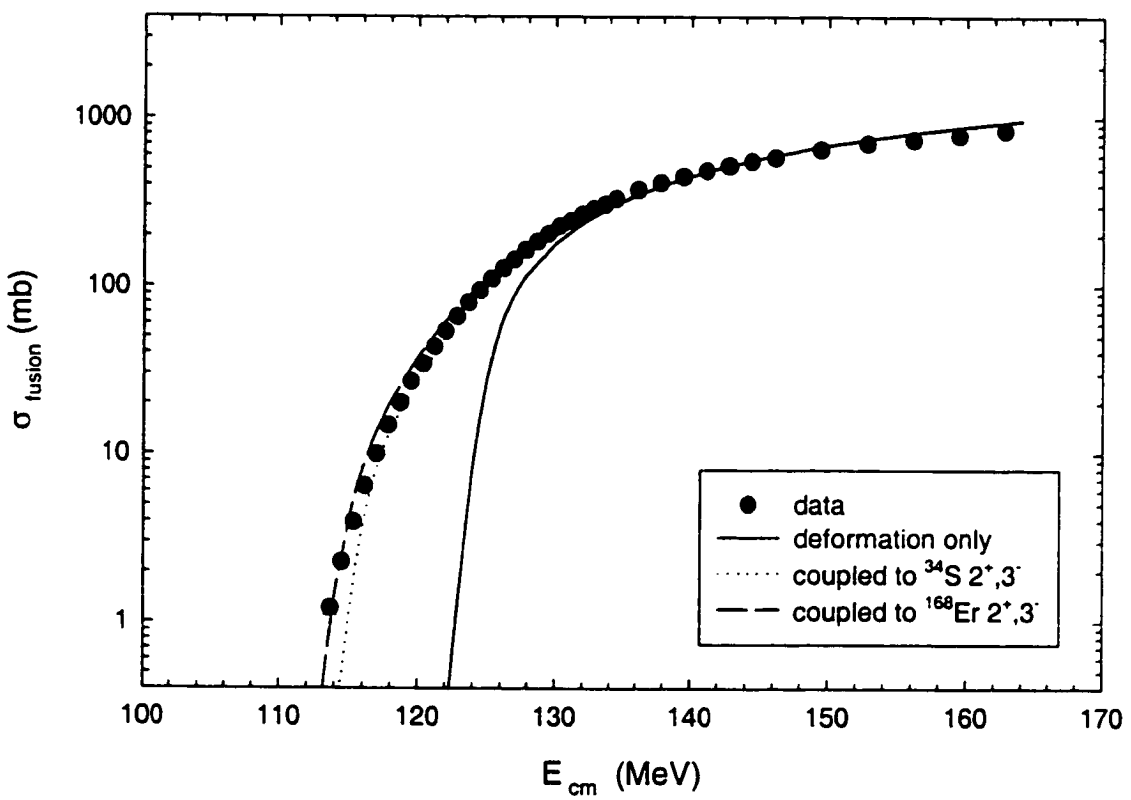

FIGURE 3.9. Coupled-channels fits to the ^{34}S + ^{168}Er excitation function. Error in the data is less than or equal to the size of the data points unless otherwise indicated.

TABLE 3.2. Fusion barriers and barrier radii for the ^{34}S + ^{168}Er system.

model	V_b (MeV)	R_b (fm)
experimental (CCDEF)	124.2 ± 0.6	11.3 ± 0.9
Bass [Bas80]	124.6	11.2
Vaz *et al.* [Vaz81]	128.8	11.4
Royer *et al.* [Roy98]	126.2	11.5

are very low-lying and can be seen to have a strong effect especially at subbarrier energies. An alternative fit, coupling to the first 2^+ and 3^- excited states of the ^{34}S projectile as well as the target deformation, describes the excitation function well into the subbarrier region, but begins to underrepresent the data at the lowest energies, in the region of $\sigma \leq 10$ mb.

Predictions for the s-wave barrier V_b and barrier radius R_b for ^{34}S + ^{168}Er were calculated using the various fusion models in the same manner as for the ^{32}S + ^{181}Ta system. These are listed in Table 3.2. As with the ^{32}S + ^{181}Ta system, the Bass barrier is the best match to the experimental value, with the parameters of Royer *et al.* also providing a reasonable description. The model of Vaz *et al.* slightly overestimates the barrier, as it did for the ^{32}S + ^{181}Ta system.

3.2.6.2. The ^{32}S + ^{182}W system

The same analysis methods were also applied to previously published data for the ^{32}S + ^{182}W reaction [Kel87]. Since this system differs from ^{32}S + ^{181}Ta by only a single proton in the target, any large variations in the analysis results would be an indication of problems in the data or analysis methods.

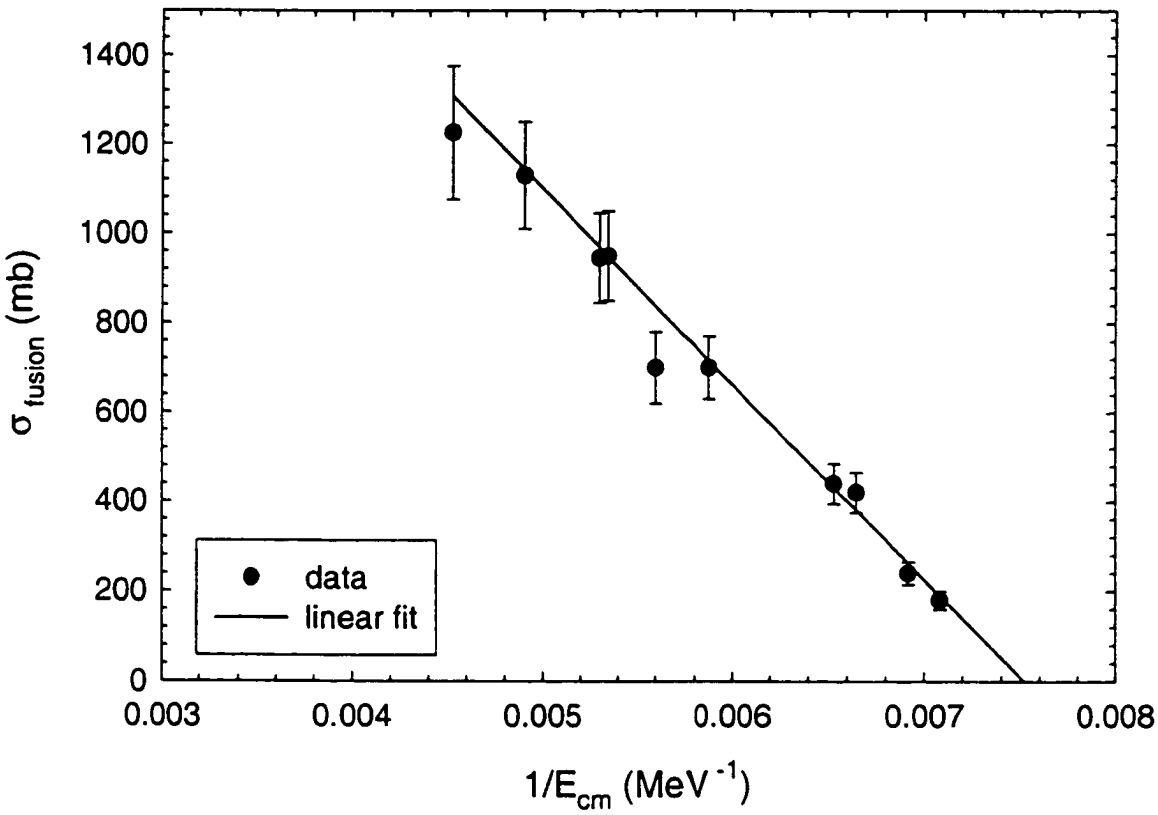

FIGURE 3.10. 1/E fit to the ^{32}S + ^{182}W fusion data.

The barrier height and radius were first extracted using the classical method of linear fitting to $1/E_{CM}$. The fit was made to data in the range 175 mb $\leq \sigma \leq$ 750 mb, and is shown in Figure 3.10. The resulting barrier parameters were $V_b = 133.0 \pm 1.2$ MeV and $R_b = 10.2 \pm 0.4$ fm, with reduced $\chi^2 = 0.58$. A coupled-channels fit using CCDEF was also made, using $\beta_2 = 0.259$, $\beta_4 = -0.084$ [Möl95] for the ^{182}W static deformation. Coupling to the lowest vibrational states of the ^{32}S projectile was also tested, using the same parameters given for the ^{32}S + ^{181}Ta

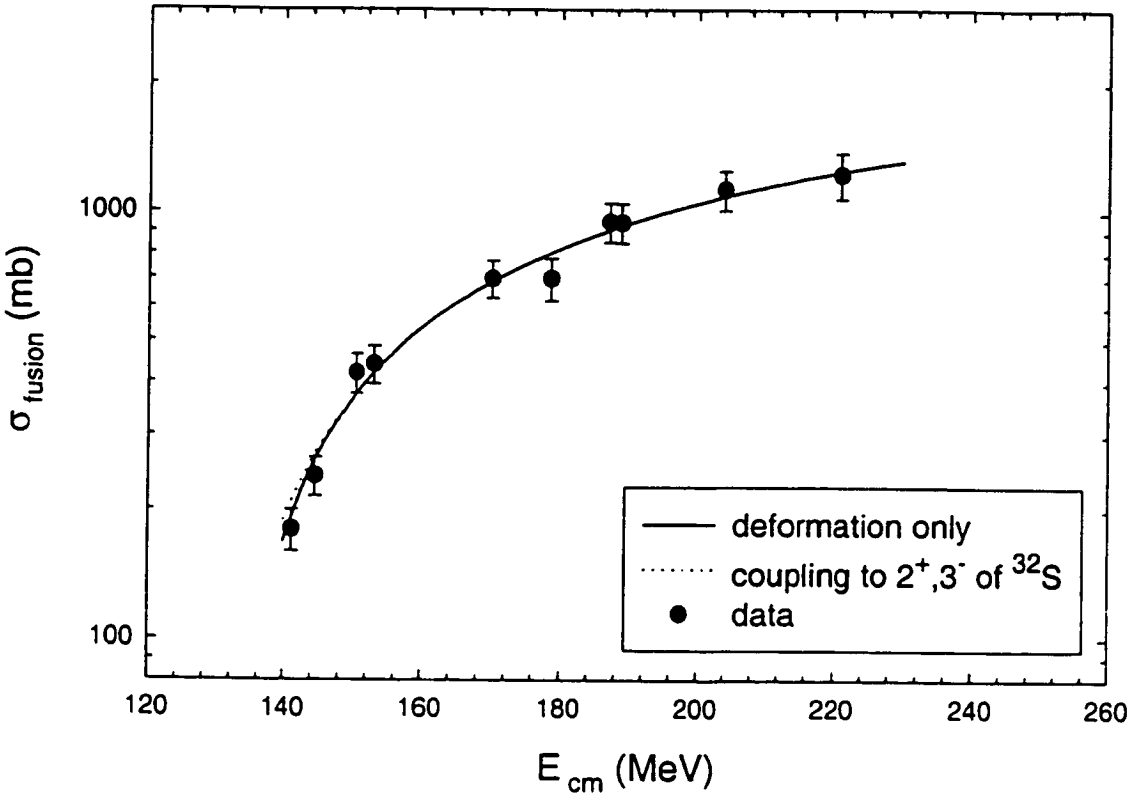

FIGURE 3.11. Coupled-channels fit to the ^{32}S + ^{182}W fusion data.

fits. The CCDEF fits are given in Figure 3.11; it can be seen that, as with the ^{32}S + ^{181}Ta system, the best fit to the data includes only the target static deformation. (Reduced χ^2 for this fit was 0.80.) In this case, however, there is very little difference between the fit using deformation only and that including the first 2^+ and 3^- vibrational states of ^{32}S, most probably because the data only extend down to 180 mb, which is above the region where the effects of these couplings should become evident. The parameters which provided the best fit to the data for the coupled-

TABLE 3.3. Fusion barriers and barrier radii for the ^{32}S + ^{182}W system.

model	V_b (MeV)	R_b (fm)
experimental (1/E)	133.0 ± 1.2	10.2 ± 0.4
experimental (CCDEF)	132.4 ± 3.4	9.9 ± 1.2
mean	$\mathbf{132.9 \pm 0.2}$	$\mathbf{10.1 \pm 0.1}$
Bass [Bas80]	135.3	11.3
Vaz *et al.* [Vaz81]	139.9	11.4
Royer *et al.* [Roy98]	136.8	11.5

channels fit were $V_b = 132.4 \pm 3.4$ MeV, $R_b = 9.9 \pm 1.2$ fm, and $\hbar\omega = 3.8$ MeV. These are listed in Table 3.3 along with various model predictions for the ^{32}S + ^{182}W system. The results of the analysis for the ^{32}S + ^{182}W system are very similar to those for ^{32}S + ^{181}Ta. Again, the values for barrier height and radius obtained from the classical and coupled-channels methods are in agreement, and again, the experimental values are lower than the model predictions. The Bass model provides the closest match to the experimental values, although again, the values of Royer *et al.* are also close. The predictions of Vaz *et al.* are slightly high. In the analysis of this published data, the authors made quantitative estimates of the quasifission component to the fission cross section, and found that it contributed a significant fraction; which agrees with the observation here that the interaction barrier is lower than the predicted barriers for true fusion. Comparing the experimental barrier heights and radii for the ^{32}S + ^{181}Ta and ^{32}S + ^{182}W data, it can be seen that the radii for the two systems are the same within error, as would be expected (10.3 ± 0.1 fm for the ^{181}Ta target, 10.1 ± 0.1 fm for ^{182}W). The barrier height for the ^{32}S + ^{182}W system (132.9 ± 0.2 MeV) is slightly higher than for the ^{32}S + ^{181}Ta system (130.7 ± 0.3 MeV), which is consistent with addition of a proton to the target.

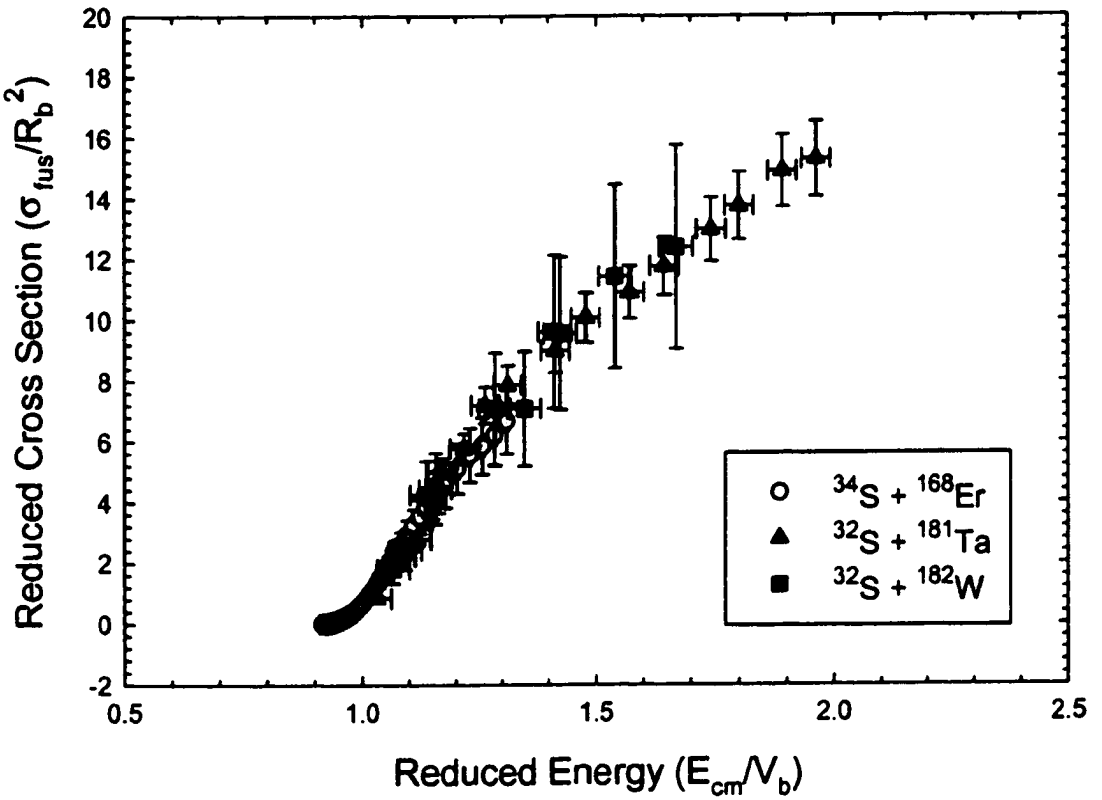

FIGURE 3.12. Reduced excitation functions for the three systems.

Figure 3.12 shows a plot of the reduced excitation functions for the three systems $^{32}S + ^{181}Ta$, ^{182}W, and $^{34}S + ^{168}Er$. By plotting σ_{fus}/R_b^2 against E_{CM}/V_b, the inherent differences between the three systems due to Coulomb and size effects are removed. Variations between the excitation functions which persist in this reduced plot indicate either differences in the reaction mechanism or problems in the data or fitting method. It can be seen in Figure 3.12 that when Coulomb and size differences are removed, the excitation functions for the three systems analyzed

here are in good agreement. The data for the $^{32}S + ^{181}Ta$ reaction are consistent with previous measurements for other, similar systems.

In summary, the singles angular distributions for the $^{32}S + ^{181}Ta$ reaction were integrated and normalized to the Rutherford cross sections. The resulting excitation function was analyzed using both a classical and a coupled-channels approach to extract the barrier parameters; the results of the two fitting methods were in agreement, and were consistent with data for other, similar systems.

3.3. The coincidence analysis

One of the necessary conditions of a complete fusion event is that there be full linear momentum transfer from the projectile to the compound system. Although an analysis of the fission excitation function, as in the singles data analysis, yields valuable information about the fusing system, there is a possibility that some fraction of these events are the result of deep-inelastic collisions, incomplete fusion, or other reactions. In order to separate these events from the fusion cross section, a reanalysis was made of the $^{32}S + ^{181}Ta$ data using coincident fission fragments to gate on full momentum transfer events.

3.3.1. Coincidence analysis methods

Since no time-of-flight information was available for the fission fragments, an iterative procedure was used to extract masses, momenta, and fission kinetic energies. Initially, symmetric fission was assumed, and using $m = \frac{A_{CN}}{2}$, fission fragment momenta in the lab frame were calculated from the detector angles and corrected energies of a coincidence event. (The same energy cuts on the fission fragment distributions were used as in the singles analysis.) The deposited energy

in the detectors was calibrated for pulse height defect [Sch66, Wei86]; corrections were also made for energy losses in the gold layer on the detector surface and in the Si dead layer. Energy loss in the target was calculated using the target half-thickness. The magnitude of these energy-loss corrections was 3-6 MeV for the target, and 0.7-1 MeV in the detector; this corresponds to a shift of 2-3% of full momentum transfer.

The laboratory momenta of the fission fragments were added to the compound nucleus momentum (determined by the beam energy) to give the momenta of the fragments in the frame of the fissioning system. From this, the kinetic energy of each fragment in the frame of the fissioning system was calculated, and new values for the mass of each fragment were obtained by assuming that the fragment momenta were equal and opposite in the frame of the fissioning system:

$$m_1 = A_{CN}\left(\frac{E_2}{E_1 + E_2}\right);\ m_2 = A_{CN}\left(\frac{E_1}{E_1 + E_2}\right) \tag{3.16}$$

The new fragment masses were compared to the previous values; if the difference was greater than 0.1 amu, another iteration was started. When the mass values had converged, the component of the laboratory momentum parallel to the beam direction was compared to the compound nucleus momentum to determine the linear momentum transfer for the event.

The total fusion cross section for the coincidence data was extracted by selecting events within $\pm 10\%$ of full linear momentum transfer and integrating the counts for each detector pair. The counts were then corrected for beam current, computer dead time, and target thickness, and normalized to the elastic scattering cross sections in the same manner as the singles data. Corrections were also made to compensate for the fact that the angles of the detector pairs did not always

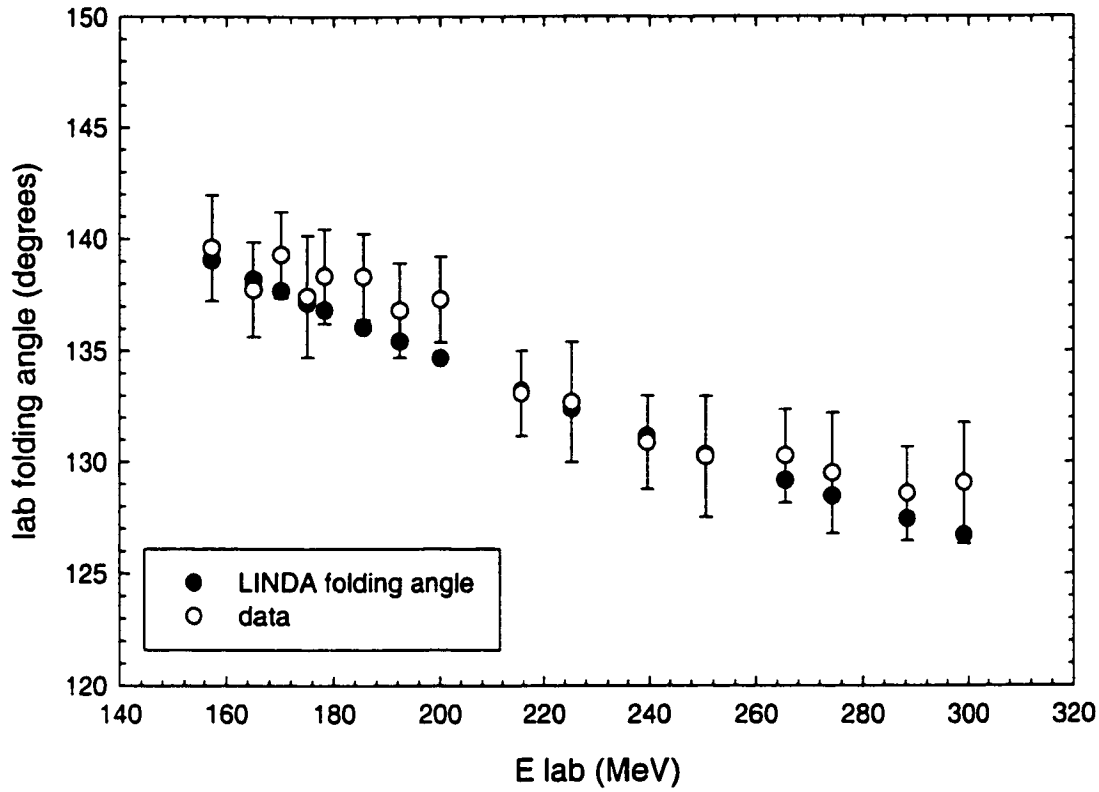

FIGURE 3.13. Comparison of observed laboratory folding angles with predictions of the code LINDA.

correspond to the optimum folding angle, and for efficiency loss in the "sweeper" detector due to rocking of the folding angle from neutron emission by the fission fragments. The statistical code LINDA [Due85] was used to model the folding angle distributions for a given trigger-sweeper detector pair. Figure 3.13 shows a comparison of predicted and observed folding angles; it can be seen that the LINDA predictions provide a reasonable description of the data. In the simulation, the trigger detector was set to the same angle and dimensions as those of the actual

experiment, and the sweeper detector was allowed to cover 180° on the other side of the beam in order to observe the width of the fission fragment distribution. The Gaussian distributions in (θ, ϕ) of the sweeper fragments given by LINDA were then used in a Monte Carlo simulation which calculated the fraction of events seen by a sweeper detector set off-center from the folding angle. In calculating the total cross section, detector pairs in which this "rocking efficiency" was less than 10% were considered to be too far from the optimum folding angle to be reliable, and so were not used. Data from each of the detector pairs were weighted according to relative count rates in the angular distributions for each trigger angle when averaging to obtain the coincidence cross sections.

The resulting coincidence excitation function is shown in Figure 3.14, and the cross sections are given in Table 3.4. Uncertainties in the cross sections were estimated in the same manner as for the singles data, but also including the uncertainty resulting from the effect on the rocking efficiency correction of a $\pm 1°$ error in the folding angle. The coincidence data are in very good agreement with the singles data at energies below 240 MeV; however, above this , the coincidence cross sections begin to decrease slightly while the singles excitation function continues to rise. It is apparent that, at higher energies, there is an additional reaction contributing to the total fission cross section.

3.3.2. The incomplete momentum transfer component

Analysis of the momentum distributions of the fission fragments shows a single peak centered at full linear momentum transfer (FLMT), corresponding to complete fusion, to be the only observable reaction for the measured energies between 157 MeV and 225 MeV (lab). At 239 MeV and above, however, a "shoulder"

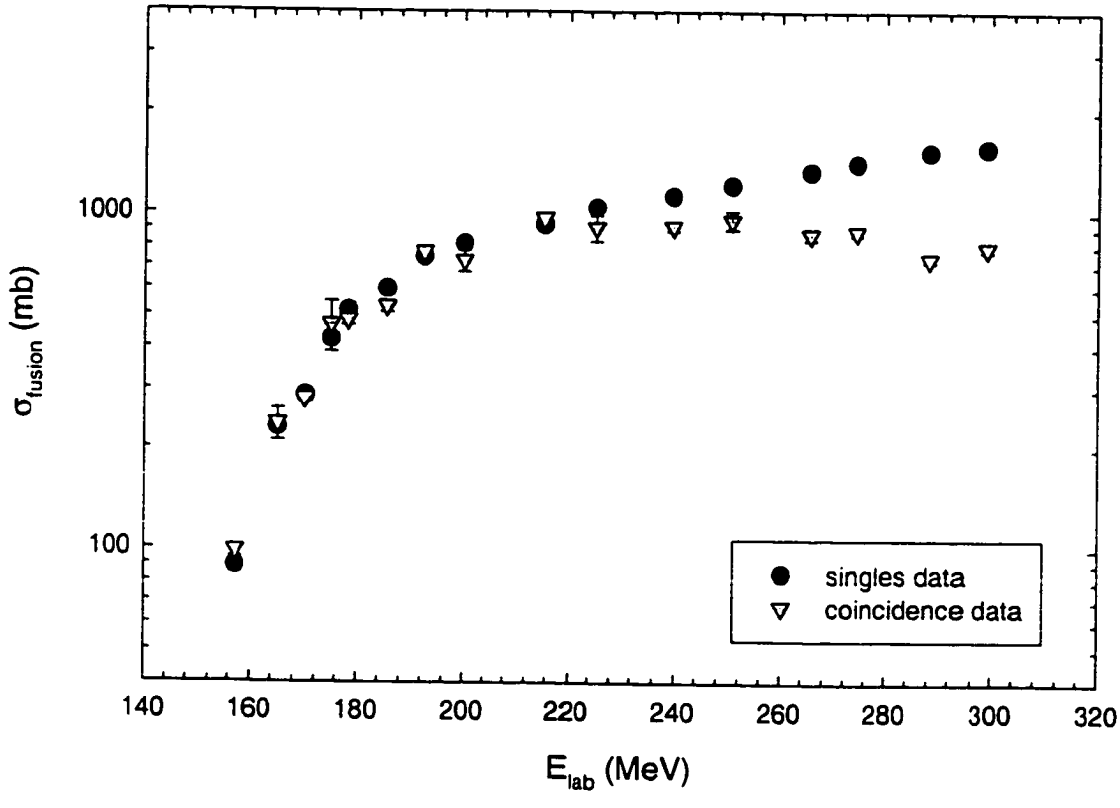

FIGURE 3.14. Comparison of the singles and coincidence excitation functions for the $^{32}S + ^{181}Ta$ reaction.

TABLE 3.4. Cross sections for the ^{32}S + ^{181}Ta reaction.

E_{lab} (MeV)	σ_{fis}(singles) (mb)	σ_{fis}(coinc) (mb)
157.3	89 ± 4	88 ± 4
165.1	230 ± 4	220 ± 20
170.2	290 ± 7	320 ± 10
175.1	420 ± 8	430 ± 70
178.3	520 ± 25	460 ± 20
185.6	600 ± 17	600 ± 20
192.5	740 ± 19	680 ± 20
200.1	810 ± 16	780 ± 60
215.6	930 ± 12	1000 ± 20
225.3	1040 ± 20	1040 ± 90
239.6	1130 ± 10	1030 ± 30
250.6	1210 ± 20	1130 ± 70
265.5	1340 ± 30	1090 ± 40
274.3	1420 ± 30	1150 ± 30
288.3	1540 ± 10	1030 ± 20
299.1	1580 ± 30	1070 ± 30

in the momentum transfer distributions corresponding to approximately 87% of full momentum transfer can also be observed. Figures 3.15 and 3.16 show the momentum distributions. Fitting of a double Gaussian to the data shows that these incomplete momentum transfer events correspond to roughly 15-30% of the total fission cross section at the highest energies, and account for the differences in cross section between the singles and coincidence data.

In measurements of ^{40}Ar-induced fusion on targets ranging from ^{116}Sn to ^{197}Au and bombarding energies of 222-340 MeV, Delagrange *et al.* [Del79] observed forward-peaked emission of ^{1}H and ^{4}He. The cross sections for the ^{4}He component corresponded to up to 20% of the fission cross section, and the authors discussed the probable inclusion of an incomplete fusion component as well as complete fu-

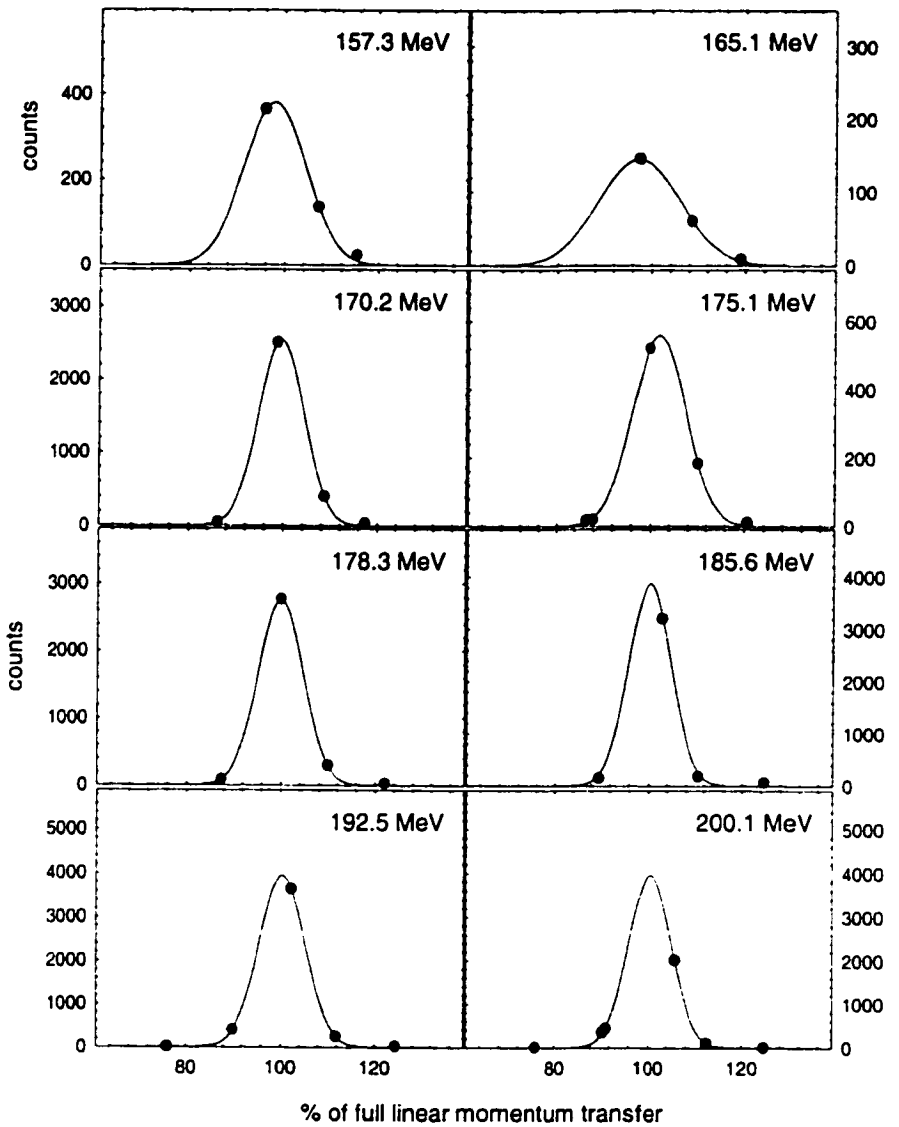

FIGURE 3.15. Momentum distributions for the ^{32}S + ^{181}Ta data (continued on following page).

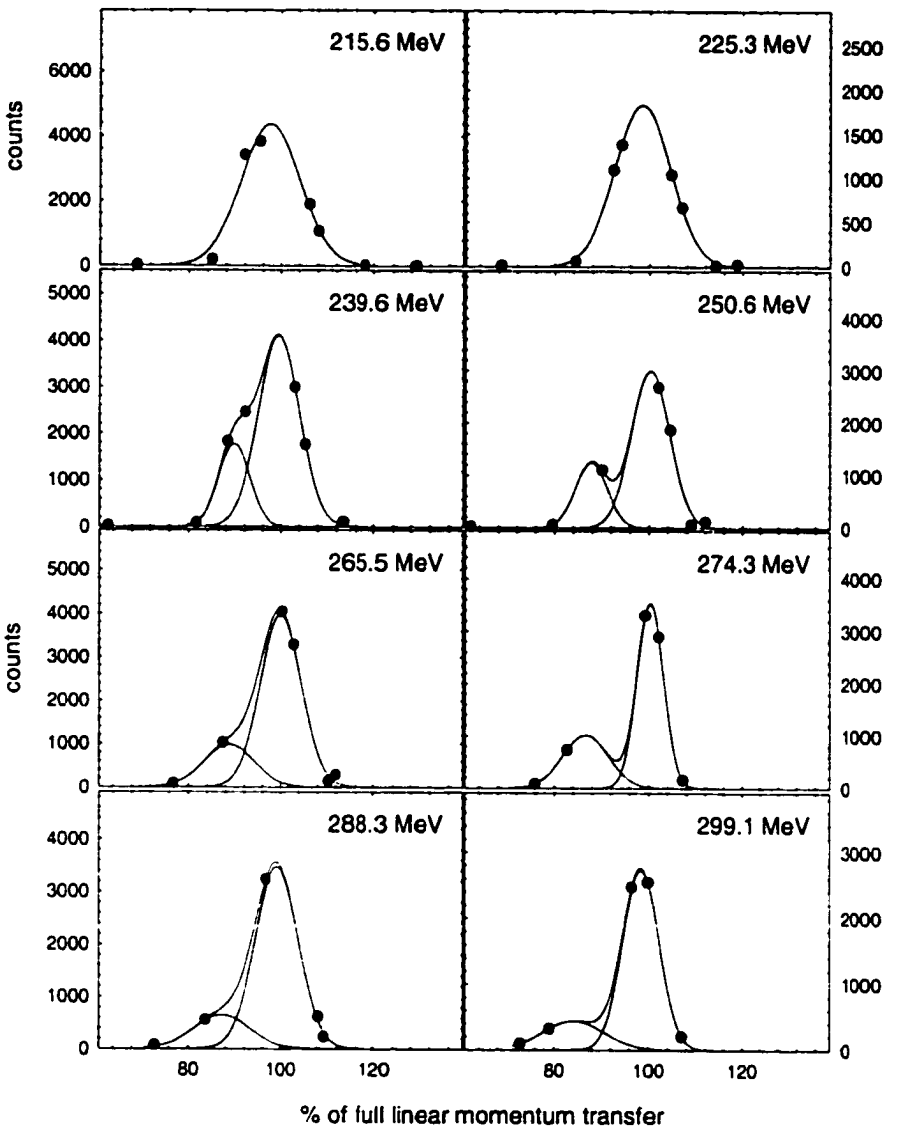

FIGURE 3.16. Momentum distributions for the $^{32}S + ^{181}Ta$ data (continued from previous page).

sion in the fission data. Siwek-Wilczyńska and Wilczyński [Siw79, Wil80b, Wil82] proposed that incomplete fusion reactions could be understood in terms of a disappearance of the pocket in the internuclear potential with increasing angular momentum. For partial waves above the critical angular momentum, escape of some portion of the projectile would remove some linear and angular momentum from the system, thus restoring a pocket in the potential and allowing fusion of the remaining projectile fragment. Following this interpretation, Huizenga, Tubbs, and their colleagues [Hui83, Tub85] looked at ^{20}Ne-induced fission using targets from ^{165}Ho to ^{238}U. The data could be well reproduced by decomposing the angular correlation data into components corresponding to full momentum transfer and one-, two-, and three-alpha escape. The relative yields for the ^{20}Ne + ^{181}Ta reaction at 292 MeV bombarding energy showed roughly 60% of the reaction strength to be in the FLMT peak, and about 30% in the one-alpha escape component, which is similar to the proportions observed in the ^{32}S + ^{181}Ta data.

For the ^{32}S + ^{181}Ta reaction, at the highest energies the maximum angular momentum ℓ_{max} of the compound system is well above the critical angular momentum for fusion. Wilcke gives the critical angular momentum for ^{32}S + ^{181}Ta to be $\ell_{crit} = 96$, while the Bass model predicts $\ell_{crit} = 87$; however, in the experimental data, the cross sections indicate angular momenta in excess of $120\hbar$ at the highest bombarding energies. It can be argued, then, that the incomplete momentum transfer events correspond to the highest partial waves, with angular momenta too high to permit complete fusion. In Figure 3.17, the linear momentum of the incomplete transfer peak is plotted as a function of bombarding energy. The lines show full momentum transfer for projectiles with mass $A = 28$ to 32, corresponding to escape of projectile fragments up to an alpha particle. A correlation is observed between the

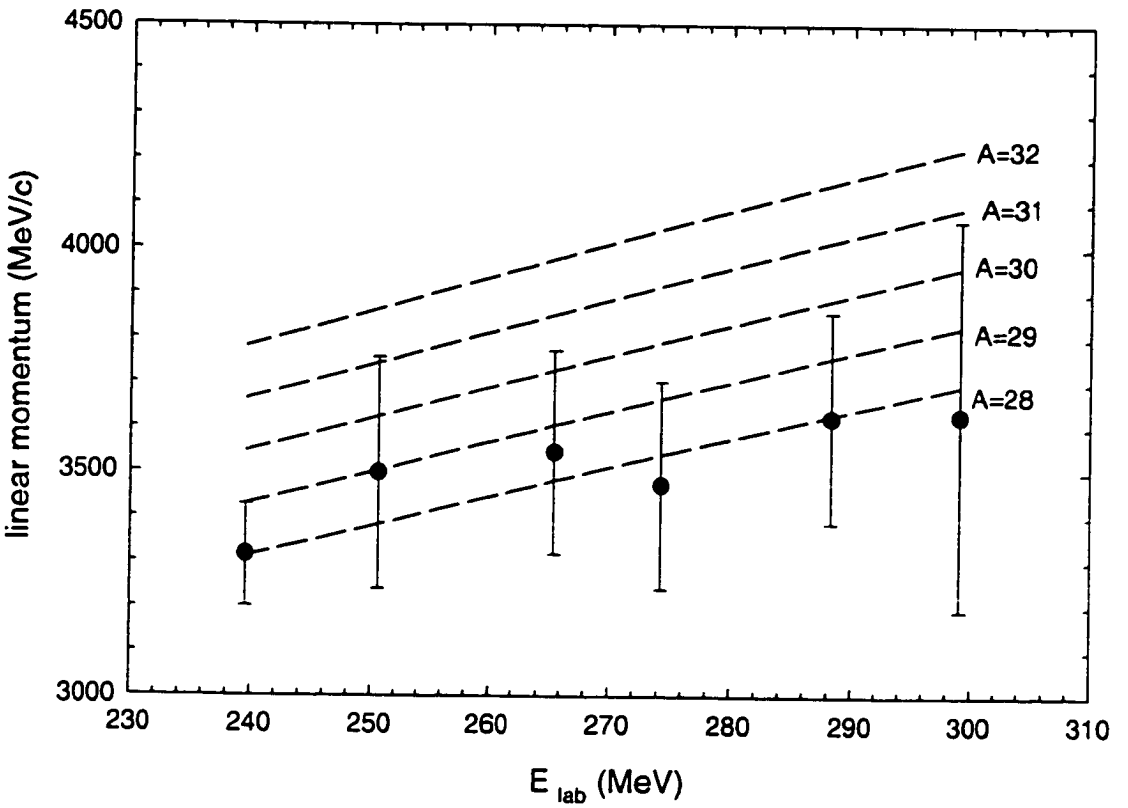

FIGURE 3.17. Linear momentum transfer for the incomplete transfer peak. The guidelines correspond to full momentum transfer for projectiles of mass 28 to 32.

data and the $A_{projectile} = 28$ calculation, and so the incomplete momentum transfer component could be interpreted as escape of an alpha from the ^{32}S projectile.

3.4. Quasifission

3.4.1. Background

In discussing quasifission, the rotating liquid drop model and the statistical transition state model are the commonly accepted framework for describing the fission process. The rotating liquid drop model [Coh74] treats the fissioning system as a charged, rotating liquid with surface tension, and describes the equilibrium shapes of the system in terms of a balance between the attractive surface energy E_s, the repulsive Coulomb energy E_c, and the rotational energy E_{rot}. The ground state shape and the saddle point shape, or the shape where fission becomes inevitable, are determined by the mass and charge of the system and by the angular momentum. The system is parametrized by two dimensionless variables: x, which is usually called the fissility, is given by

$$x = \frac{E_c}{2E_s} = \frac{1}{50.883\left[1 - 1.7826\left(\frac{N-Z}{A}\right)^2\right]} \cdot \frac{Z^2}{A} \tag{3.17}$$

and y, the angular-momentum-dependent term, is written

$$y = \frac{E_{rot}}{E_s} = \frac{1.9249}{\left[1 - 1.7826\left(\frac{N-Z}{A}\right)^2\right]} \cdot \frac{\ell^2}{A^{7/3}} \tag{3.18}$$

The bracketed term in the denominator of these equations is derived from the liquid drop surface energy γ, which can be written

$$\gamma = 0.9517\left[1 - 1.7826\,\mathrm{I}^2\right]\ \mathrm{MeV/fm^2}, \tag{3.19}$$

$$\mathrm{I} = \frac{N_{CN} - Z_{CN}}{A_{CN}} \tag{3.20}$$

For a system with $x = 1$, the fission barrier vanishes at zero angular momentum. For systems with $x < 1$, the fission barrier decreases and the saddle point configuration becomes more compact with increasing angular momentum. This fissility parameter is the most commonly used predictor for determining whether quasifission will be present in a given system, as will be described below.

In the statistical transition state model (STSM) for fission [Boh56], the K-distribution (where K is the projection of the angular momentum on the nuclear symmetry axis) may change during the evolution of the fissioning system up to the saddle point. At the saddle point, K_0^2 (the variance of the K distribution) is thought to be frozen in, and does not change further during the descent from saddle to scission. Under this assumption, the fission fragment angular distributions can be modeled as described in Section 3.1.1. K_0^2 is related to the moments of inertia of the fissioning system as shown in Equation 3.4, and it has been demonstrated for alpha- and heavy-ion-induced reactions [Vio63, Kar68] that the experimental angular distributions correspond to the moments of inertia for the liquid drop model saddle point shapes.

Many cases in which the angular distributions deviate from the standard RLDM/STSM description of fission have been observed, however. For heavy systems or high bombarding energies, the maximum angular momentum can exceed the point where the RLDM fission barrier vanishes, and so an equilibrated compound nucleus is impossible. Fissionlike fragments have nonetheless been observed from these systems [Bor81, Bac81], and the process of collision and reseparation in a system without a barrier has been termed "fast fission". Angular distributions

which cannot be described by the transition state model have also been observed in systems with nonvanishing fission barriers [Ros83, Bac83, Bac85a]; these have been taken to be evidence of "quasifission", a process described by the dynamical model for fusion.

Swiatecki's dynamical model for fusion [Swi81, Swi82] has been successful in describing fusion data for which one-dimensional models fail, especially in the case of medium to heavy systems. The fusing system is treated in terms of a multidimensional potential surface, where the relevant degrees of freedom are mass asymmetry, fragment separation, and neck size. Three configurations are taken to be important in the evolution of the system: the contact configuration, where neck formation becomes favorable; the conditional saddle point, which has frozen mass asymmetry; and the unconditional saddle point, which is the fission saddle point. A schematic diagram for a system in which all three configurations are distinct is shown in Figure 3.18. For light systems, passing the contact configuration is sufficient condition for fusion; for heavier systems or those with high angular momentum, however, the contact point is outside the conditional saddle point, and so an extra amount of radial energy (the "extra-push" energy E_x), is needed above the contact threshold in order to induce fusion. Swiatecki estimates that the extra-push energy is required for systems with an effective fissility x_{eff} greater than 0.57, where x_{eff} is defined analogously to the fissility of Equation 3.17:

$$x_{eff} = \frac{3Z^2e^2}{40\pi\gamma R^3} \tag{3.21}$$

For some symmetric or heavy systems, the conditional saddle point no longer lies at a more compact configuration than the unconditional (fission) saddle; in this situation, the energy beyond the contact threshold needed to pass both the unconditional and conditional saddles is called the "extra-extra-push" energy. It is possible for a

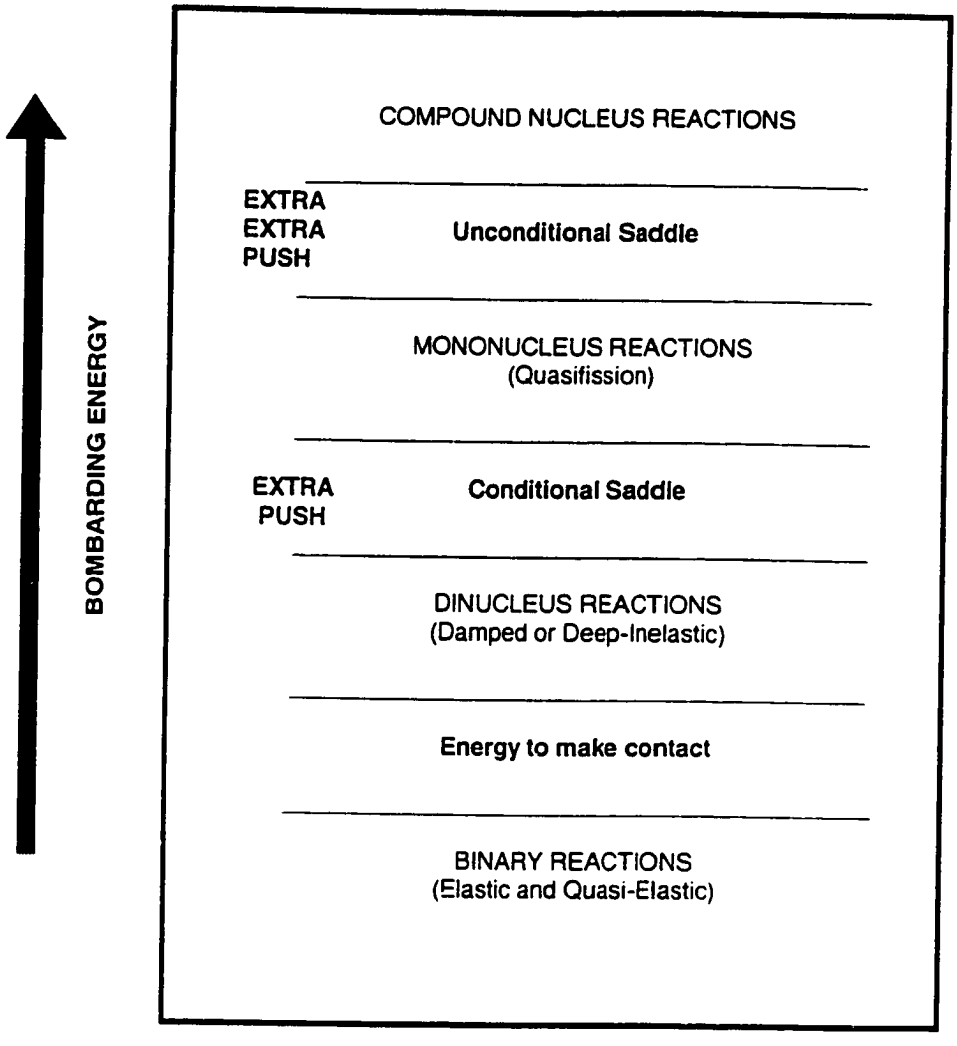

FIGURE 3.18. Schematic diagram of the evolution of a fusing system in Swiatecki's dynamical model.

system of this type to form a mononucleus but not a true, equilibrated compound nucleus: as the system evolves in mass asymmetry inside the conditional saddle point, the increasing repulsion as the charge product Z_1Z_2 increases can be sufficient to cause reseparation without passage of the unconditional saddle. Swiatecki called reactions of this type "quasifission". The extra-extra-push energy is especially relevant in synthesis of the heaviest elements, where use of Pb and Bi targets has resulted in minimization of the compound nucleus excitation energy. However, these systems have lower cross sections than those using actinide targets, because of the "dynamical" hindrance of the extra-extra-push. From comparison with experimental data for synthesis of actinide residues [Gäg84], Gäggeler *et al.* determined a fissility of $x_{eff} = 0.72$ to be the threshold for the onset of quasifission and the extra-extra-push. Variations of the effective fissility have been suggested to be relevant as well, including a mean fissility which is the geometric average of the effective fissility and the fissility of the compound nucleus; and an effective fissility after charge equilibration of the collision partners, x_{eff}^{eq}. Gäggeler *et al.* compared these to the experimental residue data, and demonstrated that in addition to the effective fissility, the data could be well-described by a mean fissility calculated using x_{eff}^{eq}, with a threshold value of 0.72.

3.4.2. Relating angular distributions to quasifission

The use of fission fragment angular distributions to discriminate between compound-nucleus fission and quasifission has been proposed by Back *et al.* [Bac83, Bac85a]. Since the anisotropy in the angular distribution increases with increasing deformation of the fissioning system, anisotropies larger than those predicted by the rotating liquid drop model shapes would indicate that the system had not passed

inside the fission saddle point. By fitting the experimental angular distributions and allowing K_0^2 to vary to achieve the best fit, experimental values for the ratio of the moments of inertia $\mathcal{J}_0/\mathcal{J}_{\text{eff}}$ can be extracted, as in Equation 3.4. Back *et al.* [Bac85b] compared these experimental moments of inertia to predictions of the RLDM saddle point shapes for many systems of varying mass and mass asymmetry. For projectiles lighter than ^{24}Mg, the data could be described by the rotating liquid drop model, but for ^{24}Mg and heavier projectiles, the anisotropies of the angular distributions were significantly larger than RLDM predictions. This agreed qualitatively with the Swiatecki model in that increasing mass and decreasing mass asymmetry resulted in quasifission, but suggested the onset of quasifission at quantitatively larger mass asymmetries than the initial model predictions. By fitting the angular distributions using K_0^2 values corresponding to the RLDM moments of inertia for partial waves below an experimentally determined critical angular momentum, and values corresponding to a point outside the fission saddle for higher partial waves, Back *et al.* were able to quantitatively estimate the fraction of fission events that were due to quasifission.

3.4.3. Application to the ^{32}S + ^{181}Ta data

In order to make an estimate of the quasifission component of the ^{32}S + ^{181}Ta data, the angular distributions were analyzed according to the methods of Back, Keller, and their colleagues, who have treated the ^{32}S + ^{182}W,^{208}Pb systems using the approach outlined above [Kel87, Tsa83, Bac85b]. It was assumed that the cross section consists of two components, with partial waves less than or equal to the critical angular momentum resulting in compound nucleus formation, while

those with angular momentum greater than ℓ_{crit} lead to quasifission. Moments of inertia for the partial waves were assigned as follows:

$$\frac{\mathcal{J}_0}{\mathcal{J}_{\text{eff}}} = \left(\frac{\mathcal{J}_0}{\mathcal{J}_{\text{eff}}}\right)_{RLDM} \qquad \ell \leq \ell_{crit}, \tag{3.22}$$

$$= 1.5 \qquad \ell > \ell_{crit} \tag{3.23}$$

where the RLDM values were calculated using a modified fissility $x = x_{RLDM} + 0.03$, and the arbitrary value of $\mathcal{J}_0/\mathcal{J}_{\text{eff}} = 1.5$ for the highest partial waves corresponds to a shape intermediate between the scission shape and touching spheres. The angular distributions were fitted as described in Section 3.1.1, using a two-component fit in K_0^2 to determine the relative strengths of the complete fusion and quasifission contributions. K_0^2 values were assigned to each partial wave using the moments of inertia described above, varying ℓ_{crit} to give the best fit to the experimental data. These fits are shown in Figures 3.19 and 3.20. It should be noted that, since the data for energies of 239.6 MeV and higher contain an incomplete fusion component, the deduced complete fusion cross sections are probably incorrect.

The resulting cross sections for true compound nucleus formation are given in Table 3.5 and shown in Figure 3.21; according to this analysis, roughly half the fission yield is attributable to quasifission. Back *et al.* estimate that this method of determining the quasifission correction factors is accurate to 20%, and so the uncertainty in the data was assigned using the uncertainties of the fission cross sections and assuming a 20% uncertainty in the correction factors. When compared with the results of the quasifission analysis for the ^{32}S + ^{182}W system [Kel87], the magnitude of the quasifission corrections determined in this analysis are in good agreement with those of the previously published work. The "true complete fusion" excitation function was then fitted using the same methods as for the fission excitation function in order to extract the true fusion barrier. For the

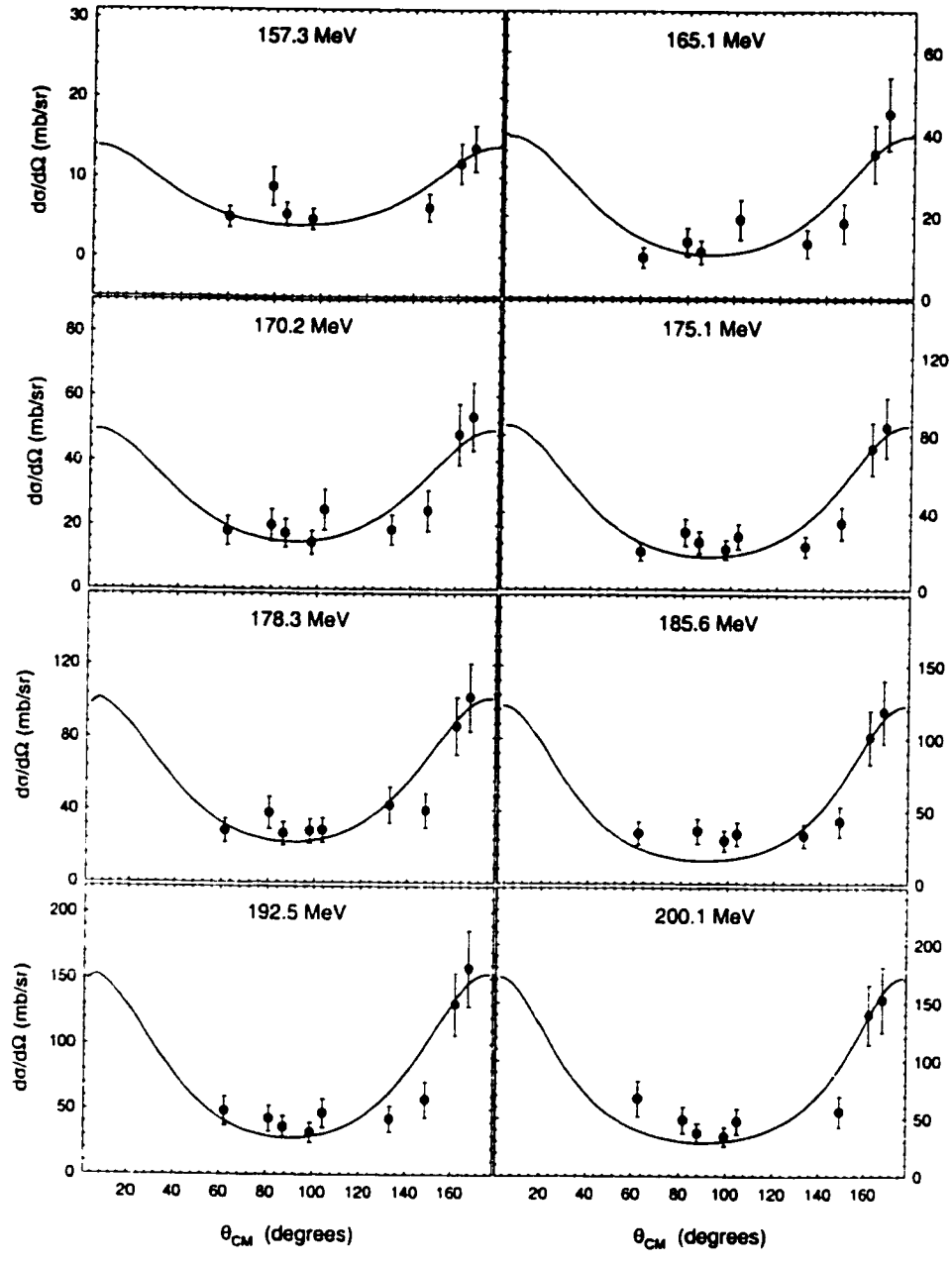

FIGURE 3.19. Fission fragment angular distribution fits used in determining the complete fusion cross sections. (Continued on following page.)

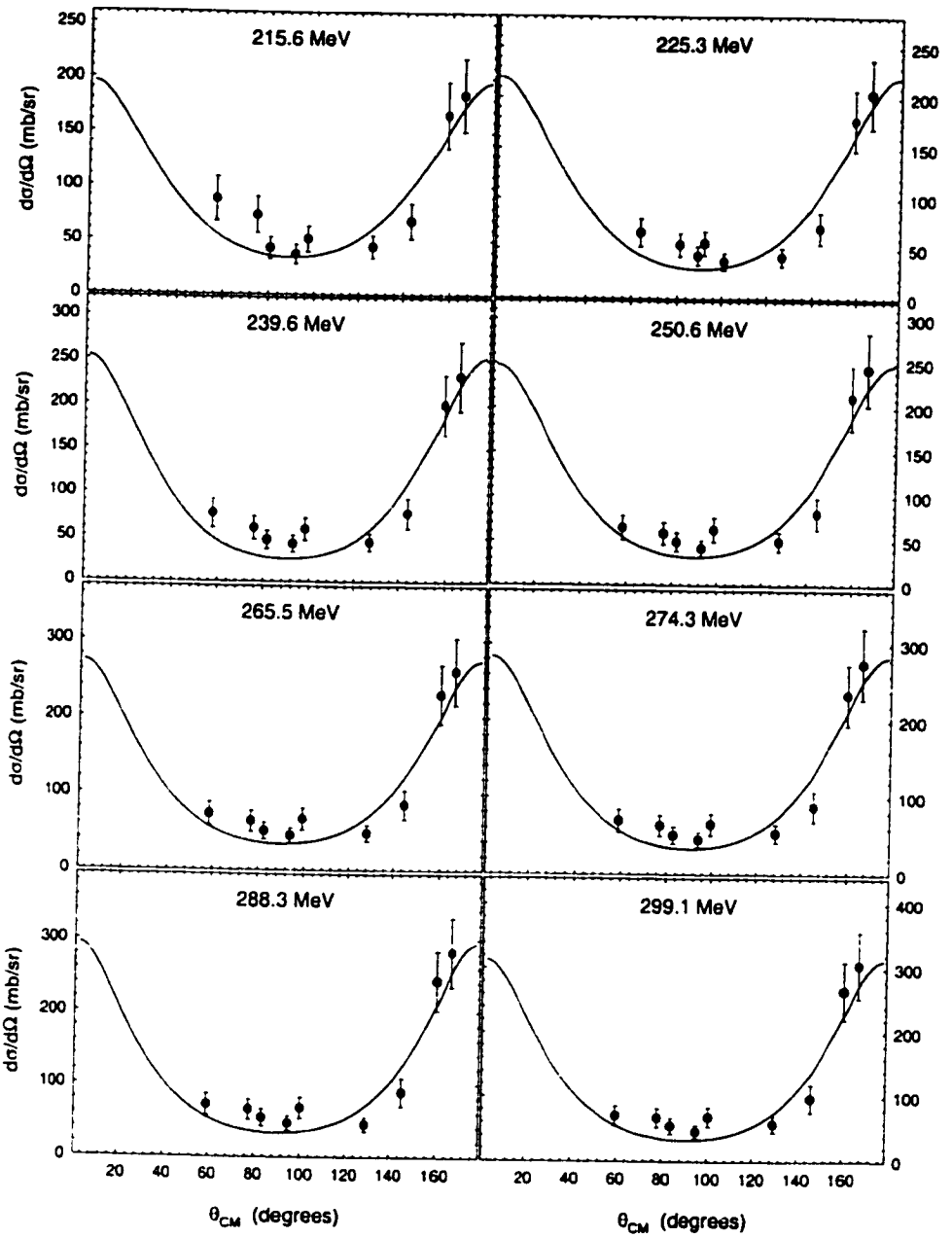

FIGURE 3.20. Fission fragment angular distribution fits used in determining the complete fusion cross sections. (Continued from previous page.)

TABLE 3.5. Compound nucleus cross sections and estimated extra-extra-push energies (from Equations 3.24 to 3.26) for the ^{32}S + ^{181}Ta reaction.

E_{lab} (MeV)	E_{cm} (MeV)	σ_{fis} (mb)	σ_{CN} (mb)	E_{xx} (MeV)
157.3	133.7	88 ± 4	14 ± 4	2.4 ± 0.5
165.1	140.3	220 ± 20	60 ± 10	6.8 ± 0.7
170.2	144.6	320 ± 10	220 ± 50	4.3 ± 2.2
175.1	148.8	430 ± 70	300 ± 40	5.4 ± 2.7
178.3	151.5	460 ± 20	420 ± 50	2.0 ± 2.3
185.6	157.7	600 ± 20	340 ± 60	12 ± 3
192.5	163.6	680 ± 20	540 ± 80	6.8 ± 3.9
200.1	170.0	780 ± 60	700 ± 160	3.8 ± 8.5
215.6	183.2	1000 ± 20	700 ± 140	16 ± 7
225.3	191.5	1040 ± 90	830 ± 160	12 ± 10
239.6	203.6	1030 ± 30	960 ± 190	5 ± 13
250.6	213.0	1130 ± 70	860 ± 170	20 ± 13.
265.5	225.6	1090 ± 40	700 ± 140	34 ± 12
274.3	233.1	1150 ± 30	930 ± 160	20 ± 14
288.3	245.0	1030 ± 20	730 ± 140	33 ± 16
299.1	254.2	1070 ± 30	860 ± 180	24 ± 21

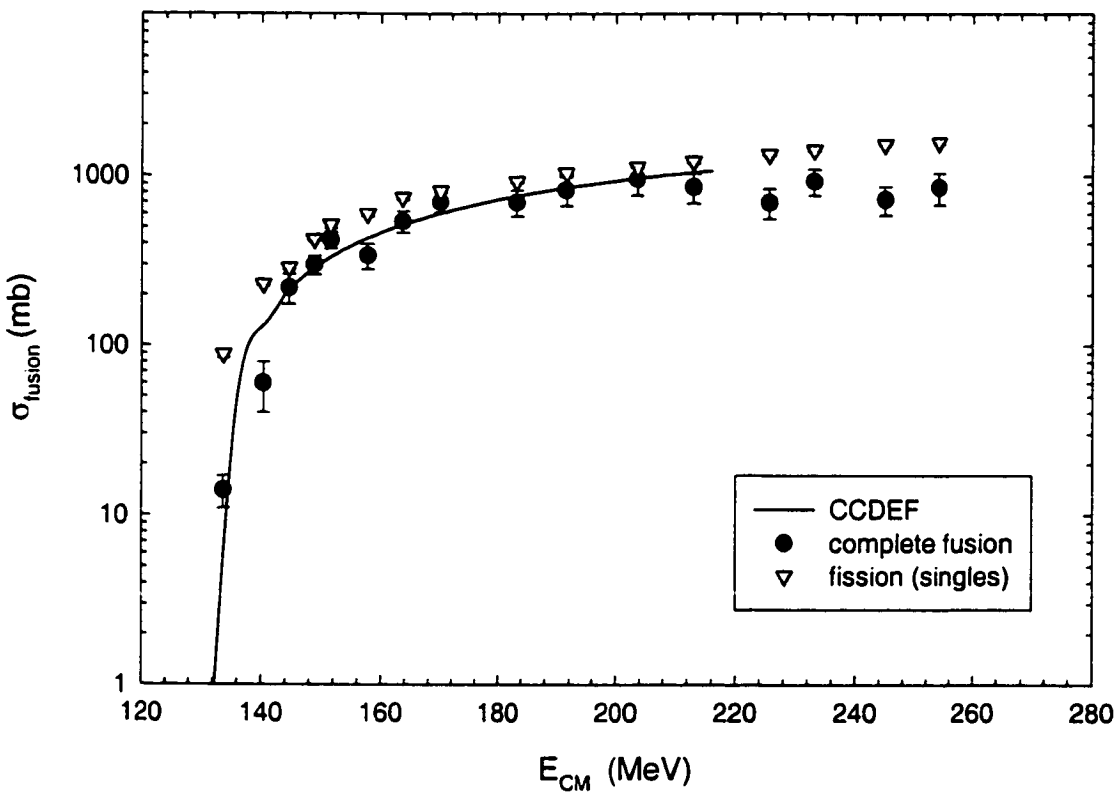

FIGURE 3.21. Comparison of the cross sections for fission and compound nucleus formation for the $^{32}S + ^{181}Ta$ reaction.

TABLE 3.6. Deduced barriers and barrier radii for the ^{32}S + ^{181}Ta true complete fusion data.

data set, fit method	V_b (MeV)	R_b (fm)
fission	130.7 ± 0.3	10.3 ± 0.1
complete fusion (1/E)	133.1 ± 8.1	8.9 ± 1.0
complete fusion (CCDEF)	133.1 ± 6.6	9.4 ± 0.9

fit with CCDEF, the same parameters were used as for the fit to the fission data, and coupling to the Ta static deformation was included. As with the fission data, results of the classical and coupled-channels methods are in agreement; these values are listed in Table 3.6. Figures 3.21 and 3.22 show the coupled-channels and classical fits to the excitation function. Reduced χ^2 for the 1/E fit was 0.55, and for the CCDEF fit was 0.71.

The barrier for true complete fusion has been shifted up by 2.4 MeV as compared to the "capture" barrier of the fission excitation function. It is interesting to note, also, that the barrier radius for true complete fusion has shifted from 10.3 fm to 8.9 fm, which could be attributed to the more compact shape necessary for complete fusion.

Again following the methods of Back [Bac85a], the deduced true complete fusion cross sections can be used to estimate the extra-extra-push energies for the system. The energy necessary for capture can be written as

$$E_{CM} = V_0 + \frac{\ell^2_{touch}\hbar^2}{2\mu R_0^2} \tag{3.24}$$

and the energy for complete fusion, as

$$E_{CM} = V_0 + E_{xx} + \frac{\ell^2_{CN}\hbar^2}{2\mu R_0^2} \tag{3.25}$$

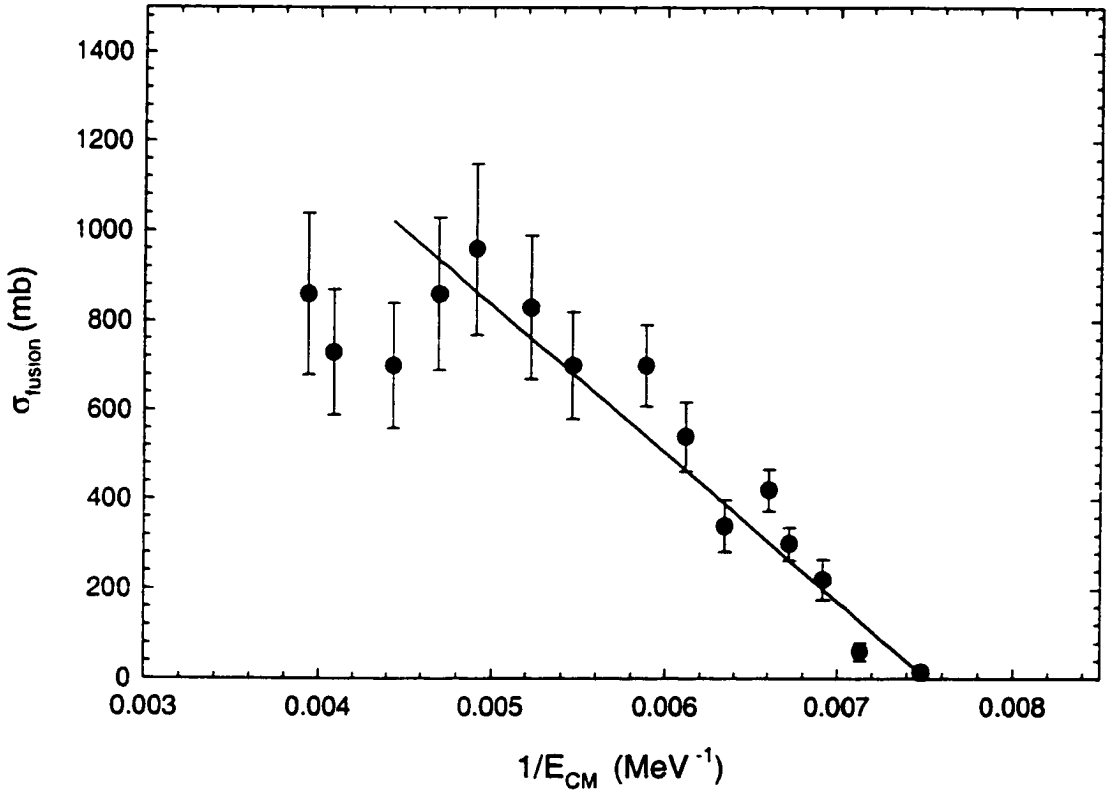

FIGURE 3.22. Classical fit to the ^{32}S + ^{181}Ta complete fusion data.

Since the cross section is proportional to the square of the maximum ℓ-wave, the ratio of the cross sections for capture and true complete fusion can be used to find the extra-extra-push energy:

$$\frac{\sigma_{CN}}{\sigma_{touch}} = \frac{\ell^2_{CN}}{\ell^2_{touch}} = 1 - \frac{E_{xx}}{E_{CM} - V_0} \tag{3.26}$$

The values for the extra-extra-push energies deduced by this method are given in Table 3.5. The increase in E_{xx} with increasing bombarding energy is due to the increasing maximum angular momentum, up to the critical angular momentum, where the values saturate.

The experimentally deduced extra-extra-push energies can be extrapolated to a value at zero angular momentum, which is the "E_{xx}" commonly discussed in the literature. In the dynamical model, the extra-extra-push energy is related to an angular-momentum-dependent mean fissility $x_m(\ell)$ by

$$E_{xx} = E_{ch} \cdot a^2 \left[x_m(\ell) - x_{th}\right]^2 \tag{3.27}$$

where x_{th} is the threshold fissility for the onset of quasifission, a, the slope parameter, is a constant, and $x_m(\ell)$ can be related to the mean fissility at zero angular momentum x_m by

$$x_m(\ell) = x_m + f' \cdot \left(\frac{\ell}{\ell_{ch}}\right)^2 \tag{3.28}$$

The quantities E_{ch} and ℓ_{ch} are the characteristic energy and angular momentum of the system, which are model parameters (see [Bjø82]). The angular momentum term in $x_m(\ell)$ is corrected by f', which assumes that only a fraction of the total angular momentum will remain in the orbital motion. Following the procedure of Back *et al.*, a value of $f' = 0.6$ was used. Using Equation 3.27, the value of the extra-extra-push at zero angular momentum can be extrapolated from the experimental

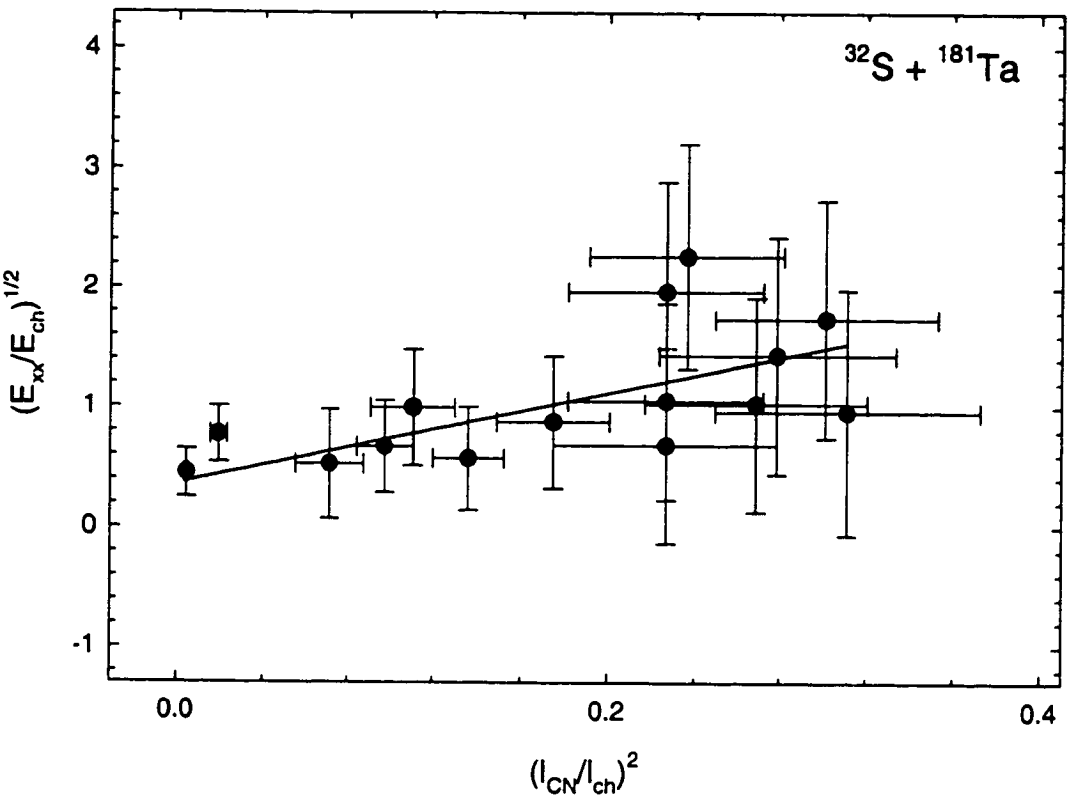

FIGURE 3.23. Fits to the experimental estimates of the extra-extra-push energies.

data by fitting the equation

$$\sqrt{\frac{E_{xx}}{E_{ch}}} = a''\,(x_m - x''_{th}) + a''f' \cdot \left(\frac{\ell_{CN}}{\ell_{ch}}\right)^2 \tag{3.29}$$

where the double-primed values indicate experimentally determined quantities. Figure 3.23 shows these fits to the experimental estimates of E_{xx}. As in the 1/E fits, only data below σ = 800 mb were used in the fits, to avoid the nonlinearities at high energies. The best-fit parameters were $a'' = 6.3$ and $x_{th} = 0.59$. These results are in reasonable agreement with the values obtained by Back for projectiles from ^{19}F to ^{32}S on ^{208}Pb, where the deduced parameters were $a'' = 8 \pm 2$ and

$x_{th} = 0.63 \pm 0.03$. In an analysis of quasifission in ^{238}U-induced reactions, Shen *et al.* [She87] also found that experimentally-determined extra-extra-push energies for ^{238}U + (^{16}O, ^{26}Mg, ^{27}Al, ^{32}S, ^{35}Cl) could be described by x_{th} values of 0.59 to 0.64. The extra-extra-push energies at zero angular momentum were deduced from these fits to be $E_{xx} = 2.5 \pm 2.4$ MeV, which agrees with the observed barrier shift.

Although Back *et al.* estimate the values for the quasifission contribution as determined in this manner to be accurate to about 20%, it should be noted that there are several approximations inherent in this analysis. Assuming a sharp cutoff of angular momentum values is a simplistic approach; in reality there is probably a more gradual transition between the two components. The value for the ratio of the moments of inertia of the quasifission component was taken to be $\mathcal{J}_0/\mathcal{J}_{\text{eff}} = 1.5$, but a different estimate of the shape of the mononucleus would give different values for the relative contributions of fusion and quasifission. The angular distribution fits were made using the singles fission data, where there was no requirement of full momentum transfer. At the highest energies, there may be contamination from incomplete fusion events, and for this reason, calculated complete fusion cross sections above 239 MeV bombarding energy were not used in the barrier fits.

Quasifission is a topic which has received much attention in recent literature. Much of the discussion centers on anomalous anisotropies observed in subbarrier reactions of lighter projectiles such as ^{12}C and ^{16}O on heavy, deformed actinide targets [Ram90, Cha94, Hin95, Mor95, Hin96, Van96, Sam96, Maj96]. In very mass-asymmetric systems with light projectiles, quasifission would not be expected; the observed quasifission component has been attributed to collisions with the tips of the deformed targets at subbarrier energies. At energies above the barrier, the anisotropies return to the values expected on the basis of the transition state model. Alternatively, it has been proposed that this subbarrier effect may be due

to fission before K-equilibration [Liu94, Liu96]. Studies of pre-scission neutron emission [Hin89, Hin92, Rud97] indicate that the timescales for fission following complete fusion and quasifission may be very different. With some development, this approach could provide an alternate method for estimating quasifission.

In summary, although qualitative discussions of anomalous angular distributions and quasifission are very much a current topic, the problem of quantitatively unfolding the quasifission and complete fusion components of the fission cross section still remains a complex issue. In this analysis, the best estimates have been made given the available information.

4. $^{38}S + ^{181}TA$ DATA ANALYSIS

The fusion cross sections for the radioactive-beam $^{38}S + ^{181}Ta$ reaction were determined using the same principles as for the stable-beam $^{32}S + ^{181}Ta$ data. A valid event was defined by observation of coincident fission fragments with a folding angle corresponding to full linear momentum transfer, with the additional requirement that the event be in coincidence with a trigger in the beam time-of-flight system within the gate set on the ^{38}S peak. Cross sections for these events were calculated for each bombarding energy, and then were corrected for the efficiency of the detector system by normalization to the known cross sections for the $^{16}O + ^{197}Au$ reaction. The resulting excitation functions were analyzed using both the classical and coupled-channels methods in order to extract the barrier V_b and barrier radius R_b, in the same manner as for the stable-beam data.

4.1. Determination of the cross sections

Since the PPACs used as the primary fission detectors in these experiments are transmission detectors and no energy information was recorded for incident particles, it was not possible to differentiate between fission fragments and scattered beam in the singles data. Because of this, no singles angular distribution information could be extracted, and so determination of the fusion cross sections was based on full momentum transfer events in the coincidence data. In order to determine the folding angles for the coincidence events, the PPACs were position-calibrated using plastic masks as described in Section 2.3.2. Once the laboratory angle (θ, ϕ) with respect to the beam axis was determined for each event in the fission detectors, the folding angles for coincident fission fragments were calculated. Time-of-flight gates were set in the MCP spectra on the ^{38}S and primary satellite peaks, and were

used to select fission events in coincidence with these beam particles. For each bombarding energy, a background measurement was made using an empty target frame. There were no valid fission + fission + beam coincidences observed in any of these background runs, which indicates that the valid events were not triggered by beam scattered from the target frame or other background. In the data acquisition, each detector which triggered was marked by a bit set in the bit register pattern, so the possibility of including any "triple coincidence" fission + fission + background events was eliminated as well. (In the high-rate ^{16}O + ^{197}Au calibration runs, these triple-coincidence events corresponded to only 0.3% of the full momentum transfer peak without any beam gating requirement, and so their occurrence in the radioactive beam data, with its very low event rates, would be unlikely in any case.)

Figure 4.1 shows the beam-gated folding angle distributions for the ^{38}S + ^{181}Ta data. Fusion events for the ^{38}S-induced reaction were selected by cuts on the folding angle distributions at $\pm 15\%$ of the full momentum transfer folding angle. These cuts were sufficient to encompass all the counts in this region of the folding angle distributions (with the exception of the two counts that can be observed at $\theta_{ff} = 150^{\circ}$ in the 237.7 MeV data; despite the fact that they lie just outside the folding angle cut, they appear to be part of the distribution and were included in the fusion data). The only other counts observed were typically at angles much smaller than the FLMT folding angle, and included a hit in one of the two most forward detectors. In most of these cases, the hits were in two detectors on the same side of the beam; these "unphysical" coincidences are most probably due to ^{252}Cf background in coincidence with a scattered beam particle. A ^{252}Cf calibration source was mounted facing backward in the target ladder, and although an aluminum shield was mounted over it to keep the source shielded from

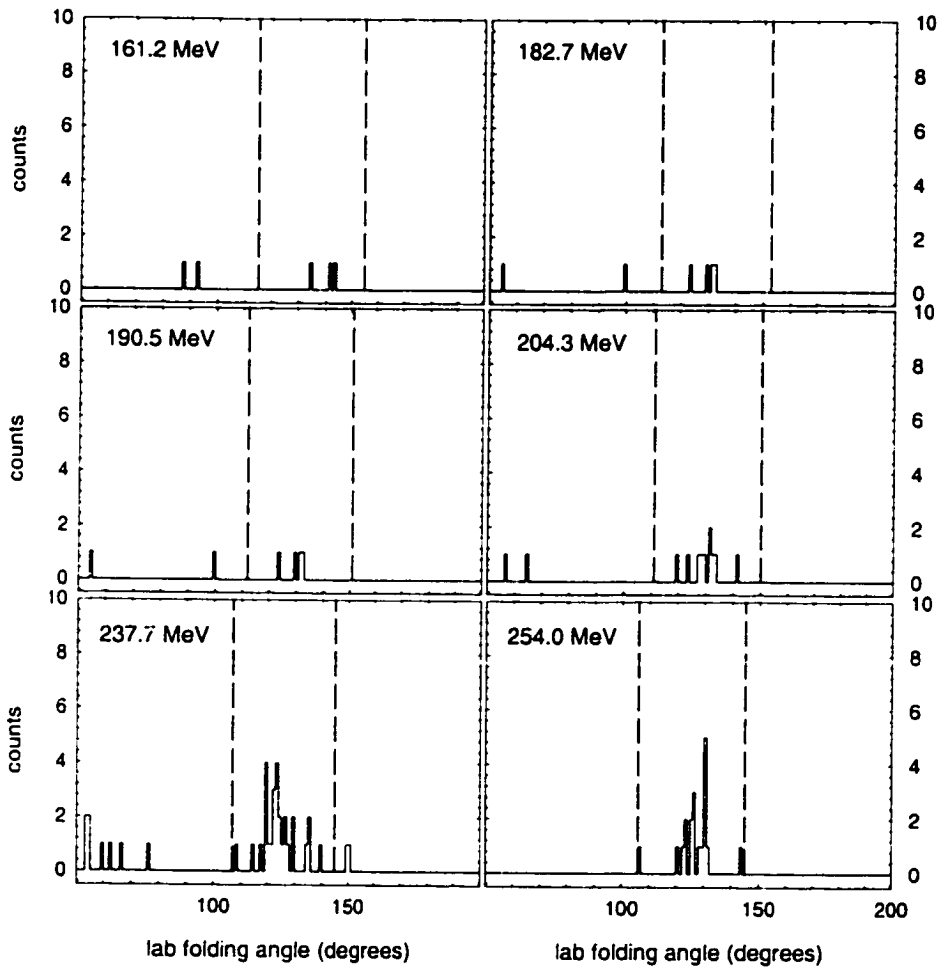

FIGURE 4.1. Beam-gated folding angle distributions for the ^{38}S + ^{181}Ta data.

the detectors when the target was in position, some background was still observable in the detectors, especially in the right PPAC when the target was in the tilted configuration. The rate of these accidental coincidences was approximately one per 10^8 beam particles, or about one every three to four hours at typical beam rates; the typical folding angle for these events was 80-100°.

Cross sections for the FLMT events were calculated as in Section 3.1.1 by correcting for target thickness, beam flux, live time of the acquisition system, solid angle of the detectors, and angular coverage of each detector. For this correction, it was assumed that the angular distributions had a $1/\sin\theta$ shape. To calculate the beam flux, the scaler rates in the PPAC time-of-flight system were used, multiplied by the fraction of the total beam that was ^{38}S.

In order to determine the total efficiency of the detector system, measurements were made of the known ^{16}O + ^{197}Au fusion cross section at two energies [Vio63]. Two calibrations were made at each energy: a high-beam-intensity run with the timing system out of the beamline, in order to calibrate the fission PPACS; and a run with beam intensities attenuated to a few thousand particles per second, in order to determine the efficiency of the entire fission and timing detector system in RNB configuration. In both calibrations, valid events were determined by coincident fission fragments with full momentum transfer as in the ^{38}S runs; for the RNB-configuration calibrations, the additional requirement of a trigger in the beam TOF gate of the timing system was added. The efficiency of the entire detector system was 78% ±4% as determined by the ratio of the observed to the known cross sections for this reaction, and the ^{38}S-induced cross sections were normalized using this calibration. Uncertainties given for the final cross sections are relative uncertainties. They were determined by including the uncertainty in the normalization; taking the error in the scaler readings for the live time and beam rates to be 1%;

and assuming that the ratio of ^{38}S to total beam in the TOF spectra was accurate to 3%. The uncertainty in the angle and solid angle corrections was determined by assuming an error of ± 1 cm in the position of the detectors, and the accuracy of the coincidence count rates was taken to be ± 1 count.

4.2. Evaporation residues

An attempt was also made to observe any evaporation-residue alpha particles which could be detected in the backward silicon strip detectors. Although the statistical code PACE [Gav80] predicts that the product actinium nuclei will decay by fission in greater than 99% of the events, another code, HIVAP [Rei81], which is commonly used for predicting heavy-element cross sections, predicts significant residue cross sections at the lower energies. Figure 4.2 shows the measured fission cross sections for the ^{38}S + ^{181}Ta reaction, along with HIVAP predictions for fission and residue formation. The code predicts the residue cross section at the lowest measured energy, 161.2 MeV, to be 65 mb, or about a quarter of the observed fission cross section. If the residue cross sections are indeed this high, they should be observable, and must be accounted for in the total fusion cross sections.

In the second experiment, the silicon detectors at backward angles were used to look for any residue alphas; these alpha spectra are shown in Figure 4.3. It can be seen that the only observed counts in these spectra were background from the ^{252}Cf calibration source. An upper limit for the residue cross section can be set by assuming that one Ac alpha was observed, and taking the ratio of that to the beam-gated fission counts observed in these detectors. (In empty-target runs, it was determined that the requiring a coincidence with the ^{38}S peak in the time-of-flight system eliminated the ^{252}Cf fission background in these detectors.) This

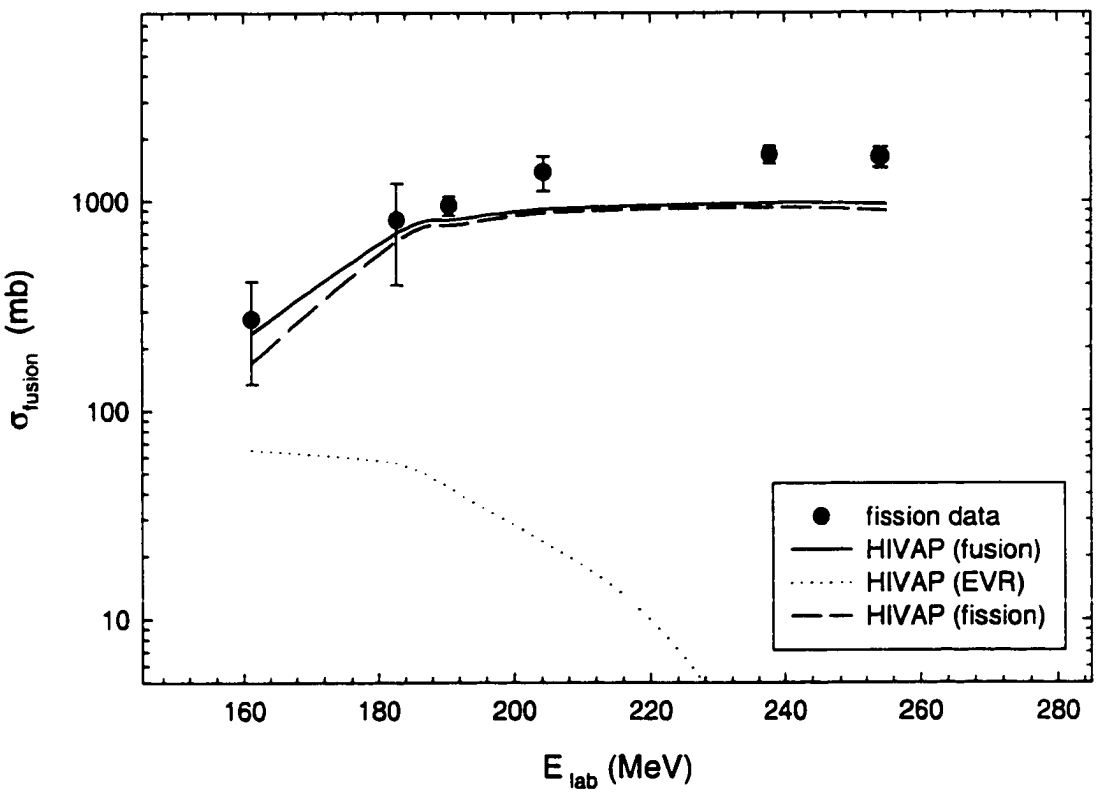

FIGURE 4.2. HIVAP predictions for evaporation residue formation in the ^{38}S + ^{181}Ta system.

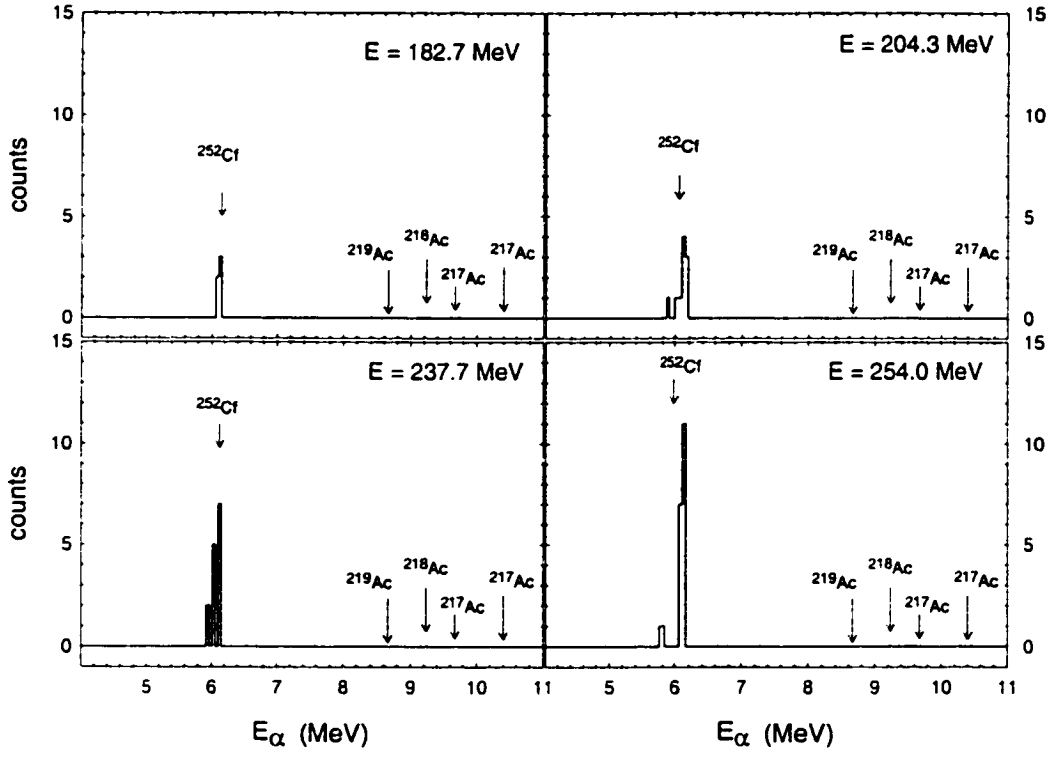

FIGURE 4.3. Alpha spectra for the silicon detectors at backward angles.

TABLE 4.1. Fission cross sections for the $^{38}S + ^{181}Ta$ reaction.

E_{lab} (MeV)	E_{cm} (MeV)	σ_{fis} (mb)
161.2 ± 7.3	133.2 ± 6.0	280 ± 140
182.7 ± 5.8	151.0 ± 4.8	810 ± 410
190.5 ± 7.2	157.4 ± 6.0	950 ± 100
204.3 ± 5.2	168.9 ± 4.3	1380 ± 260
237.7 ± 5.3	196.5 ± 4.4	1670 ± 160
254.0 ± 4.7	209.9 ± 3.9	1620 ± 180

gives an upper limit of 3% at the lowest energy (182.7 MeV), and less than 2% for 204.3 MeV bombarding energy. Taking the HIVAP residue cross sections (56 mb for 182.7 MeV, and 23 mb for 204.3 MeV), it would be expected that three counts would have been observed at 182.7 MeV, and one count at 204.3 MeV; these are not seen in the data. Further support for this comes from the measured residue cross sections for the similar system $^{32}S + ^{184}W$ [Bac99]. The maximum observed residue cross section for this system was measured to be 200 μb, while HIVAP predicts a maximum of 4 mb. Based on these results, it was assumed that, within the precision of this data, the actinium compound nuclei decayed by fission without a significant evaporation residue channel.

4.3. The classical and coupled-channels analysis

The final, normalized cross sections for the $^{38}S + ^{181}Ta$ reaction are given in Table 4.1 and shown in Figure 4.4. The excitation function was analyzed in the same manner as the stable-beam ^{32}S data; that is, a 1/E fit was made to extract the barrier and barrier radius using the classical equation $\sigma = \pi R^2(1 - \frac{V_b}{E})$, and

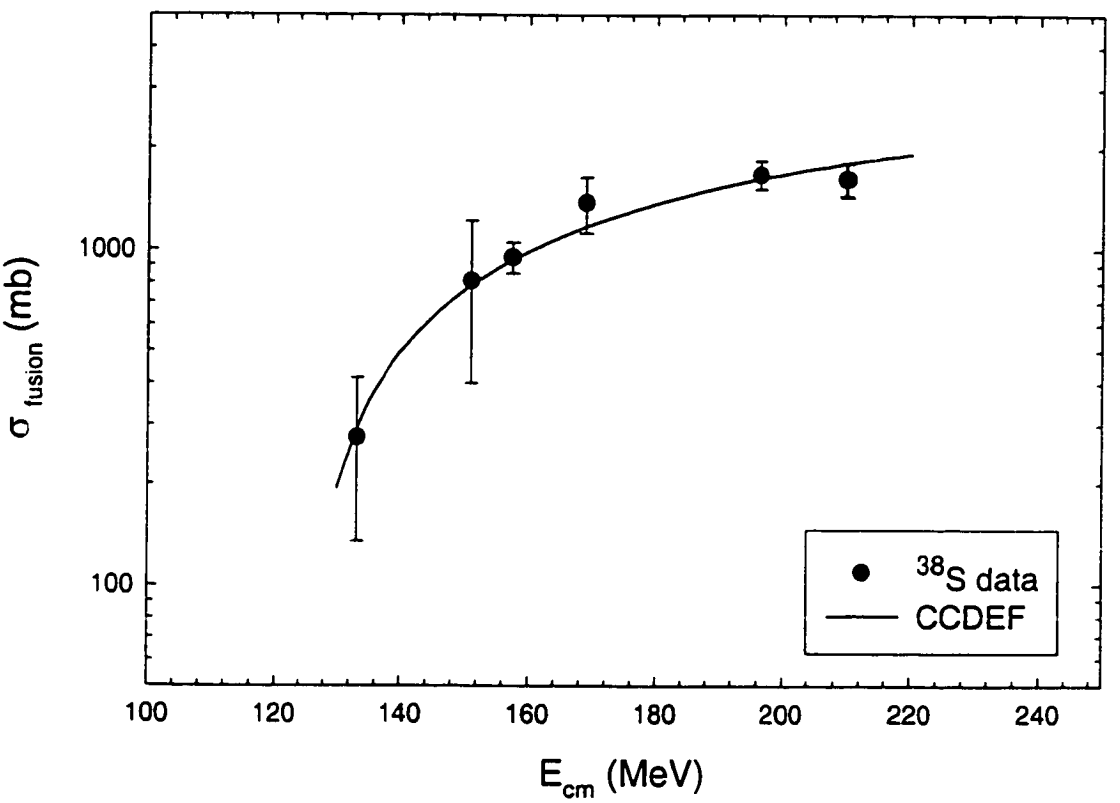

FIGURE 4.4. Excitation function for the $^{38}S + ^{181}Ta$ reaction, and coupled-channels fit to the data.

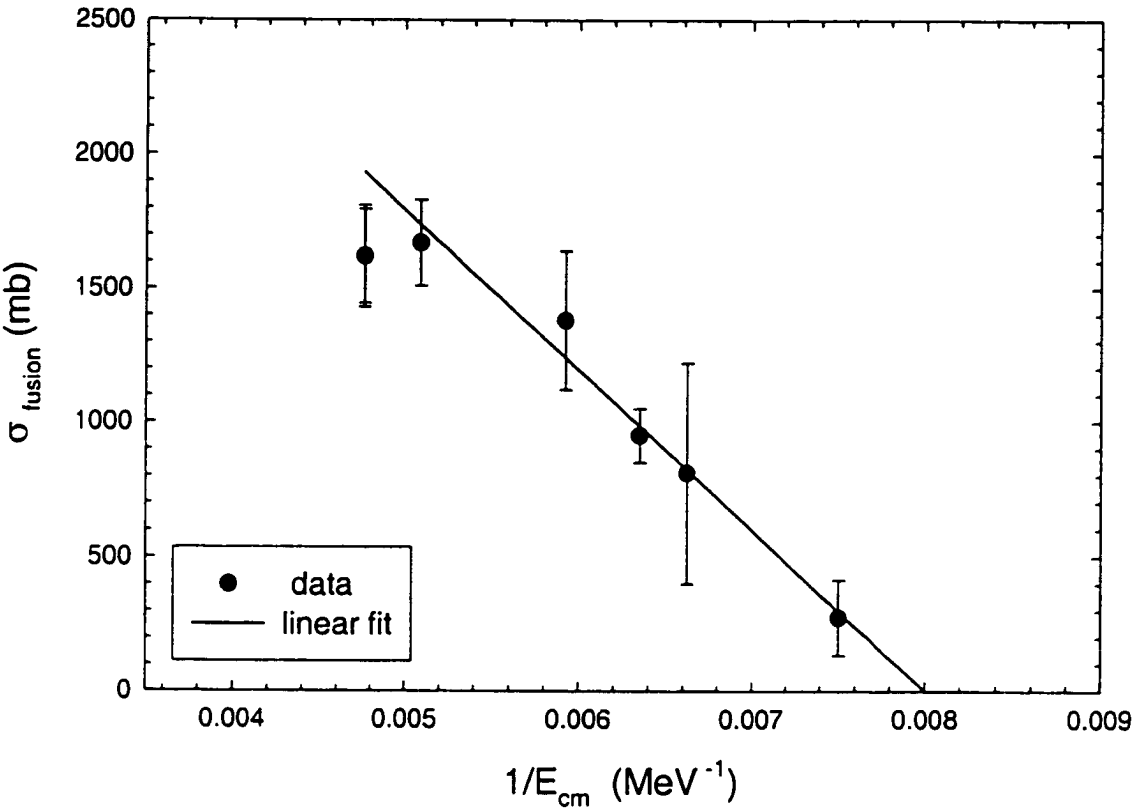

FIGURE 4.5. Linear fit to the cross section vs. 1/E data for the ^{38}S + ^{181}Ta reaction.

a coupled-channels fit was made using the code CCDEF. As before, the classical fit was made including only cross sections smaller than 800 mb, to avoid possible nonlinearities at high energies. This fit is shown in Figure 4.5; the parameters extracted are $V_b = 125.2 \pm 5.3$ MeV, and $R_b = 12.2 \pm 0.4$ fm, with reduced $\chi^2 = 0.49$. These are also given in Table 4.2.

In the coupled-channels fit, the ^{181}Ta static deformation was included using the same values as for the ^{32}S analysis, as given in Section 3.2.5. In this case, the

TABLE 4.2. Fusion barriers and barrier radii for the ^{38}S + ^{181}Ta system.

model	V_b (MeV)	R_b (fm)
experimental (1/E)	125.2 ± 5.3	12.2 ± 0.4
experimental (CCDEF)	124.3 ± 5.9	11.9 ± 0.7
mean	**124.8 ± 0.3**	**12.1 ± 0.1**
Bass [Bas80]	130.1	11.6
Vaz *et al.* [Vaz81]	135.2	11.7
Royer *et al.* [Roy98]	132.1	11.9

^{38}S projectile is also deformed; the measured value for the projectile deformation of $\beta_2 = 0.246$ [Sch96] was also included. As in the ^{32}S case, the lowest-energy data are well above the barrier, and so coupling to additional modes such as vibrational states was unnecessary to describe the data, since these modes have significant effects on the cross section only in the subbarrier region. The best fit to the excitation function (with reduced $\chi^2 = 0.39$) is shown in Figure 4.4. The barrier parameters extracted from this fit are $V_b = 124.3 \pm 5.9$ MeV, $R_b = 11.9 \pm 0.7$ fm, and $\hbar\omega = 3.3$ MeV. (Uncertainties in the coupled-channels fit were determined in the same manner as in the ^{32}S analysis, by using a nonlinear least-squares fit.) These experimental values are given in Table 4.2, along with various model predictions for this reaction. The barrier height and radius as determined by the two fitting methods agree, and it can be seen that as in the ^{32}S case, the measured barriers are lower than all model predictions, with the Bass barrier being the closest match to the data. Again, this can be taken as a first-order indication that the fission cross section is not equivalent to the complete fusion cross section; there is probably some quasifission component in the data. In these experiments, however, event rates were too low to

obtain angular distribution data, and so the quasifission component could not be estimated.

In summary, the cross sections for the radioactive-beam $^{38}S + ^{181}Ta$ reaction were determined using coincident fission fragments corresponding to full momentum transfer. No evaporation residues were observed, and so fission was taken to be the only significant exit channel for the compound system. The resulting excitation function was analyzed using both a classical and coupled-channels approach, in order to extract the barrier height and radius. In the following chapter, the results of this analysis will be compared with that of the stable-beam ^{32}S-induced reaction, in order to determine the enhancement resulting from use of the radioactive neutron-rich beam.

5. RESULTS AND CONCLUSIONS

The object of these experiments was to make a comparison of the $^{32,38}S$ + ^{181}Ta fusion reactions in order to determine the enhancement due to the use of the radioactive neutron-rich projectile. In this chapter, the results of the data analysis for the ^{32}S- and ^{38}S-induced reactions will be compared, and the differences between the reactions will be discussed in the context of heavy-element fusion. Finally, suggestions will be made for future research to clarify and extend the work presented here.

5.1. Comparison of the analysis results

In comparing the excitation functions for the stable-beam and radioactive-beam reactions, there are two topics of interest. First is any observable shift in the height and radius of the interaction barrier, which could allow lower bombarding energies in a synthesis reaction, and consequently lower excitation energies of the fused system. Second, exotic effects such as a soft dipole vibration have been predicted [Agu88, Agu92, Das92, Tak92] to enhance the cross sections for fusion of neutron-rich nuclei, and so the data will be examined for indications of any influence of additional mechanisms in the radioactive-beam reaction for the energy region measured.

Table 5.1 shows the experimental values of V_b extracted from the fission cross sections for the ^{32}S- and ^{38}S-induced reactions. The mean barrier shift resulting from the use of the radioactive neutron-rich ^{38}S is 5.9 ± 0.4 MeV. This shift is on the order of the binding energy of a neutron in heavy nuclei, which is typically 5-6 MeV. Taking into account the difference in fusion Q-values for the two systems, which were calculated using Audi-Wapstra masses [Aud95] to be -80.58 and -86.86 MeV

TABLE 5.1. Comparison of the experimental barrier heights and radii deduced from the fission cross sections.

reaction	$^{32}S + ^{181}Ta$	$^{38}S + ^{181}Ta$	barrier shift
V_b (MeV)	130.7 ± 0.3	124.8 ± 0.3	5.9 ± 0.4
R_b (fm)	10.3 ± 0.1	12.1 ± 0.1	1.8 ± 0.1

for ^{32}S- and ^{38}S-induced fusion, the excitation energy at the barrier is lowered from about 50 MeV for the stable projectile to about 38 MeV for the radioactive beam. In the context of synthesis reactions for heavy nuclei, a lowering of the excitation energy by 12 MeV, which could allow retention of up to two additional neutrons, would increase survival probabilities against fission by orders of magnitude. The lowering of the barrier by use of radioactive neutron-rich projectiles, then, could have a significant impact on production cross sections for the heaviest elements.

It is interesting to ask whether the cross section enhancement seen in the ^{38}S-induced reaction is a straightforward result of the Coulomb barrier shift, or if other exotic effects such as a soft dipole vibration or neck formation may be present. Figure 5.1 shows the excitation functions for the $^{32,38}S + ^{181}Ta$ reactions plotted as reduced cross sections: the differences in barrier have been factored out of the bombarding energy, and the same has been done in the cross sections for the differences in barrier radius. It can be seen that, when the effects of the barrier shift have been removed, the two excitation functions are in agreement. No evidence for an enhancement due to any additional mode is observed. (It should be noted, however, that predictions of enhancement due to the soft dipole vibration focus mainly on increased transmission coefficients at subbarrier energies. It cannot

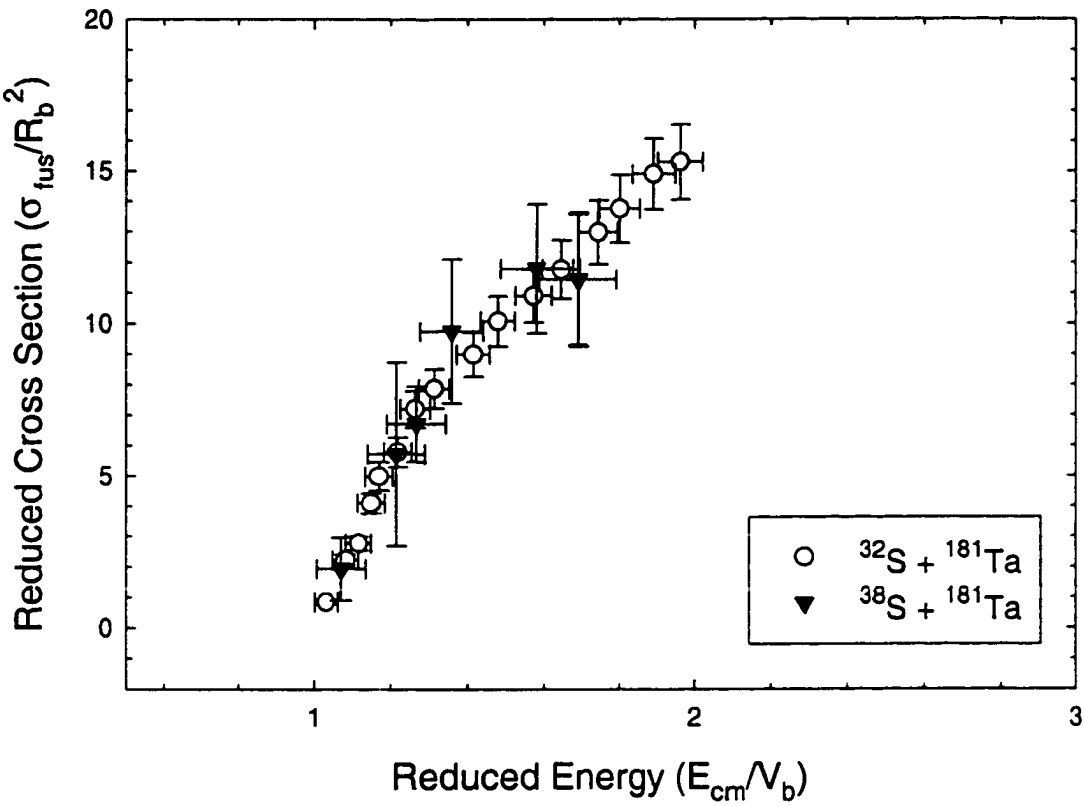

FIGURE 5.1. Reduced excitation functions for the $^{32,38}S + ^{181}Ta$ reactions.

be inferred from this data whether ^{38}S is not neutron-rich enough to possess a soft dipole mode, or if the effect simply is not present above the barrier.)

5.2. Evaporation residue formation

The increase in evaporation residue cross sections with increasing neutron-enrichment of a given projectile or target element is a well-known effect which has been observed for many systems (see reviews by Beckerman [Bec85, Bec88] and references therein; also [Rei85, Cle84, Gäg84]). In the context of heavy-element synthesis, the product compound nucleus is usually neutron-deficient (relative to β-stability) and highly fissionable. The increasing difference between the fission barrier and neutron binding energy with increasing neutron enrichment greatly increases the survival probability of the reaction products (see, e.g., a review by Schmidt and Morawek [Sch91], and references therein). For example, in the synthesis of ^{269,271}110 via the ^{62,64}Ni + ^{208}Pb reaction [Hof95a], the estimated experimental values for the production cross section increased by more than a factor of two in going from the ^{62}Ni to the ^{64}Ni projectile. It would be expected, then, that neutron-rich radioactive beams could prove to be an important tool in heavy-element synthesis reactions.

Estimates have been made of evaporation-residue production rates for the heaviest elements using neutron-rich radioactive projectiles [Lov93], based on predicted beam intensities for two proposed radioactive-beam facilities. Although much of the discussion in the literature of radioactive-beam fusion centers on enhancements to the cross section, the low beam intensities associated with radioactive beams are in many cases the limiting factor in a heavy-element production reaction. Figure 5.2 shows a comparison of evaporation-residue production rates using radioactive and stable beams. It can be seen that high-intensity stable beams are

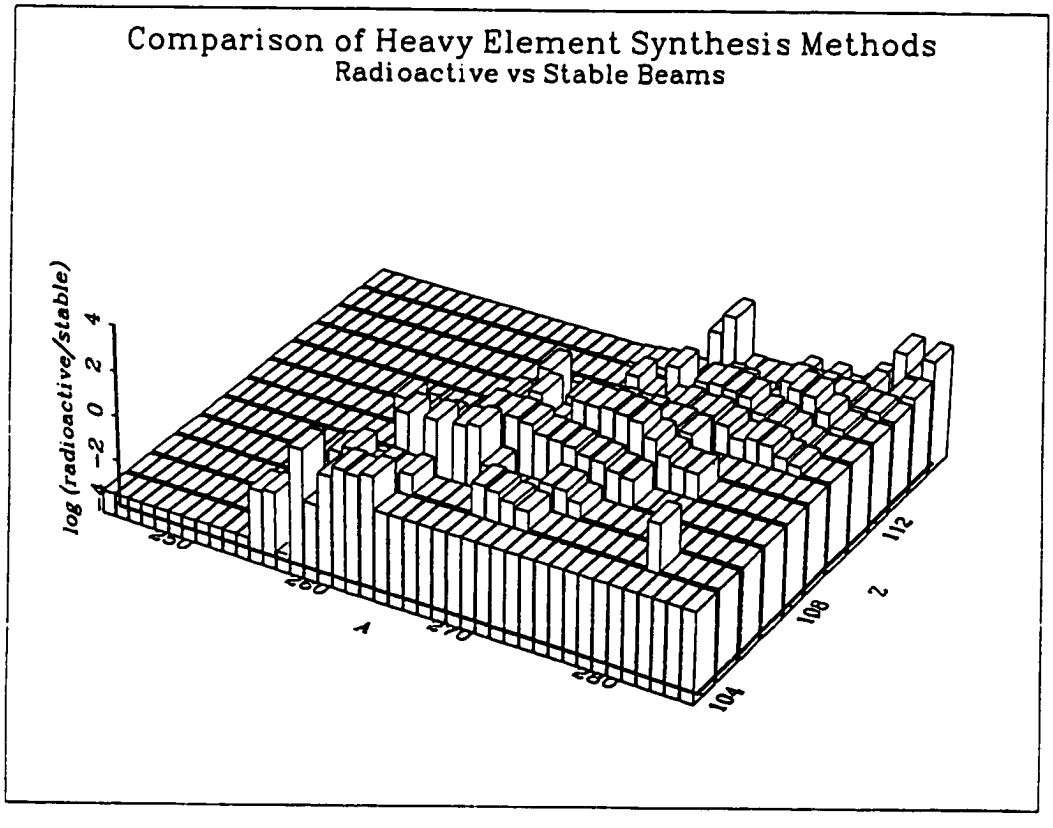

FIGURE 5.2. Comparison of heavy-element production rates using stable and radioactive beams [Lov93].

still the most efficient method of producing elements 110 and above, but that for the lighter elements, radioactive beams may be an effective method for synthesis of neutron-rich transactinides. This would open many opportunities for study of the physics and chemistry of the heaviest elements, even though currently available beam intensities are prohibitively low for radioactive-beam fusion to be a route to the extension of the periodic table.

It would be useful if the evaporation-residue production cross sections could be extrapolated from the measured fusion-fission data. However, systems similar to $^{32,38}S + ^{181}Ta$ for which both fission and residues have been measured show significant discrepancies between them. Clerc *et al.* [Cle84] have measured fission and neutron-evaporation residues for ^{40}Ar on targets from ^{165}Ho to ^{208}Pb, and saw that the maxima of the residue excitation functions in all cases were near the Bass barrier. In a measurement of $^{30}Si + ^{232}Th$, however, Ikezoe *et al.* [Ike98] calculated that an extra-extra-push energy of 8 MeV was necessary to describe the residue cross sections. Back and his colleagues [Bac99] have measured residues for the $^{32}S + ^{184}W$ system, and found that the cross sections, rather than peaking, continued increasing even well above the barrier. At the present time, there seems to be no straightforward way to extrapolate evaporation residue cross sections from the fission measurements of this analysis.

5.3. Summary

In summary, the fusion excitation function for the radioactive-beam reaction $^{38}S + ^{181}Ta$ was measured and compared to the stable-beam ^{32}S-induced reaction. It was found that the enhancement in the cross sections resulting from use of the radioactive projectile could be explained by a shift in the interaction barrier due to

the neutron enrichment of the projectile. The magnitude of the barrier shift was determined to be 5.9 ± 0.4 MeV; when the difference in reaction Q-values is also taken into account, the net lowering of the excitation energy at the barrier is about 12 MeV. This corresponds to retention of up to two additional neutrons in a heavy nucleus due to the use of a neutron-rich projectile. No indication of coupling to additional modes was observed for energies at and above the barrier.

It has been demonstrated in this work that fusion studies are possible with the current beam intensities at radioactive-beam facilities, if the experimental design is modified to accomodate very-low-rate events and typical RNB impurities; and that the barrier shift due to the use of the neutron-rich radioactive projectile is large enough to be of significance in heavy-element synthesis reactions.

5.4. Suggestions for future research

On the basis of this first-generation work, at least three areas can be identified where additional research could be quite useful in developing a stronger understanding of fusion reactions with radioactive neutron-rich projectiles. The first is a more quantitative analysis of quasifission, which would ideally include a spin-zero target, measurement of evaporation residues, more complete fission fragment angular distribution data, and measurement of coincident neutrons. Experimental measurements of the isotopic dependence of the quasifission component would also be useful in extrapolating to the radioactive-beam data. (Direct measurements of the RNB-induced angular distributions would be ideal, but would require significant beam times in order to obtain reasonable statistics.)

Secondly, as available beam intensities continue to increase with the improvements in radioactive-beam facilities, it should be possible to extend fusion measure-

ments to subbarrier energies. The effects of neutron transfer or flow and of the soft dipole vibration on subbarrier fusion with neutron-rich projectiles has been a topic of much theoretical discussion, and any data in this region will be of interest.

Lastly, extension to more neutron-rich species should be possible with the continuing improvements in RNB facilities. Although much of the focus of radioactive-beam fusion literature has been on extremely neutron-rich halo nuclei, other systems may also yield interesting results. For example, a systematic study of the sodium isotopes could be used in conjunction with charge- and matter-radius data to map the effects of the development of a neutron skin on fusion; and the deformed $N = 28$ shell in ^{44}S and ^{46}Ar would make them good projectiles in hot-fusion synthesis reactions.

All of the measurements mentioned above would benefit from supporting structure and reaction data; the area of fusion reactions with neutron-rich radioactive nuclear beams is a topic with many open questions and many opportunities for future research.

BIBLIOGRAPHY

[Agu88] C. E. Aguiar, V. C. Barbosa, L. F. Canto, and R. Donangelo, Phys. Lett. **B201** (1988) 22.

[Agu92] C. E. Aguiar, V. C. Barbosa, C. H. Dasso, and R. Donangelo, Phys. Rev. **C46** (1992) R45.

[Agu95] E. F. Aguilera, J. J. Kolata, and R. J. Tighe, Phys. Rev. **C52** (1995) 3103.

[Aky79] R. Ö. Akyüz and A. Winther, in *Nuclear Structure and Heavy Ion Reactions*, R. A. Broglia, C. H. Dasso, and R. Ricci, ed., North-Holland, Amsterdam (1981).

[Aud95] G. Audi and A. H. Wapstra, Nucl. Phys. **A595** (1995) 409.

[Bac81] B. B. Back, H.-G. Clerc, R. R. Betts, B. G. Glagola, and B. D. Wilkins, Phys. Rev. Lett. **46** (1981) 1068.

[Bac83] B. B. Back, R. R. Betts, K. Cassidy, B. G. Glagola, J. E. Gindler,L. E. Glendenin, and B. D. Wilkins, Phys. Rev. Lett. **50** (1983) 818.

[Bac85a] B. B. Back, Phys. Rev. **C31** (1985) 2104.

[Bac85b] B. B. Back, R. R. Betts, J. E. Gindler, B. D. Wilkins, S. Saini, M. B. Tsang, C. K. Gelbke, W. G. Lynch, M. A. McMahan, and P. A. Baisden, Phys. Rev. **C32** (1985) 195.

[Bac99] B. B. Back, to be published.

[Bal98] A. B. Balantekin and N. Takigawa, Rev. Mod. Phys. **70** (1998) 77.

[Bas74] R. Bass, Nucl. Phys. **A231** (1974) 45.

[Bas77] R. Bass, Phys. Rev. Lett. **39** (1977) 265.

[Bas80] R. Bass, *Nuclear Reactions with Heavy Ions*, Springer-Verlag, New York (1980) 283- 351.

[Bat97] O. Batenkov, K. Elmgren, M. Majorov, J. Blomgren, H. Condé, S. Hultqvist, N. Olsson, J. Rahm, E. Ramström, S. Smirnov, and A. Veshikov, Nucl. Instr. Meth. Phys. Res. **A394** (1997) 235.

[Bec80] M. Beckerman, M. Salomaa, A. Sperduto, H. Enge, J. Ball, A. DiRienzo, S. Gazes, Y. Chen, J. D. Molitoris, and M. Nai-Feng, Phys. Rev. Lett. **45** (1980) 1472.

[Bec81] M. Beckerman, J. Ball, H. Enge, M. Salomaa, A. Sperduto, S. Gazes, A. DiRienzo, and J. D. Molitoris, Phys. Rev. **C23** (1981) 1581.

[Bec82] M. Beckerman, M. Salomaa, A. Sperduto, J. D. Molitoris, and A. DiRienzo, Phys. Rev. **C25** (1982) 837.

[Bec83] M. Beckerman, M. K. Salomaa, J. Wiggins, and R. Rohe, Phys. Rev. **C28** (1983) 1963.

[Bec85] M. Beckerman, Phys. Rep. **129** (1985) 145.

[Bec88] M. Beckerman, Rep. Prog. Phys. **51** (1988) 1047.

[Bie96] J. D. Bierman, P. Chan, J. F. Liang, M. P. Kelly, A. A. Sonzogni, and R. Vandenbosch, Phys. Rev. **C54** (1996) 3068.

[Bir79] J. R. Birkelund, L. E. Tubbs, and J. R. Huizenga, Phys. Rep. **56** (1979) 107.

[Bjø82] S. Bjørnholm and W. J. Swiatecki, Nucl. Phys. **A391** (1982) 471.

[Blo77] J. Blocki, J. Randrup, W. J. Swiatecki, and C. F. Tsang, Ann. Phys. **105** (1977) 427.

[Boh39] N. Bohr and J. A. Wheeler, Phys. Rev. **56** (1939) 426.

[Boh56] A. Bohr, *Proceedings of the United Nations International Conference on the Peaceful Uses of Atomic Energy*, United Nations, N.Y. (1956) vol. 2 p. 151.

[Bor81] B. Borderie, M. Berlanger, D. Gardes, F. Hanappe, L. Nowicki, J. Peter, B. Tamain, S. Agarwal, J. Girard, C. Gregoire, J. Matuszek, and C. Ngô, Z. Phys. **A299** (1981) 263.

[Boy92] R. N. Boyd and I. Tanihata, Physics Today (1992) 44.

[Bro83a] R. A. Broglia, G. Pollarolo, and A. Winther, Nucl. Phys. **A406** (1983) 369.

[Bro83b] R. A. Broglia, C. H. Dasso, S. Landowne, and G. Pollarolo, Phys. Lett. **B133** (1983) 34.

[Cha94] A. Charlop, J. Bierman, Z. Drebi, A. Garcia, D. Prindle, A. A. Sonzogni, R. Vandenbosch, D. Ye, S. Gil, F. Hasenbalg, J. E. Testoni, D. Abriola, M. di Tada, A. Etchegoyen, M. C. Berisso, J. O. Fernandez-Niello, and A. J. Pacheco, Phys. Rev. **C49** (1994) R1235.

[Cha95] A. Charlop, J. Bierman, Z. Drebi, S. Gil, A. Sonzogni, R. Vandenbosch, and D. Ye, Phys. Rev. **C51** (1995) 623.

[Cle84] H.-G. Clerc, J. G. Keller, C.-C. Sahm, K.-H. Schmidt, H. Schulte, and D. Vermeulen, Nucl. Phys. **A419** (1984) 571.

[Coh74] S. Cohen, F. Plasil, and W. J. Swiatecki, Ann. Phys. **82** (1974) 557.

[Das83] C. H. Dasso, S. Landowne, and A. Winther, Nucl. Phys. **A407** (1983) 221.

[Das87] C. H. Dasso and S. Landowne, Comp. Phys. Comm. **46** (1987) 187.

[Das92] C. H. Dasso and R. Donangelo, Phys. Lett. **B276** (1992) 1.

[Das97] M. Dasgupta, K. Hagino, C. R. Morton, D. J. Hinde, J. R. Leigh, N. Takigawa, H. Timmers, and J. O. Newton, J. Phys. **G23** (1997) 1491.

[Das98] M. Dasgupta, D. J. Hinde, N. Rowley, and A. M. Stefanini, ANU-P/1365 (1998); to be published in Ann. Rev. Nucl. Part. Sci. (1998).

[Del79] H. Delagrange, D. Logan, M. F. Rivet, M. Rajagopalan, J. M. Alexander, M. S. Zisman, M. Kaplan, and J. W. Ball, Phys. Rev. Lett. **43** (1979) 1490.

[Dey98] P. A. DeYoung, B. Hughey, P. L. Jolivette, G. F. Peaslee, J. J. Kolata, V. Guimaraes, D. Peterson, P. Santi, H. C. Griffin, J. A. Zimmerman, and J. D. Hinnefeld, Phys. Rev. **C58** (1998) 3442.

[Due85] E. Duek, L. Kowalski, and J. M. Alexander, Comp. Phys. Comm. **34** (1985) 395.

[Esb96] H. Esbensen and B. B. Back, Phys. Rev. **C54** (1996) 3109.

[Fek95] V. Fekou-Youmbi, J. L. Sida, N. Alamanos, F. Auger, D. Bazin, C. Borcea, C. Cabot, A. Consulo, A. Foti, A. Gillibert, A. Lepine, M. Lewitowicz, R. Liguori-Neto, W. Mittig, E. Pollacco, P. Roussel-Chomaz, C. Volant, and Y. Y. Feng, Nucl. Phys. **A583** (1995) 811c.

[Fek97] V. Fekou-Youmbi, J. L. Sida, N. Alamanos, W. Mittig, F. Auger, D. Bazin, C. Borcea, C. Cabot, X. Charlot, A. Cunsolo, A. Foti, A. Gillibert, N. Lecesne, A. Lepine, M. Lewitowicz, R. Liguori-Neto, F. Marie, C. Mazur, A. Mougeot, S. Ottini, E. Pollacco, A. Ostrowski, M. Riallot, P. Roussel-Chomaz, C. Volant, and Y. Y. Feng, J. Phys. **G23** (1997) 1259.

[Fel84] H. Feldmeier, in *Proceedings of the International School of Physics "Enrico Fermi"*, L. Moretto and R. A. Ricci, eds., North-Holland, Amsterdam (1984) 274.

[Fer89] J. Fernández-Niello, C. H. Dasso, and S. Landowne, Comp. Phys. Comm. **54** (1989) 409.

[Fox89] R. Fox, R. Au, and A. VanderMolen, IEEE Trans. Nucl. Sci **36** (1989) 1562.

[Fri85] E. M. Friedlander and H. H. Heckman, in Treatise On Heavy-Ion Science, vol. 4, D. A. Bromley, ed., Plenum Press, N.Y. (1985) 403.

[Gav80] A. Gavron, Phys. Rev. **C21** (1980) 230.

[Gie95] H. Giessel, G. Münzenberg, and K. Riisager, Ann. Rev. Nucl. Part. Sci. **45** (1995) 163.

[Gäg84] H. Gäggeler, T. Sikkeland, G. Wirth, W. Bruchle, W. Bogl, G. Franz, G. Herrmann, J.V. Kratz, M. Schadel, K. Summerer, and W. Weber, Z. Phys. **A316** (1984) 291.

[Hil53] D. L. Hill and J. A. Wheeler, Phys. Rev. **89** (1953) 1102.

[Hin89] D. J. Hinde, H. Ogata, M. Tanaka, T. Shimoda, N. Takahashi, A. Shinohara, S. Wakamatsu, K. Katori, and H. Okamura, Phys. Rev. **C39** (1989) 2268.

[Hin92] D. J. Hinde, D. Hilscher, H. Rossner, B. Gebauer, M. Lehmann, and M. Wilpert, Phys. Rev. **C45** (1992) 1229.

[Hin95] D. J. Hinde, C. R. Morton, M. Dasgupta, J. R. Leigh, J. C. Mein, and H. Timmers, Nucl. Phys. **A592** (1995) 271.

[Hin96] D. J. Hinde, M. Dasgupta, J. R. Leigh, J. C. Mein, C. R. Morton, J. O. Newton, and H. Timmers, Phys. Rev. **C53** (1996) 1290.

[Hof95a] S. Hofmann, V. Ninov, F. P. Hessberger, P. Armbruster, H. Folger, G. Münzenberg, H. J. Schott, A. G. Popeko, A. V. Yeremin, A. N. Andreyev, S. Saro, R. Janik, and M. Leino, Z. Phys. **A350** (1995) 277; GSI Nachrichten 02- 1995 (1995) 4.

[Hof95b] S. Hofmann, V. Ninov, F. P. Hessberger, P. Armbruster, H. Folger, G. Münzenberg, H. J. Schott, A. G. Popeko, A. V. Yeremin, A. N. Andreyev, S. Saro, R. Janik, and M. Leino, Z. Phys. **A350** (1995) 281.

[Hub90] F. Hubert, R. Bimbot, and H. Gauvin, At. Data Nucl. Data Tables **46** (1990) 1; Nucl. Instr. Meth. Phys. Res. **B36** (1989) 357.

[Hui69] J. R. Huizenga, A. N. Behkami, and L. G. Moretto, Phys. Rev. **177** (1969) 1826.

[Hui83] J. R. Huizenga, J. R. Birkelund, L. E. Tubbs, D. Hilscher, U. Jahnke, H. Rossner, B. Gebauer, and H. Lettau, Phys. Rev. **C28** (1983) 1853.

[Hus91a] M. S. Hussein, Nucl. Phys. **A531** (1991) 192.

[Hus91b] M. S. Hussein, Phys. Rev. **C44** (1991) 446.

[Ike98] H. Ikezoe, T. Ikuta, S. Mitsuoka, T. Kuzumaki, J. Lu, Y. Nagame, I. Nishinaka, K. Tsukada, and T. Ohtsuki, ENAM 98: Exotic Nuclei and Atomic Masses, B. M. Sherrill, D. J. Morrissey, and C. N. Davids, eds., AIP (1998) 548.

[Kar68] S. A. Karamyan, I. V. Kuznetsov, T. A. Muzycka, Yu. Ts. Oganesyan, Yu. E. Penionzkevich, and B. I. Pustylnik, Sov. J. Nucl. Phys. **6** (1968) 360.

[Kel87] J. G. Keller, B. B. Back, B. G. Glagola, D. Henderson, S. B. Kaufman, S. J. Sanders, R. H. Siemssen, F. Videbaek, B. D. Wilkins, and A. Worsham, Phys. Rev. **C36** (1987) 1364.

[Kol98] J. J. Kolata, V. Guimaraes, D. Peterson, P. Santi, R. White-Stevens, J. von Schwarzenberg, J. D. Hinnefeld, E. F. Aguilera, E. Martinez-Quiroz, D. A. Roberts, F. D. Becchetti, M. Y. Lee, and R. A. Kryger, Phys. Rev. **C57** (1998) R6; Phys. Rev. Lett. **81** (1998) 4580.

[Kra79] H. J. Krappe, J. R. Nix, and A. J. Sierk, Phys. Rev. Lett. **42** (1979) 215; Phys. Rev. **C20** (1979) 992.

[Kru93] A. T. Kruppa, P. Romain, M. A. Nagarajan, and N. Rowley, Nucl. Phys. **A560** (1993) 845.

[Lan84] S. Landowne and C. H. Dasso, Phys. Lett. **B138** (1984) 32.

[Lil95] J. O. Liljenzin, private communication.

[Liu94] Z. Liu, H. Zhang, J. Xu, X. Quin, Y. Qiao, C. Lin, and K. Xu, Phys. Rev. **C50** (1994) 1717.

[Liu96] Z. Liu, H. Zhang, J. Xu, Y. Qiao, X. Qian, and C. Lin, Phys. Rev. **C54** (1996) 761.

[Lov93] W. D. Loveland, in *Proceedings of the 3rd International Conference on Radioactive Nuclear Beams*, D. J. Morrissey ed. Gif-sur-Yvette: Editions Frontières (1993) 526.

[Mac96] A. M. M. Maciel and P. R. S. Gomes, Phys. Rev. **C53** (1996) 1981.

[Maj96] N. Majumdar, P. Bhattacharya, D. C. Biswas, R. K. Choudhury, D. M. Nadkarni, and A. Saxena, Phys. Rev. **C53** (1996) R544.

[Mor95] C. R. Morton, D. J. Hinde, J. R. Leigh, J. P. Lestone, M. Dasgupta, J. C. Mein, J. O. Newton, and H. Timmers, Phys. Rev. **C52** (1995) 243.

[Mor98] C. R. Morton, private communication.

[Mue93] A. C. Mueller and B. M. Sherrill, Ann. Rev. Nucl. Part. Sci. **43** (1993) 529.

[Möl95] P. Möller, J. R. Nix, W. D. Myers, and W. J. Swiatecki, At. Data Nucl. Data Tables **59** (1995) 185.

[Mün81] G. Münzenberg, S. Hofmann, F. P. Hessberger, W. Reisdorf, K.-H. Schmidt, J.H.R.Schneider, P. Armbruster, C. C. Sahm, and B. Thuma, Z. Phys. **A300** (1981) 107.

[Mün82] G. Münzenberg, P. Armbruster, F. P. Hessberger, S. Hofmann, K. Poppensieker, W. Reisdorf, J. H. R. Schneider, W. F. W. Schneider, K.-H. Schmidt, C.-C. Sahm, and D. Vermeulen, Z. Phys. **A309** (1982) 89.

[Mün84] G. Münzenberg, P. Armbruster, H. Folger, F. P. Hessberger, S. Hofmann, J. Keller, K. Poppensieker, W. Reisdorf, K.-H. Schmidt, H.-J. Schott, M. E. Leino, and R. Hingmann, Z. Phys. **A317** (1984) 235

[Mün86] G. Münzenberg, P. Armbruster, G. Berthes, H. Folger, F. P. Hessberger, S. Hofmann, K. Poppensieker, W. Reisdorf, B. Quint, K.-H. Schmidt, H.-J. Schott, K. Summerer, I. Zychor, M. E. Leino, U. Gollerthan, and E. Hanelt, Z. Phys. **A324** (1986) 489.

[Mün88] G. Münzenberg, S. Hofmann, F. P. Hessberger, H. Folger, V. Ninov, K. Poppensieker, A. B. Quint, W. Reisdorf, H.-J. Schott, K. Summerer, P. Armbruster, M. E. Leino, D. Ackermann, U. Gollerthan, E. Hanelt, W. Morawek, Y. Fujita, T. Schwab, and A. Turler, Z. Phys. **A330** (1988) 435.

[Ngô75] C. Ngô, B. Tamain, M. Beiner, R. J. Lombard, D. Mas, and H. H. Deubler, Nucl. Phys. **A252** (1975) 237.

[Oer96] W. von Oertzen and I. Krouglov, Phys. Rev. **C53** (1996) R1061.

[Oga74] Yu. Ts. Oganessian, Yu. p. Tretyakov, A. S. Ilinov, A. G. Demin, A. A. Pleve, S. P. Tretyakova, V. M. Plotko, M. P. Ivanov, N. A. Danilov, Yu. S. Korotkin, and G. N. Flerov, Soviet Phys. JETP Lett. **20** (1974) 265.

[Oga84] Yu. Ts. Oganessian, A. G. Demin, M. Hussonnois, S. P. Tretyakova, Yu. P. Kharitonov, V. K. Utyonkov, I. V. Shirokovsky, O. Constantinescu, H. Bruchertseifer, and Yu. S. Korotkin, Z. Phys. **A319** (1984) 215.

[Pen95] Y. Penionzhkevich, Nucl. Phys. **A588** (1995) 259c.

[Ram87] S. Raman, C. H. Malarkey, W. T. Milner, C. W. Nestor, Jr., and P. H. Stelson. At. Data Nucl. Data Tables **36** (1987) 1.

[Ram87b] V. S. Ramamurthy, in *SERC School Series, Nuclear Physics, Rajasthan University, Jaipur, India*, ed. B. K. Jain, World Scientific, New Jersey (1987) 269; and references therein.

[Ram90] V. S. Ramamurthy, S. S. Kapoor, R. K. Choudhury, A. Saxena, D. M. Nadkarni, A. K. Mohanty, B. K. Nayak, S. V. Sastry, S. Kailas, A. Chatterjee, P. Singh, and A. Navin, Phys. Rev. Lett. **65** (1990) 25.

[Ran74] J. Randrup, W. J. Swiatecki, and C. F. Tsang, Lawrence Berkeley Laboratory Report No. 3603 (1974).

[Rei81] W. Reisdorf, Z. Phys. **A300** (1981) 227.

[Rei82] W. Reisdorf, F. P. Hessberger, K. D. Hildenbrand, S. Hofmann, G. Münzenberg, K.-H. Schmidt, J. H. R. Schneider, W. F. W. Schneider, K. Summerer, G. Wirth, J. V. Kratz, and K. Schlitt, Phys. Rev. Lett. **49** (1982) 1811.

[Rei85] W. Reisdorf, F. P. Hessberger, K. D. Hildenbrand, S. Hofmann, G. Münzenberg, K.-H. Schmidt, J. H. R. Schneider, W. F. W. Schneider, K. Summerer, G. Wirth, J. V. Kratz, and K. Schlitt, Nucl. Phys. **A438** (1985) 212; Nucl. Phys. **A444** (1985) 154.

[Rei94] W. Reisdorf, J. Phys. **G20** (1994) 1297.

[Ros83] H. Rossner, D. Hilscher, E. Holub, G. Ingold, U. Jahnke, H. Orf, J. R. Huizenga, J. R. Birkelund, W. U. Schroder, and W. W. Wilcke, Phys. Rev. **C27** (1983) 2666.

[Ros97] E. S. Rossi, Jr., L. C. Chamon, D. Pereira, C. P. Silva, and G. Ramirez, J. Phys. **G23** (1997) 1473.

[Row91] N. Rowley, G. R. Satchler, and P. H. Stelson, Phys. Lett. **B254** (1991) 25.

[Roy98] G. Royer, C. Normand, and E. Druet, Nucl. Phys. **A634** (1998) 267.

[Rud97] G. Rudolf, Institut de Recherches Subatomique, preprint IreS 97-28 (1997).

[Sam96] M. Samant and S. Kailas, Z. Phys. **A356** (1996) 309.

[Sat90] G. R. Satchler, *Introduction to Nuclear Reactions*, Oxford University Press, N.Y., 1990.

[Sch66] H. W. Schmitt, J. H. Neiler, and F. J. Walter, Phys. Rev. **141** (1966) 1146; H. W. Schmitt and F. Pleasonton, Nucl. Instr. Meth. **40** (1966) 204.

[Sch91] K.-H. Schmidt and W. Morawek, Rep. Prog. Phys. **54** (1991) 949.

[Sch96] H. Scheit, T. Glasmacher, B. A. Brown, J. A. Brown, P. D. Cottle, P. G. Hansen, R. Harkewicz, M. Hellstrom, R. W. Ibbotson, J. K. Jewell, K. W. Kemper, D. J. Morrissey, M. Steiner, P. Thirolf, and M. Thoennessen, Phys. Rev. Lett. **77** (1996) 3967.

[She87] W. Q. Shen, J. Albinski, A. Gobbi, S. Gralla, K. D. Hildenbrand, N. Herrmann, J. Kuzminski, W. F. J. Muller, H. Stelzer, J. Toke, B. B. Back, S. Bjørnholm, and S. P. Sorensen, Phys. Rev. **C36** (1987) 115.

[She91] B. M. Sherrill, D. J. Morrissey, J. A. Nolan, and J. A. Winger, Nucl. Instr. Meth. **B56/57** (1991) 1106.

[She94] B. Sherrill and J. Winfield, MSUCL Report no. 499 (1994).

[Siw79] K. Siwek-Wilczyńska, E. H. du Marchie van Voorthuysen, J. van Popta, R. H. Siemssen, and J. Wilczyński, Phys. Rev. Lett. **42** (1979) 1599.

[Spe89] R. H. Spear, At. Data Nucl. Data Tables **42** (1989) 55.

[Ste86] A. M. Stefanini, G. Fortuna, R. Pengo, W. Meczynski, G. Montagnoli, L. Corradi, A. Tivelli, S. Beghini, C. Signorini, S. Lunardi, M. Morando, and F. Soramel, Nucl. Phys. **A456** (1986) 509.

[Ste92] A. M. Stefanini, Nucl. Phys. **A538** (1992) 195c.

[Ste95] A. M. Stefanini, D. Ackermann, L. Corradi, J. H. He, G. Montagnoli, S. Beghini, F. Scarlassara, and G. F. Segato, Phys. Rev. **C52** (1995) R1727.

[Ste90] P. H. Stelson, H. J. Kim, M. Beckerman, D. Shapira, and R. L. Robinson, Phys. Rev. **C41** (1990) 1584.

[Sto78] R. G. Stokstad, Y. Eisen, S. Kaplanis, D. Pelte, U. Smilansky, and I. Tserruya, Phys. Rev. Lett. **41** (1978) 465.

[Sto80] R. G. Stokstad, Y. Eisen, S. Kaplanis, D. Pelte, U. Smilansky, and I. Tserruya, Phys. Rev. **C21** (1980) 2427.

[Swa94] D. Swan, J. Yurkon, and D. J. Morrissey, Nucl. Instr. Meth. Phys. Res. **A348** (1994) 314.

[Swi81] W. J. Swiatecki, Phys. Scr. **24** (1981) 113.

[Swi82] W. J. Swiatecki, Nucl. Phys. **A376** (1982) 275.

[Süm90] K. Sümmerer, W. Bruchle, D. J. Morrissey, M. Schadel, B. Szweryn, and W. Yang, Phys. Rev. **C42** (1990) 2546.

[Tak91] N. Takigawa and H. Sagawa, Phys. Lett. **B265** (1991) 23.

[Tak92] N. Takigawa, H. Sagawa, and T. Shinozuka, Nucl. Phys. **A538** (1992) 221c.

[Tsa83] M. B. Tsang, D. Ardouin, C. K. Gelbke, W. G. Lynch, Z. R. Xu, B. B. Back, R. Betts, S. Saini, P. A. Baisden, and M. A. McMahan, Phys. Rev. **C28** (1983) 747.

[Tub85] L. E. Tubbs, J. R. Birkelund, J. R. Huizenga, D. Hilscher, U. Jahnke, H. Rossner, and B. Gebauer, Phys. Rev. **C32** (1985) 214.

[Van73] R. Vandenbosch and J. R. Huizenga, *Nuclear Fission*, Academic Press, N.Y. (1973).

[Van96] R. Vandenbosch, J. D. Bierman, J. P. Lestone, J. F. Liang, D. J. Prindle, A. A. Sonzogni, S. Kailas, D. M. Nadkarni, and S. S. Kapoor, Phys. Rev. **C54** (1996) R977.

[Vaz78] L. C. Vaz and J. M. Alexander, Phys. Rev. **C18** (1978) 2152.

[Vaz81] L. C. Vaz, J. M. Alexander, and G. R. Satchler, Phys. Rep. **69** (1981) 373.

[Vio63] V. E. Viola, Jr., T. D. Thomas, and G. T. Seaborg, Phys. Rev. **129** (1963) 2710.

[Vio85] V. E. Viola, K. Kwiatkowski, and M. Walker, Phys. Rev. **C31** (1985) 1550.

[Wei86] E. Weissenberger, P. Geltenbort, A. Oed, F. Gonnenwein, and H. Faust, Nucl. Instrum. Meth. Phys. Res. **A248** (1986) 506.

[Wil80] W. W. Wilcke, J. R. Birkelund, H. J. Wollersheim, A. D. Hoover, J. R. Huizenga, W. U. Schroder, and L. E. Tubbs, At. Data Nucl. Data Tables **25** (1980) 389.

[Wil80b] J. Wilczyński, K. Siwek-Wilczyńska, J. van Driel, S. Gonggrijp, D. C. J. M. Hageman, R. V. F. Janssens, J. Lukasiak, and R. H. Siemssen, Phys. Rev. Lett. **45** (1980) 606.

[Wil82] J. Wilczyński, K. Siwek-Wilczyńska, J. Van Driel, S. Gonggrijp, D. C. J. M. Hageman, R. V. F. Janssens, J. Lukasiak, R. H. Siemssen, and S. Y. Van Der Werf, Nucl. Phys. **A373** (1982) 109.

[Win92] J. A. Winger, B. M. Sherrill, and D. J. Morrissey, Nucl. Instr. Meth. Phys. Res. **B70** (1992) 380.

[Won73] C. Y. Wong, Phys. Rev. Lett. **31** (1973) 766.

[Woo54] R. W. Woods and D. S. Saxon, Phys. Rev. **95** (1954) 577.

[Wu86] J. Q. Wu and G. F. Bertsch, Nucl. Phys. **A457** (1986) 401.

[Yos95] A. Yoshida, N. Aoi, T. Fukuda, M. Hirai, M. Ishihara, H. Kobinata, Y. Mizoi, L. Mueller, Y. Nagashima, J. Nakano, T. Nomura, Y. H. Pu, F. Scarlassara, C. Signorini, Y. Watanabe Nucl. Phys. **A588** (1995) 109c.

[Yur99] J. Yurkon, private communication.

[Zyr97] K. E. Zyromski, W. Loveland, G. A. Souliotis, D. J. Morrissey, C. F. Powell, O. Batenkov, K. Aleklett, R. Yanez, I. Forsberg, M. Sanchez-Vega, J. R. Dunn, and B. G. Glagola, Phys. Rev. **C55** (1997) R562.